



Fermi National Accelerator Laboratory

FERMILAB-Pub-96/357-E

DØ

The DØ Upgrade The Detector and Its Physics

**S. Abachi et al.
The DØ Collaboration**

*Fermi National Accelerator Laboratory
P.O. Box 500, Batavia, Illinois 60510*

October 1996

Disclaimer

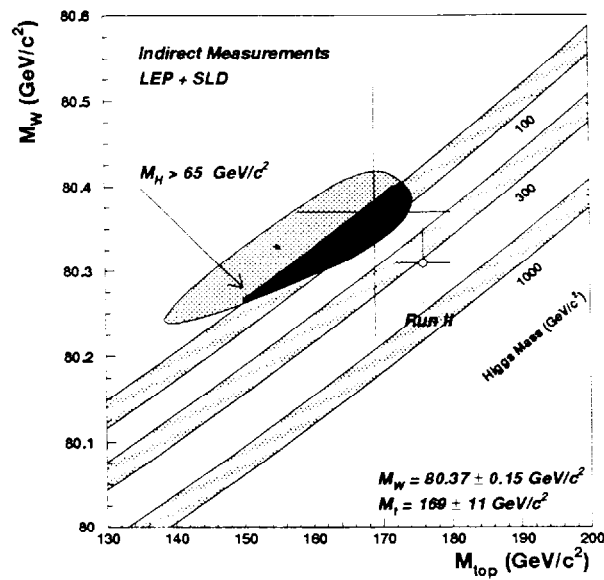
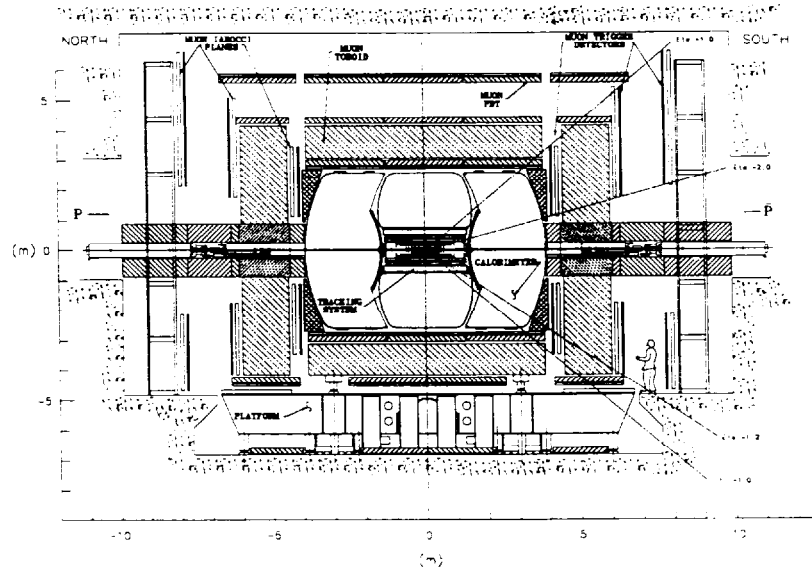
This report was prepared as an account of work sponsored by an agency of the United States Government. Neither the United States Government nor any agency thereof, nor any of their employees, makes any warranty, express or implied, or assumes any legal liability or responsibility for the accuracy, completeness or usefulness of any information, apparatus, product or process disclosed, or represents that its use would not infringe privately owned rights. Reference herein to any specific commercial product, process or service by trade name, trademark, manufacturer or otherwise, does not necessarily constitute or imply its endorsement, recommendation or favoring by the United States Government or any agency thereof. The views and opinions of authors expressed herein do not necessarily state or reflect those of the United States Government or any agency thereof.

Distribution

Approved for public release: further dissemination unlimited.

The DØ Upgrade

The Detector and Its Physics



The DØ Collaboration
July 30, 1996

Contents

1	Overview of the Upgrade	5
2	Description of the DØ Upgrade	8
2.1	The Solenoid Magnet	8
2.2	The Silicon Vertex Detector	9
2.2.1	Silicon Detectors	10
2.2.2	Mechanical Support	10
2.2.3	Assembly and Testing	13
2.3	The Scintillating Fiber Tracker	14
2.3.1	Scintillating Fibers	14
2.3.2	Photodetectors	15
2.3.3	Cosmic Ray Test Setup	15
2.3.4	R&D and Design	16
2.4	Tracking Electronics	17
2.4.1	SVX II Chip	17
2.4.2	Silicon Readout	17
2.4.3	Fiber Tracker Readout	17
2.5	The Preshower Detectors	20
2.5.1	Central Preshower	20
2.5.2	Forward Preshower	21
2.6	The Calorimeter System	24
2.6.1	Calorimeter Front-End Electronics	24
2.6.2	The Intercryostat Detector	25
2.7	The Muon System	26
2.7.1	Introduction	26
2.7.2	Shielding	26

2.7.3	Central Muon Detectors	27
2.7.4	Forward Muon Detectors	30
2.7.5	Front-End Electronics	34
2.8	Trigger Systems	36
2.8.1	Introduction	36
2.8.2	The Trigger Framework	36
2.8.3	Level 1	37
2.8.4	Level 2	39
2.8.5	Level 3	41
2.8.6	Trigger Examples and Rates	42
2.8.7	Summary	43
2.9	Luminosity Monitor	44
2.10	Data Acquisition and Computing	45
2.11	Software Upgrades	47
2.11.1	Software Organization	47
2.11.2	Online	47
2.11.3	Algorithms	47
2.11.4	Offline	48
2.11.5	Production and Data Access	48
2.11.6	Summary	48
3	Physics Topics and Detector Performance	49
3.1	Introduction	49
3.2	Top Physics	51
3.2.1	Run I Observation of the Top Quark	51
3.2.2	Run II Detector Improvements for Top Physics	52
3.2.3	$t\bar{t}$ Production Cross Section	54
3.2.4	Top Quark Mass	54

3.2.5	Top Quark Decay Properties	55
3.2.6	W Polarization from Top Decays	55
3.2.7	Single Top Production	57
3.2.8	Search for the Charged Higgs Boson in Top Decays	57
3.2.9	Discovery of New Physics in the $t\bar{t}$ Channel	59
3.3	Electroweak Physics	60
3.3.1	W Boson Mass	60
3.3.2	W Boson Decay Properties	62
3.3.3	The W Boson Charge Asymmetry	63
3.3.4	Forward–Backward Charge Asymmetry in Z Decays	65
3.3.5	Anomalous Vector Boson Couplings	66
3.4	QCD	68
3.4.1	Introduction	68
3.4.2	Parton Distributions	68
3.4.3	Next–to–Leading Order and Beyond	69
3.4.4	Drell–Yan (W/Z) Production	70
3.4.5	Jet Algorithms and Studies of Jet Structure	70
3.4.6	Rapidity Gaps, Diffractive Scattering and the Pomeron	71
3.5	B –Physics	72
3.5.1	Introduction	72
3.5.2	B_s Mixing	74
3.5.3	CP Violation	75
3.5.4	Other B –Physics Topics	77
3.6	Searches for New Phenomena	78
3.6.1	An Overview of New Particle Searches	78
3.6.2	The Z' Search	78
3.6.3	The Gaugino Search	79

3.6.4	The \tilde{t} Search	80
3.6.5	The $\tilde{q} - \tilde{g}$ Search	80
3.6.6	Other Searches	81
3.7	Beyond Run II	82
4	Conclusions	83

1 Overview of the Upgrade

The DØ upgrade will be a key element of the U.S. high energy physics program in the next decade. The upgrade will enable us to pursue forefront physics in the new high luminosity Main Injector environment. The original DØ upgrade proposal [1] was presented to the Laboratory in Fall 1990. Almost all components of the upgraded detector now approved were presented there. The detailed understanding of each has been refined through subsequent submissions to the Laboratory and PAC in the intervening years, and through reviews conducted by the PAC (April 1991), Director (Feb. 1992, May 1994, Jan. 1995) and DOE (May 1996). The status of approval by the Fermilab director is summarized in [2].

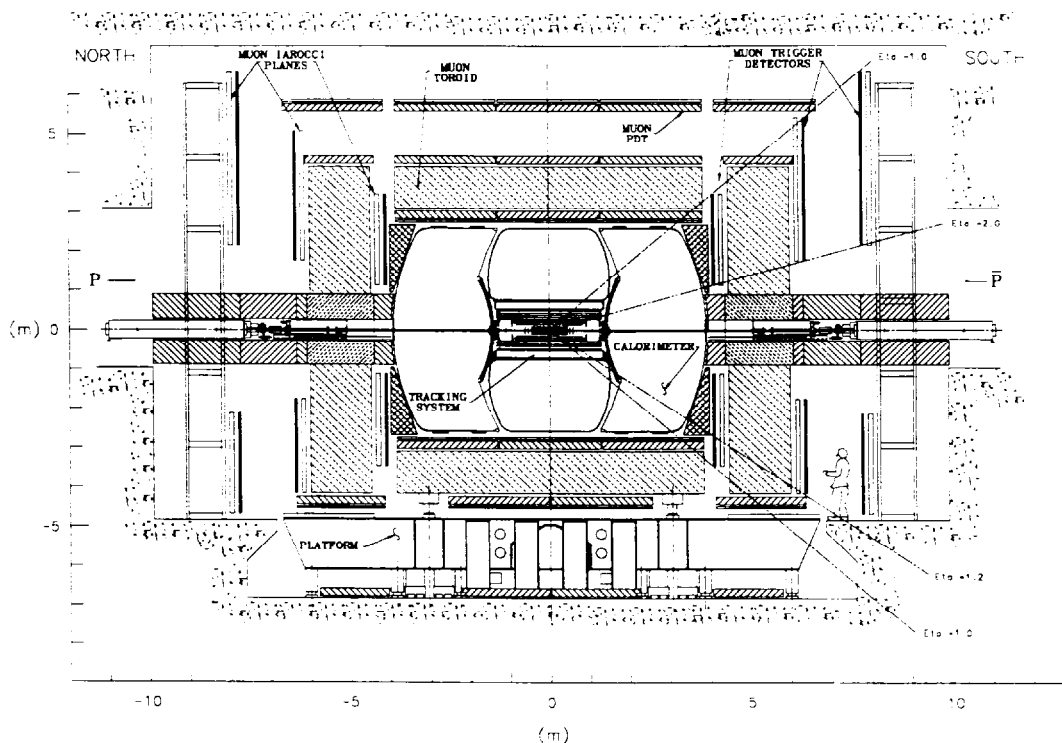


Figure 1: Side view of the DØ upgrade detector with major upgrade detector systems indicated.

The upgrade has been designed to operate reliably and with small deadtimes for instantaneous luminosity in the upgraded Tevatron of $2 \times 10^{32} \text{ cm}^{-2}\text{s}^{-1}$ and bunch crossing times of $\Delta t \geq 132 \text{ ns}$. The design is based upon a beam structure with at least $2 \mu\text{s}$ gaps between superbunches. There was not a requirement that the upgraded detector operate at the higher instantaneous luminosities which might be encountered in post Run II operation, but wherever possible, and without incurring added cost or complexity, choices were made to enable or simplify such operation. The upgrade builds on the strengths of DØ, full coverage in calorimetry and muon detection, while enhancing the tracking and triggering capabilities. Construction is

now underway on a number of the detector systems. It is thus an appropriate juncture at which to review the DØ upgrade detector systems and the physics performance we will achieve with the upgrade. Technical design reports are kept for individual detector subsystems separately.

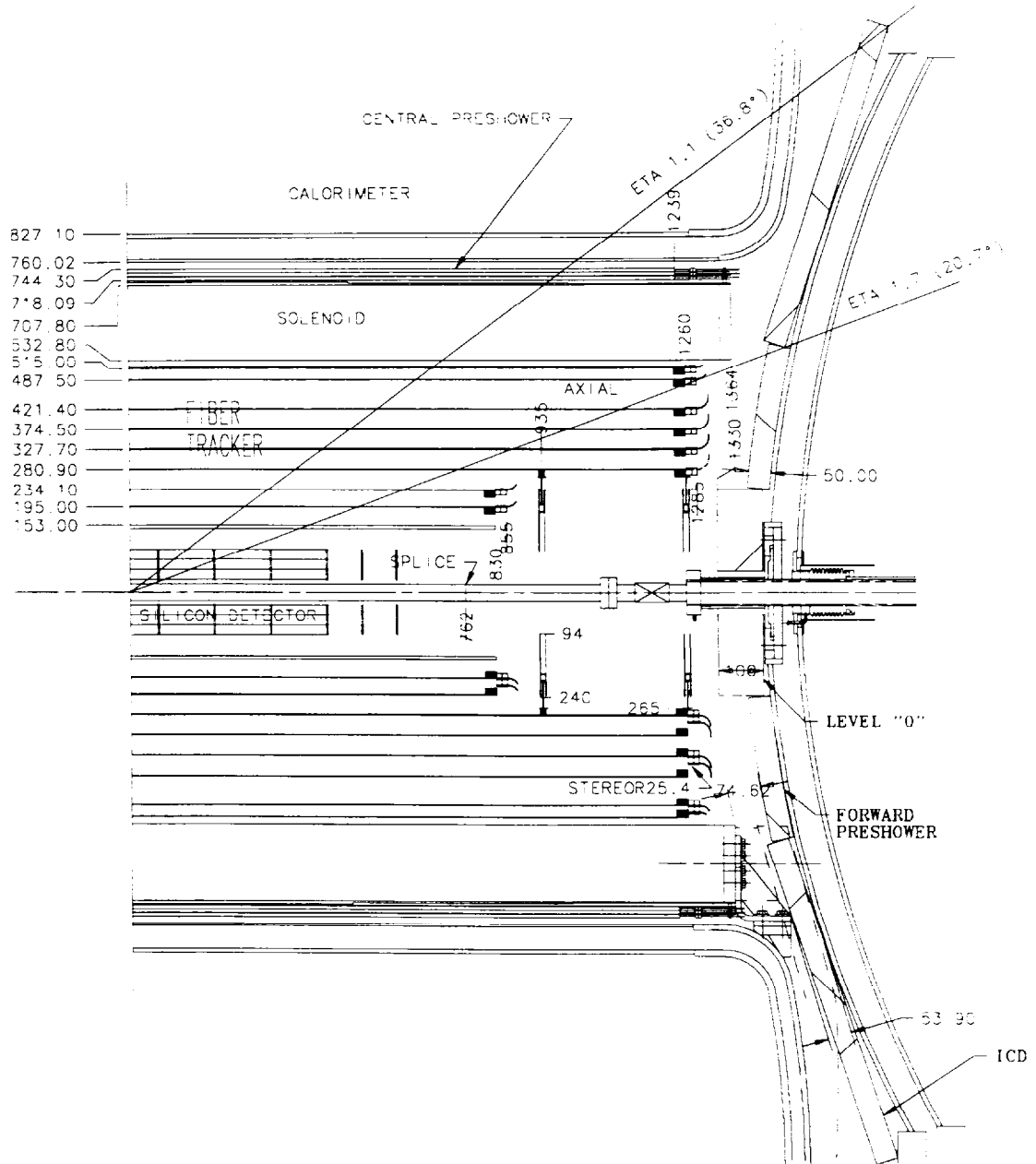


Figure 2: One-half side view of the DØ tracking upgrade (dimensions in mm).

In Section 2 we summarize the design of the major upgrade detector systems sufficient to give a broad overview, without excess detail. An overall view of the DØ detector is shown in Fig. 1 with the primary detector systems indicated. A major element of the upgrade is the replacement of the inner tracking systems, required because of the new Tevatron time structure, the expected radiation damage to those detectors by Run II, and also to improve the physics capabilities of the DØ detector. The upgraded tracking system consists of an inner silicon vertex detector, surrounded by eight superlayers of scintillating fiber tracker. These detectors

are located inside a 2 Tesla superconducting solenoid. A scintillator based central preshower detector with wavelength shifter readout is located between the outer radius of the solenoid and the inner radius of the central calorimeter cryostat to provide electron identification and to compensate for energy losses in the solenoid. A detailed view of the DØ upgrade tracking system is shown in Fig. 2. In the forward region, a preshower detector similar to the central preshower detector is installed on the faces of the end calorimeter cryostats. We had considered small angle tracking detectors, but eliminated them in favor of extended fiber barrels and small angle silicon disks due to cost considerations. The higher event rates in Run II have led us to add new muon trigger detectors covering the full pseudorapidity range and the harsh radiation environment of Run II has prompted us to replace the forward proportional drift tubes with mini-drift tubes. Electronic upgrades are driven by the need to handle a smaller bunch spacing and provide pipelining of the various front end signals from the tracking, calorimeter, and muon systems. The front-end electronics for all these systems will be replaced. A new level of triggering is planned to help reduce the raw event rates to manageable proportions. The addition of new trigger elements and front-end electronics requires a new trigger control system.

In Section 3, we summarize the physics capabilities of the DØ upgrade detector. The strengths of DØ are considerably enhanced in many areas of high p_T physics such as the ability to tag b -quarks in top decays using the silicon detector. Precision electroweak measurements such as the W mass measurement will benefit from the *in situ* energy calibration provided by electron momentum measurements. Several electroweak measurements that were previously impossible, such as the forward-backward charge asymmetry of Z decays will be accessible with the addition of the magnetic field. The upgrades to the muon system and the inner tracking system will improve our B physics capabilities by allowing triggering on low p_T muons and low mass dimuons and the reconstruction of complete B final states. Finally, we note that the significant improvements in the lepton and photon identifications and the maintenance of the good E_T resolution will greatly expand our capability for searching for new physics beyond the Standard Model.

2 Description of the DØ Upgrade

2.1 The Solenoid Magnet

The momenta of charged particles will be determined from their curvature in the 2T magnetic field provided by a 2.8m long solenoid magnet [3]. The superconducting (SC) solenoid, a two layer coil with mean radius of 60cm, has a stored energy of 5MJ (for reference the CDF coil is 30MJ). Inside the tracking volume the value of $\sin \theta \times \int B_z d\ell$ along the trajectory of any particle reaching the solenoid is uniform to within 0.5%. This uniformity is achieved in the absence of a field-shaping iron return yoke by using two grades of conductor with higher current density near the ends of the coil. From the value of the field integral and the space point precision provided by the silicon and fiber tracking system, a momentum resolution of $\Delta p_T / p_T^2 \approx 0.002$ is expected. The SC coil plus cryostat is about 1.1 radiation lengths thick.

The solenoid is being built by Toshiba Corp. in Yokohama, Japan. They are under contract to provide the solenoid as specified by Fermilab. The contract was awarded in January 1995 and Toshiba presented its preliminary design to Fermilab in March 1995. Delivery of the magnet to Fermilab will occur in early 1997 after complete testing in Japan.

The cryogenic plant that supplies LHe for both the solenoid and the visible light photon counter (VLPC) readout devices is in the final stages of design and the initial stages of construction. After appropriate modifications to the DØ cryogenic services building, the Accelerator Division (AD) will provide the experiment with warm high pressure He. The expansion engines and heat exchangers used in making LHe, will be located in the DØ Assembly Hall. Modifications to the AD cryo building began in the 1995 summer shutdown and are largely complete.

2.2 The Silicon Vertex Detector

The tracking system is designed to meet several goals: momentum measurement with the introduction of a solenoidal field; good electron identification and e/π rejection (to compensate for the loss of the Run I transition radiation detector); tracking over a large range in pseudo-rapidity ($\eta \approx \pm 3$); secondary vertex measurement for identification of b -jets from top and for b -physics; hardware tracking trigger; fast detector response to enable operation with a bunch crossing time of 132 ns; and radiation hardness. The silicon tracker [4] is the high resolution part of the tracking system and is the first set of detectors encountered by particles emerging from the collision.

Several of the Run II Collider machine parameters have an effect on the silicon design. The luminosity sets a scale for the radiation damage expected over the life of the detector, which in turn dictates the operating temperature ($< 10^\circ\text{C}$). The long luminous region length sets the length scale, and motivates our hybrid disk and barrel design. The crossing interval sets the design parameters for the electronics and readout.

Since the Collider interaction point is extended, with a σ_z of 25 cm, it is difficult to deploy detectors such that the tracks are generally perpendicular to detector surfaces for all η . This forces us to a hybrid system, with barrel detectors measuring primarily the r - ϕ coordinate and disk detectors which measure r - z as well as r - ϕ . Thus vertices for high η particles are reconstructed in three dimensions by the disks, and vertices of particles at small η are determined by the barrels.

The interspersed disk and barrel design is shown in Fig. 2. In such a system, the disk separation must be kept small to minimize extrapolation errors. However, each plane of disks also introduces a dead region between the barrels which lowers the overall efficiency of the detector. Thus there is a compromise between vertex resolution at large η and efficiency at small values of η . This design clearly puts a premium on minimizing the gap between barrel sections. The modular design also provides flexibility. Our baseline design includes six barrels with the more expensive 90 degree double metal technology detectors used only in the central modules:

- 6 barrel segments in z
- 4 detector layers per barrel
 - Layers 1 (innermost) and 3 are divided into the central and end regions and consist of:
 - * double-sided detectors (axial and 90° z -strips) in the central 4 barrel segments
 - * single-sided detectors (axial strips) in the out most barrel segment at each end
 - Layers 2 and 4 are double-sided detectors (axial strips and 2° stereo strips)
- 12 small diameter, double-sided “F” disks (30° stereo, 4 sandwiched between barrel segments)
- 4 large diameter, single-sided “H” disks (15° stereo)

The 12 cm long barrel segments are separated by 8 mm gaps containing F disks. Four more F disks are located at each end of the barrel. The H disks are located at $|z| \approx 110$ cm and 120 cm. The individual channel count for layer 1, 2, 3 and 4 is $\sim 46\text{k}$, 83k , 92k and 166k respectively. It is 258k for F disks and 147k for H disks, resulting in a total channel count of $\sim 793\text{k}$.

2.2.1 Silicon Detectors

The barrels and the F disks are based on 50 and $62.5\text{ }\mu\text{m}$ pitch silicon microstrip detectors, $300\text{ }\mu\text{m}$ thick, providing a spatial resolution of approximately $10\text{ }\mu\text{m}$. The small angle stereo detectors provide the pattern recognition necessary to resolve tracks from b decays within jets. The 90 degree detectors provide resolution in r - z at the vertex of $100\text{ }\mu\text{m}$, allowing identification of decay fragments by impact parameter in the r - z plane. The detectors are AC coupled; each strip has an integrated coupling capacitor and a polysilicon bias resistor. This technology has been shown to be sufficiently radiation hard [5]. F disks are made from 12 double-sided detectors which have $\pm 15^\circ$ stereo strips. Figs. 3 and 4 show cross sectional views in the $r - \phi$ plane of the barrel and F disk, respectively.

Results from tests of prototype F disk and barrel detectors fabricated at Micron Semiconductor (UK) have shown that these detectors are suitable for use in DØ [6]. Leakage currents were $< 120\text{ nA/cm}^2$; coupling capacitors had a capacitance of $> 20\text{ pF/cm}$ and a breakdown of $> 100\text{ V}$; and the polysilicon resistance was $> 3.5\text{ M}\Omega$ with strip-to-strip non-uniformity of $< 3\%$.

We have completed a series of radiation damage tests, the first at TRIUMF in April 1995 and subsequently in several test beam runs at the Fermilab Booster using 8 GeV protons at doses up to several Mrad. We verified the radiation hardness of the production barrel detectors and found deficiencies in the guard ring design of the F-disk prototypes resulting in higher than expected guard ring currents. This has been understood and corrected in the new designs for the double-sided barrel and disk detectors.

The SVX II front end readout chips (see Section 2.4) are mounted on a kapton high density circuit (HDI) which is laminated onto a $300\text{ }\mu\text{m}$ thick beryllium plate and glued to the surface of the detector. The end of the HDI consists of a kapton strip cable which carries signals and bias voltages to the outer radius of the detector ($\approx 18\text{ cm}$) where a connection to a long ($\approx 8\text{ m}$) low mass microstrip cable is made. These cables carry the signals to the port cards located on the DØ support platform.

2.2.2 Mechanical Support

The mechanical structure must provide a precise and stable support for the individual barrel and disk detectors, provide cooling for the heat generated in the SVX II chips and allow for the necessary cable paths for external connections. In the barrels, the basic mechanical unit is the ladder. Each ladder supports two detectors wire-bonded together, forming a 12 cm long unit with the SVX II readout at one end. Rohacell-carbon fiber support rails provide extra rigidity

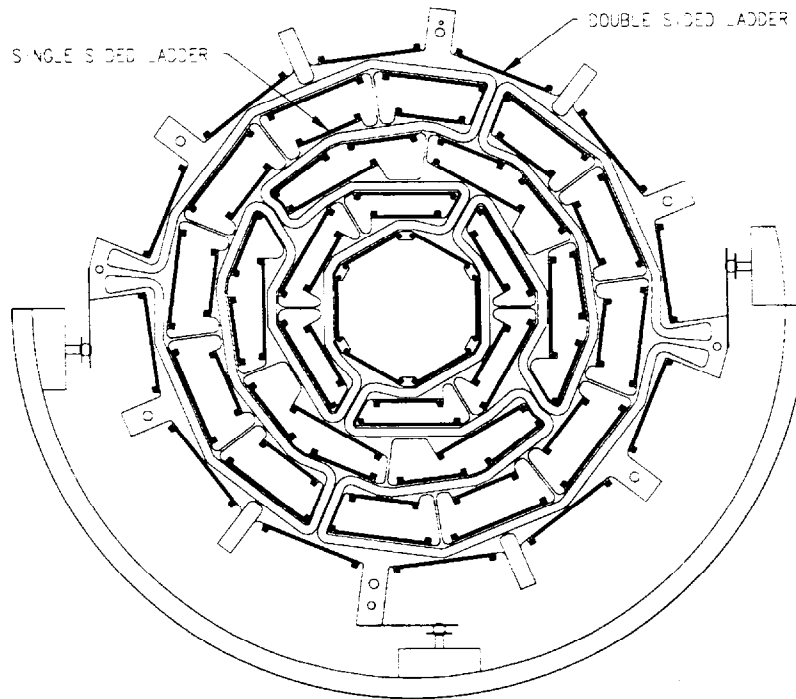


Figure 3: Cross sectional ($r - \phi$) view of the barrel detector.

to the ladder.

Ladder mechanical designs for single-sided and double-sided ladders (Fig. 5) are complete. Prototype single-sided ladders were assembled in the Lab D Silicon Detector Facility at Fermilab. The ladders were successfully tested using a laser test stand with full readout of the SVX II chips. The detailed procedures, ladder fixturing and traveller are all in place for ladder production.

The ladders are mounted on beryllium bulkheads, which serve as a support at both ends of the ladder and provide cooling at the readout end by means of an integrated coolant channel. The final bulkhead design is finished and orders placed for all the bulkheads.

The F disks are mounted in the 8 mm gap between the barrel segments. In analogy to ladders, disk modules consist of a single F disk detector with SVX II readout at the outer radius. Water cooling is via a beryllium cooling channel which also supports the modules at the outer radius.

The barrels and disks are mounted in a double-walled carbon half-cylinder which acts as a

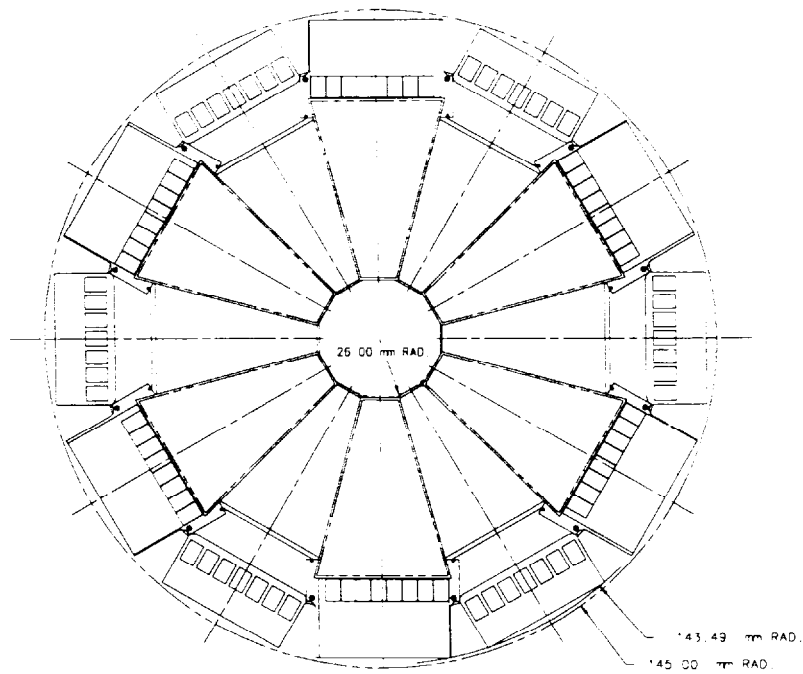


Figure 4: Cross sectional ($r - \phi$) view of the F disks.

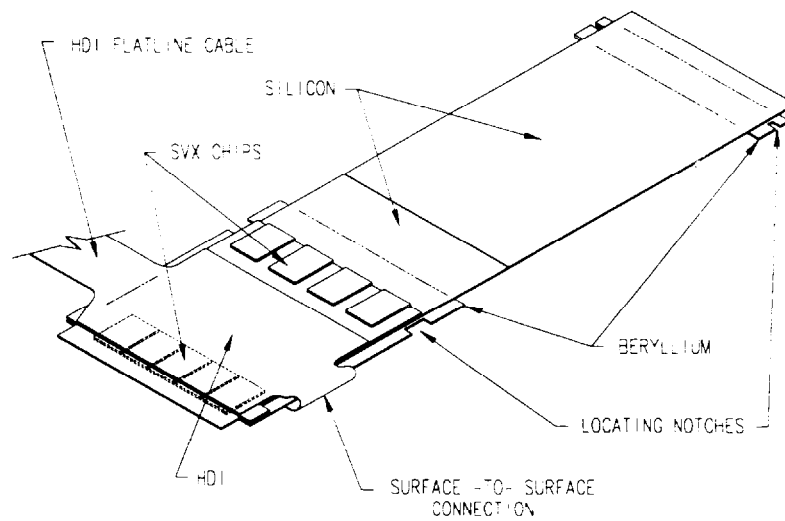


Figure 5: The layout of the ladder.

support with zero thermal expansion. The half-cylinder has a length of 1.66 m and an outer radius of 15.3 cm. A prototype half-cylinder has been fabricated and deflection tested. We found a maximum deflection under load of $75\text{ }\mu\text{m}$, well within our specifications of $100\text{ }\mu\text{m}$. During assembly of the final detector, as detector elements are installed, compensation will be made for the half-cylinder gravitational deflection.

The cooling of ladders has received considerable attention, as it is important to keep the detectors cool to avoid excessive radiation damage to the inner silicon layer. Finite element analysis and tests with prototype ladders have yielded good agreement and show a maximum temperature in the silicon of 10°C . This is low enough to ensure that the silicon survives for Run II at the Tevatron.

2.2.3 Assembly and Testing

Barrel and disk modules will undergo thorough testing to avoid using modules with unacceptable fractions of dead channels. This is being done in stages, starting with probe testing of the individual silicon detectors and SVX II chips. Due to the large numbers involved, three sites have been set up with probe station facilities. Probe testing of the first 200 detectors from Micron, is already well underway.

Further testing of HDI's instrumented with SVX II chips will be performed and, finally, the fully assembled ladders and disk modules will be checked with a 1064 nm wavelength laser, which simulates a charged particle track traversing the silicon.

2.3 The Scintillating Fiber Tracker

A scintillating fiber tracker surrounds the silicon vertex detector and covers the central pseudorapidity region. The fiber tracker serves two main functions. First, with the silicon vertex detector, the tracker enables track reconstruction and momentum measurement for all charged particles within the range $|\eta| < 2.0$. Second, the fiber tracker provides fast, “Level 1” track triggering within the range $|\eta| < 1.6$. Combining information from the tracker with the muon and preshower detectors, triggers for both single muons and electrons will be formed at Level 1. These triggers will be critical to take full advantage of the physics opportunities available with the Main Injector.

The scintillating fiber tracker is shown in Fig. 2. A total of about 74,000 scintillating fibers are mounted on eight concentric cylinders at radii of 19.5, 23.4, 28.1, 32.8, 37.5, 42.1, 48.8, and 51.5 cm. Each of the cylinders supports a doublet layer of fibers oriented in the axial direction, parallel to the beam line. Cylinders at odd numbered radii support two additional doublet layers of fibers that are oriented at $\pm(2.0^\circ \text{ to } 3.0^\circ)$ stereo angles. All doublet fiber layers are constructed so that one layer of the doublet is offset by one half of the fiber spacing with respect to its partner. This configuration compensates for the geometric gaps between adjacent fibers in a monolayer and provides near-unity detection efficiency per doublet. We have measured the tracking performance of doublet fiber layers extensively in tests of several thousand fiber channels with cosmic rays. Spatial resolution per doublet of $\sim 100 \mu\text{m}$ and detection efficiency per doublet $> 99\%$ have been measured. Based on these results, we have modeled the performance of the fiber-tracker for tracking and triggering using GEANT-based Monte Carlo simulations. The expected performance is excellent.

2.3.1 Scintillating Fibers

The basic detection element is the multi-clad scintillating fiber. The inner polystyrene core is surrounded by a thin acrylic cladding, which in turn is covered by a thin fluoro-acrylic cladding. These three materials have indices of refraction of 1.59, 1.49 and 1.42, respectively. The addition of the second cladding increases the light trapping by about 70% with respect to single-clad fibers and, additionally, improves the mechanical robustness of the fibers. The fiber diameter is $835 \mu\text{m}$ and each cladding is $15 \mu\text{m}$ thick. The polystyrene core of the fibers is doped with 1% p-terphenyl (PTP) and 1500 ppm of 3-hydroxyflavone (3HF). The fiber scintillates in the yellow-green part of the visible spectrum, with a peak emission wavelength near 530 nm.

Eleven-meter-long clear multiclاد fiber waveguides are mated to the scintillating fibers by plastic, diamond-finished optical connectors. These waveguides conduct the scintillation light to photodetectors that are situated in cryostats on the DØ platform under the central calorimeter.

2.3.2 Photodetectors

The photodetector must be capable of detecting single photons with high efficiency at high rates and with large gain. We will use the Visible Light Photon Counter (VLPC) [7], a variant of the solid-state photomultiplier. Much research and development in collaboration with Rockwell International Science and Electro-Optical Centers (Anaheim, CA) has led to a device with the following characteristics: $\sim 70\%$ quantum efficiency for the wavelength range of interest, gain of roughly 20,000, and a rate capability of at least 10 MHz. The VLPC can be operated at full efficiency with a noise rate of 0.1% or less. The VLPC's are manufactured in arrays containing 8 circular pixels each 1 mm in diameter, well-matched to the clear waveguide fibers. The VLPC operate with a bias voltage of 6.5–7.5 V and at a temperature of 6.5–14 K, depending upon the version used. The operating temperature range requires that the detectors be maintained in a cryogenic environment. Cryogenic “cassettes” have been prototyped which will each house 128 arrays (for a total of 1024 channels) and maintain them at a stable operating temperature.

2.3.3 Cosmic Ray Test Setup

The R&D program to develop the fiber system culminated in the operation of a large-scale scintillating fiber cosmic ray test stand at Fermilab. In one configuration, the test stand consisted of three superlayers, each containing two axial fiber doublets and two stereo fiber doublets, for a total of 3072 fibers. Two of the superlayers were mounted at the top and bottom of a carbon-fiber support cylinder; a third superlayer was mounted on a flat board on the cylinder axis. Muons with momenta greater than 2.5 GeV/c were selected using a steel filter. The cosmic ray setup was designed to test the major components of the fiber tracker in a configuration similar to the final tracker design. The scintillating fibers were three meters in length, and were optically coupled to eight-meter-long clear waveguides. A cryostat was built to house test cassettes containing 128 VLPC channels each. The test stand was in operation from May through December 1994. A second configuration consisting of three fiber superlayers, mounted on flat boards and incorporating improved fiber ribbon placement techniques, was tested using the cosmic ray test stand to verify expected improvements in spatial resolution. This configuration contained 1785 fiber channels (all oriented in the axial direction) and was tested over a 4 month period in March through June 1995.

The results [8] of the cosmic ray tests were excellent. The VLPC cryostat operated stably and the temperatures of individual cassettes were controlled to better than ± 15 mK, well exceeding the stability required for the VLPC operation. The gain of each of the 3072 channels was monitored by an LED-based calibration system, and overall gains were found to vary less than 1% over the length of the run. The noise rate, which was fixed to 0.1% by setting thresholds on each VLPC channel, also remained constant over the entire run. The light yield and tracking resolution are consistent with expectations. Figure 6(a) shows the light yield spectrum in photoelectrons for all fibers found on tracks. The most likely value of 8.5 (see Fig. 6(a)) photoelectrons is about a factor of four more than the minimum required for efficient tracking. There was no evidence of any degradation in light yield over the duration of the run. The doublet hit efficiency for cosmic ray tracks is better than 99.9%. The doublet position resolution, plotted in Fig. 6(b) is found to be ~ 100 μm .

2.3.4 R&D and Design

Currently, several R&D tasks are being completed before construction of the fiber tracker begins. Designs for the fiber ribbon manufacture and for the optical connectors are being finalized. Engineering designs and studies of low-mass composite support cylinders are in progress. A joint Fermilab-Rockwell project to build the prototype 1024 channel VLPC cassette is well underway. Characterization of various VLPC device versions under very high rate conditions of illumination are in progress. Prototypes for the final calibration system are being tested. Pending the successful completion of these studies, we expect actual construction of the fiber tracker to begin on schedule.

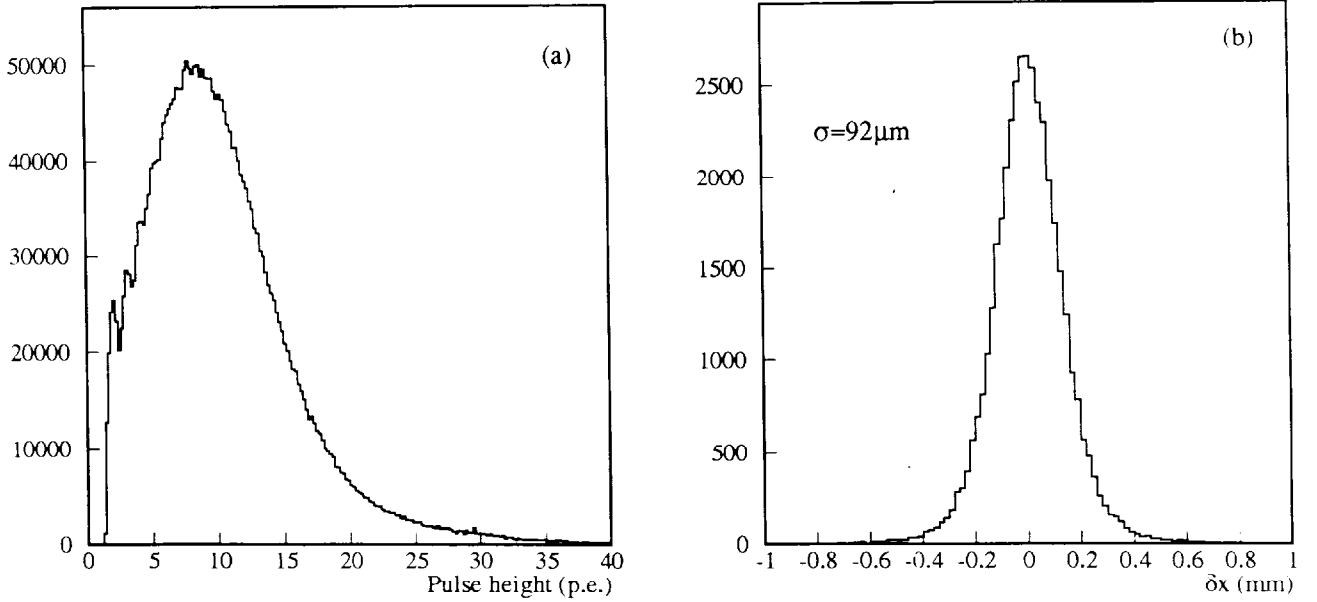


Figure 6: Results from cosmic-ray test: (a) light yield (in the unit of photoelectrons) distribution for all fibers on the track, and (b) position resolution for the fiber doublet.

2.4 Tracking Electronics

2.4.1 SVX II Chip

The readout for both the silicon vertex detector and the fiber tracker is based on the 128 channel SVX II chip [9] developed by Fermilab and LBL. Each channel contains a double-correlated sampling charge sensitive preamp, 32 stages of analog pipeline delay, a Wilkinson 8 bit analog to digital converter and a sparse data readout system ($< 5 \mu\text{s}$ for $\sim 3\%$ occupancy). The readout system employs a common digital threshold for all 128 channels. It also implements a 'nearest neighbor' readout scheme in which two channels below threshold neighboring a channel above threshold will also be read out. The chip is designed to accept data every 132 ns. At this crossing frequency, the 32 channel delay stage provides $4.2 \mu\text{s}$ for the Level 1 trigger decision. For the silicon tracking system, this chip is mounted directly on the detector. Four iterations of the SVX II chip have been prototyped in standard CMOS and tested. All parts of the chip are fully functional and the noise has been measured to be $\sigma = 600e + 65e/\text{pF}$ for a risetime of 105 ns. Tests of the radiation hard version have been completed and a production order has placed with UTMC.

2.4.2 Silicon Readout

Figure 7 is a block diagram of the silicon readout system. The SVX II's are controlled by a readout card, called a port card, which is mounted in the detector platform. The silicon detector is connected to the port card by two metallic cables. The first is an 8 foot long flat transmission line made from copper and aluminum clad Kapton while the second is a commercial ribbon coax. The two cables are connected together with a printed circuit board located on the face of the central cryostat. The port card downloads the parameters to the SVX II chips, controls the chip during data taking, reads out the data after a Level 1 trigger and converts the data to optical signals and sends these signals over fiber optic cables to the moving counting house. It also provides temperature, voltage and current monitoring and some level of diagnostics. It generates the test pulse signal for the SVX II.

The optical signals are received in the Moving Counting House by the VME Readout Buffer (VRB) a VME board that acts as a buffer for transferring data to the Level 3 system. Events are held in one of eight local buffers until a valid Level 2 accept is received, when they are sent to the existing VME buffer driver (VBD) for transmission to the Level 3 system. Level 2 rejects are discarded.

2.4.3 Fiber Tracker Readout

The front-end electronics for the fiber tracker must provide a prompt Level 1 trigger pickoff, necessitating the development of a special 'precursor' chip between the VLPC and the SVX II. Each channel of this chip has a charge sensitive amplifier, a discriminator with TTL output and a buffer amplifier to put charge onto an output capacitor which is read by the SVX II chip. In order to prevent the chip from oscillating, the trigger is picked off at a different clock cycle

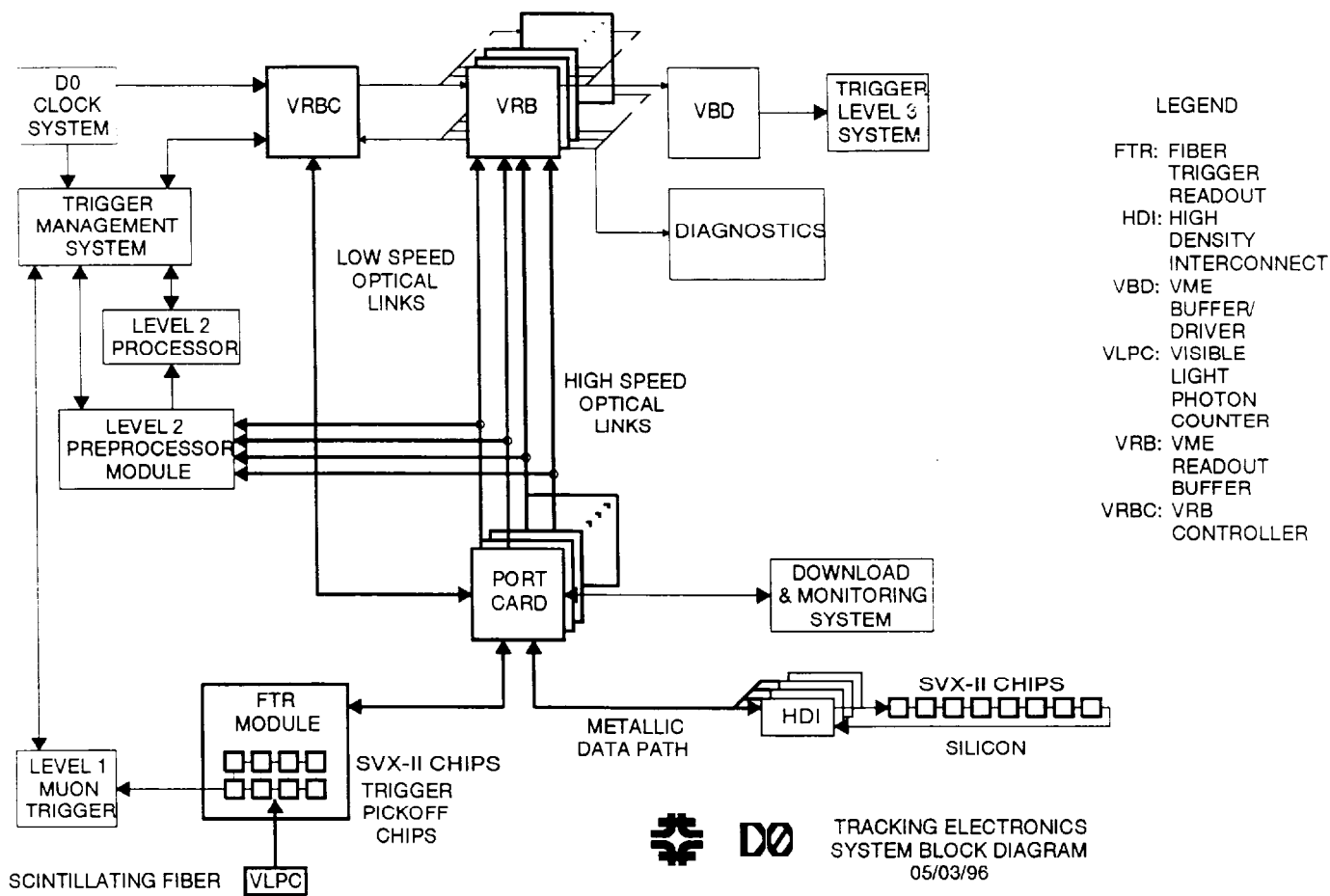


Figure 7: Block diagram of the readout system for the silicon detector and the fiber tracker.

than both the input and the transfer to the SVX II. The readout after the SVX II is nearly identical to that for the silicon system as shown in Fig. 7.

The trigger scheme for the fiber tracker is based upon the $r - \phi$ hit patterns in 4.5 degree sectors and allows four distinct momentum thresholds. The output from the trigger pickoff chip is fed into a series of large Field Programmable Gate Arrays (FPGA) which are preloaded with the appropriate logic to form hits from the eight trigger layers. The FPGA's are static RAM based, so thresholds are software settable. Trigger data is combined with the preshower detector on the trigger board and sent serially at 424 MHz to other trigger systems.

2.5 The Preshower Detectors

2.5.1 Central Preshower

The central preshower detector (CPS) [10] is designed to aid electron identification and triggering and to correct electromagnetic energy for effects of the solenoid. The detector functions as a calorimeter by early energy sampling and as a tracker by providing precise position measurements. The cylindrical detector is placed in the 51 mm gap between the solenoid coil and the central calorimeter cryostat at a radius of 72 cm, and covers the region $-1.2 < \eta < 1.2$. The detector consists of three layers of scintillating strips arranged in axial and stereo views with a wavelength-shifting (WLS) fiber readout. The stereo angles for the two stereo layers are $\sim \pm 23^\circ$. Cross-sectional end and side views of the detector are shown in Fig. 8. A lead absorber before the detector will be tapered in z so the solenoid plus lead total two radiation lengths of material for all particle trajectories.

The fast energy and position measurements enable use of preshower information at the trigger level to aid electron identification. The axial layer of the preshower will be used in the Level 1 electron trigger. Monte Carlo studies show that the information from the preshower detector will provide a factor of 3–5 reduction in the trigger rate by applying a pulse height cut and requiring coarse position-matching with tracks. Off-line, the early sampling of the showers and the good position resolution of the detector will provide additional means for identifying electrons and therefore enhances the capability for tagging b -quark jets through their semi-electronic decays.

To facilitate the detector construction, each layer will be made into 8 octants each ~ 270 cm long. The WLS fibers will be split at $z = 0$ and are connected to the clear fibers at both ends of each octant. The fiber splitting at $z = 0$ effectively halves the occupancy for each channel and therefore makes the detector less vulnerable to high rates. The clear fibers from each end of the octants will be grouped together to form one bundle. There will be 24 octants, 48 clear-fiber bundles and a total of 7680 readout channels for the detector.

After an extensive R&D, the scintillating strips of equilateral triangular cross section made through extrusion are chosen for the design. The triangular cross section has a base of ~ 7 mm with a 1 mm diameter hole in the center for housing the WLS fiber. The strips wrapped with aluminized mylar are nested to form layers as shown in Fig. 8. This design improves the position resolution for minimum ionizing particles (MIP) as a result of the light sharing between two neighboring strips. Cosmic-ray tests show that the design has a considerable margin in achieving the performance specifications of the preshower detector. A light yield of 4 photoelectrons per millimeter of scintillator traversed and an effective attenuation length of about 9 m with the silvered non-readout end of the WLS fiber have been achieved for cosmic-ray muons. The detailed test results are summarized in Ref. [11].

The scintillation light from the preshower detector will be transported over ~ 10 m long clear light-guide fibers to the VLPCs. The readout electronics will be again based on the SVX II. Before the VLPC signals are sent to the SVX II chips for amplification and digitization, they will be split into two channels each by special chips designed for the preshower to allow for fast trigger pick-off and to effectively extend the dynamic range of the readout system. To

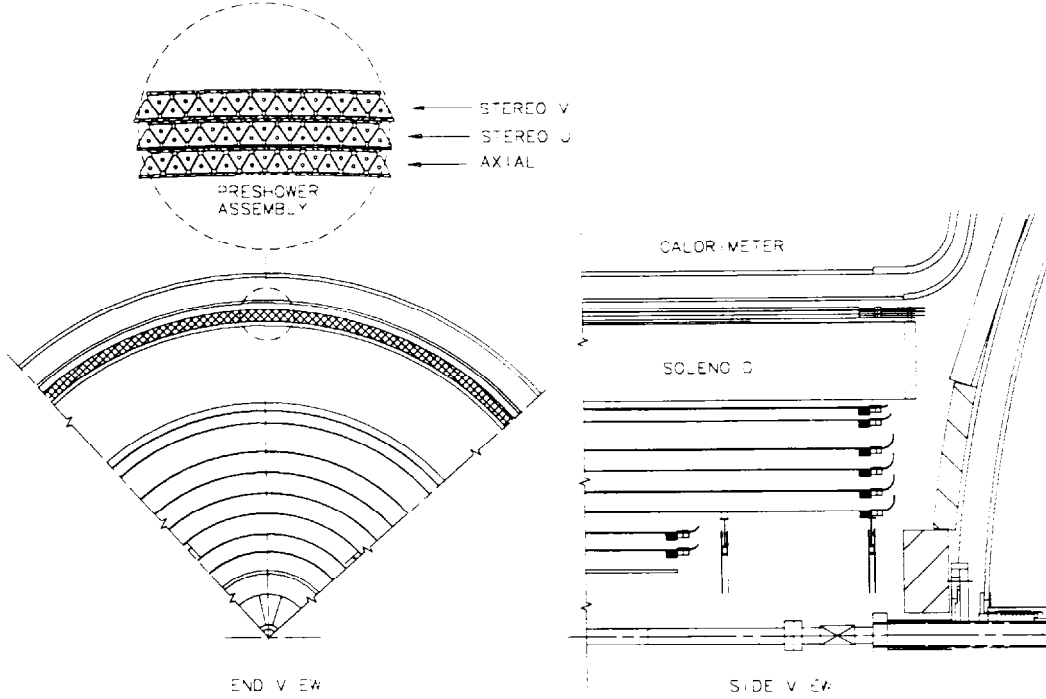


Figure 8: Cross sectional end (left) and side (right) views of the central preshower detector with the inset of the triangular strip assembly.

facilitate the Level 1 electron trigger discussed in Section 2.8, the readout for the axial layer will be integrated with the fiber tracker readout as the ninth layer.

Calibration of the detector will be done in two steps. Light emitting diodes (LED) will be utilized to provide a quick calibration on-line. The WLS fibers will be excited by blue LED's at the ends of the detector. By comparing the one and two photoelectron peaks from the LED light, the relative calibration of the detector elements can be performed. An absolute calibration will be provided by MIP responses of the detector using data. The Monte Carlo studies show that the MIP peak can easily be identified.

2.5.2 Forward Preshower

The DØ Forward Preshower Detector (FPS) [12], like its counterpart in the central region, is intended to enhance our electron identification capability by making precision position measurements of particle trajectories using dE/dx and showering information collected just upstream of the calorimeter. Monte Carlo simulations have shown that, relative to using the calorimeter alone, implementation of trigger algorithms that integrate FPS information reduces the Level

1 output rate by a factor of 2-4 (3-7 for Level 2), with no significant reduction in efficiency. In addition, these studies have demonstrated that substantial improvements in offline electron identification and γ/π^0 separation can be expected when FPS information is appropriately applied.

Two FPS detectors will cover the pseudorapidity range $1.4 < |\eta| < 2.5$, with one detector mounted on the inner face of each of the End Calorimeter (EC) cryostats (see Fig. 9). In order to make the most effective use of the limited amount of available space in the region, the detectors will be made to conform to the outer shell of the cryostats.

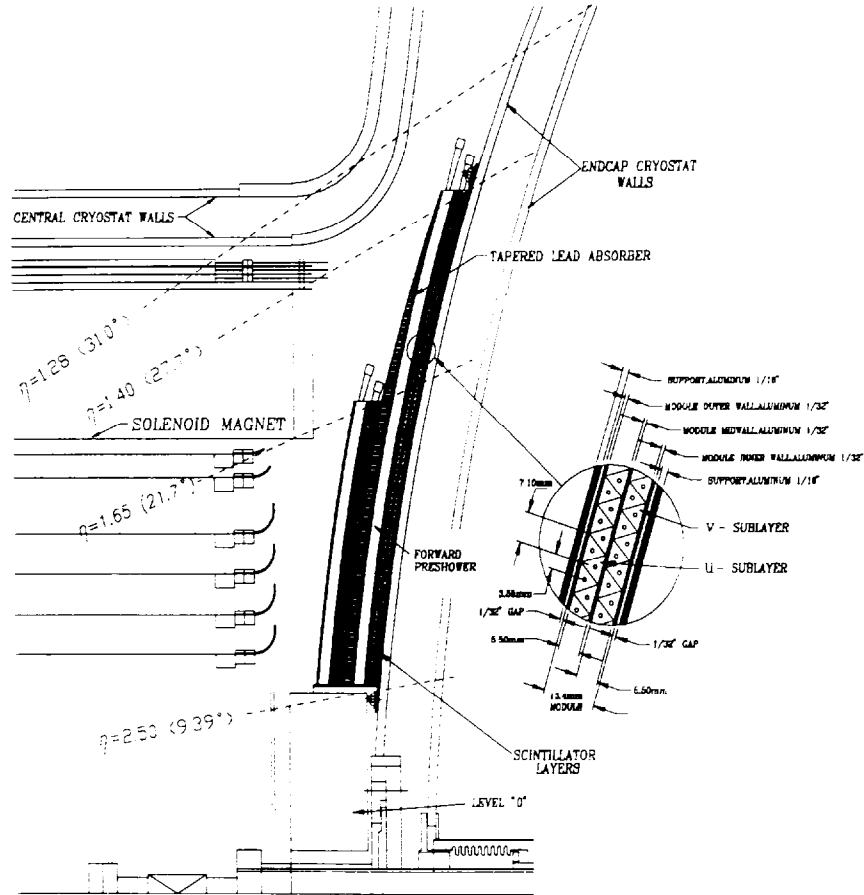


Figure 9: One quarter view of forward preshower detector, with detail of a scintillator u - v layer.

We have opted to pursue the same technology for the FPS as that being used for the central preshower: triangular scintillator strips with embedded wavelength-shifting fibers, read out by visible light photon counters. The detector will be composed of a layer of lead absorber of two radiation length thick sandwiched between two active scintillator planes, with each scintillator plane consisting of one u and one v sublayer.

The FPS will be segmented longitudinally into four structurally distinct layers, with each layer consisting of eight azimuthal wedges or modules. Each module will subtend 45° (one

octant) in ϕ , and will consist of both a u and a v scintillator sublayer. The central 22.5° of each module will consist of active scintillator volume. The remaining $\approx 11^\circ$ on either side of the active region provides space and mechanical support for routing the WLS fibers from the end of the scintillator strips, which are oriented perpendicular to the radial edge defined by the active volume of the module, to the outer radius of the detector. The module positions in successive layers will be staggered by 22.5° in order to cover the full azimuthal angle.

Connectors that couple to WLS fibers on the detector end, and clear transmission fibers on the other, will be mounted at the end of each fiber-routing channel at the periphery of the detector. The clear fiber is routed about the circumference of the FPS and down to the platform below the detector, where the VLPCs are housed.

Since particles traversing the magnet solenoid ($1.4 < |\eta| < 1.6$) are likely to shower upstream of the FPS, the mip-detecting scintillator (or inner) layer in front of the lead absorber will not be needed in this pseudorapidity range. The inner (outer) scintillator layer, therefore, will cover the pseudorapidity range $1.6 < |\eta| < 2.5$ ($1.4 < |\eta| < 2.5$). The lead will consist of two radiation lengths in the high- η region, and will be tapered in the region $1.4 < |\eta| < 1.6$ in order to equalize the amount of material traversed as a function of pseudorapidity.

Based on our studies, we anticipate that a strip width of ≈ 8.1 mm and a strip height of ≈ 5.5 mm will provide the required performance. This yields a total channel count (for both FPS) of 16,000 channels.

The conceptual and practical design of the FPS has already benefited substantially from the design work of the CPS group. The approach to FPS connector design, detector calibration and temperature monitoring, fiber bundling, and scintillator extrusion will be based on CPS R&D, with appropriate modifications being introduced as they are warranted. The basic readout and calibration systems, discussed in more detail in the CPS section above, are two examples of design schemes that we expect to carry over directly from the CPS. The reader is referred to Ref. [12] for further details on the conceptual and mechanical design of the FPS detector.

2.6 The Calorimeter System

The Calorimeter system upgrade is driven by the need to preserve the excellent performance of the calorimeter for Run II running conditions. We have chosen not to make any modifications to the uranium liquid–argon calorimeter itself, but to restrict all the changes to the front–end electronics. The phototubes for the Intercryostat Detector (ICD) readout will be moved to a field free region.

2.6.1 Calorimeter Front–End Electronics

An upgrade of the calorimeter front–end electronics is required because the minimum bunch crossing time will be reduced and the luminosity will be increased in Run II. These changed conditions require a re–optimization of the three noise components: electronics noise, uranium noise, and pile–up noise. This optimization is achieved by shortening the effective integration time and reducing the intrinsic noise of the pre–amplifier within practical limits. The electronics upgrade will preserve as much of the existing infrastructure as possible.

To minimize the effects of pile–up in the calorimeter, we have re–optimized the shaping times. The present peak sampling time of $2.2\ \mu\text{s}$ will be reduced to 400 ns (matching both the charge drift times in the calorimeter and the expected minimum bunch–spacing at the start of Run II). Since this shorter shaping time increases the sensitivity to noise and reflections on the signal cables, we will replace the present cables from the calorimeter cryostat with cables that are impedance matched (30Ω) to both the cables inside the cryostat and the new preamp input impedance. The calorimeter signals are transported to preamps housed on the surface of calorimeter. The present preamp hybrids will be replaced with new hybrids which will have better noise performance through use of dual low–noise FETs, and increased output drive capability in order to drive the long terminated–cable run from the preamp to shaper circuitry (baseline subtractor or BLS). The new preamps require new preamp motherboards and power supplies, but otherwise use the existing mechanical structure.

The shaper circuitry incorporates significant new elements in the design to provide the necessary pipelining of the calorimeter signals to provide time for a trigger decision to be made. The analog pipeline will use a switched capacitor array (SCA) originally developed for SSC work by [13] LBL and modified to match DØ specifications. The SCA will sample the peak of the integrated charge signal from a preamp, shaped to provide a symmetric unipolar signal. The calorimeter signals require 12–bit accuracy with 15–bit dynamic range. This range requirement exceeds that which can be achieved with the SCAs, so a dual–pipeline will be used to accommodate the full dynamic range. To minimize the deadtime at high luminosity, the signals will be toggled between two dual–pipelines. Limiting the trigger to only one in a “superbunch” (a superbunch consists of 11 (or 33) bunches at 396 (or 132) ns spacing with about a $2\ \mu\text{s}$ gap between superbunches) provides a deadtimeless system in which one of the dual–pipelines is reading out while the other is being filled with data. The gap between superbunches will provide a single baseline sample which will be used to remove long term drifts. The present BLS system (60,000 channels) will be fully replaced (including new power supplies, timing system, and pulser system) except for the mechanical infrastructure (crates, cabling, cooling,

shielding).

The performance of the system with regard to pile-up has been simulated, and we find that the capability of the upgrade detector at high luminosity is comparable to that of the present detector at our present lower luminosities. Its performance at 132 ns has also been checked and found satisfactory up to luminosities approaching $10^{33} \text{ cm}^{-2}\text{s}^{-1}$.

2.6.2 The Intercryostat Detector

The Intercryostat Detector (ICD) [14] plays an important role in $D\bar{O}$ calorimetry, both in terms of measuring jet energy as well as missing transverse energy (\cancel{E}_T). In order to preserve the Run I calorimeter resolution, the ICD will be modified for Run II by relocating the photodetection readout outside of the high magnetic field environment expected in the inter-cryostat region.

This detector will consist of a single layer array of scintillating tile as the active element. The light signals, picked up by wavelength shifting fiber in the tiles, will be transported along clear fiber to the location of the photodetection readout via clear fiber ribbon cables (about 8 meters from the ICD tile location).

The phototubes and readout electronics will be distributed by quadrant onto the ‘trays’ that move within each of the four cable winders. The readout system will include Hamamatsu phototubes, many of which can be salvaged from the Run I detector. In this location, the field seen by the phototubes will be less than 500 gauss. A moderate level of shielding will be required.

An ICD tray will house a 2-dimensional array of slots holding the ICD drawers. The ICD drawers will house PMTs, PMT electronics, and preamplifiers for three or more channels of readout. The final number of channels per drawer will be determined based on how the readout signals are to be multiplexed to interface with the BLS system. Based on our experience with the Run I detector, occasional maintenance on the photodetection electronics will be required. Therefore, each drawer will slide individually on rails, making access to PMT and electronic components convenient.

2.7 The Muon System

2.7.1 Introduction

The design of the upgraded muon system [12] is driven by the DØ Run II physics goals and by the higher event rates and backgrounds expected in Run II. The physics motivations for going to the highest luminosities are to study low cross section, high- p_T processes, such as top and W/Z , and to search for new phenomena. In order to maximize the acceptance for muons from these processes, we need sufficient detector coverage and an efficient, unprescaled trigger. It has been shown that $|\eta|$ coverage to ~ 2 is required for DØ's physics goals to be met. The new design satisfies this requirement.

Triggering in the high rate environment of Run II requires the use of fast trigger elements with good time resolution. In the central region, the maximum drift time in the existing PDTs of 750 ns exceeds the Run II bunch spacing of 396 or 132 ns, and scintillators will provide the necessary time stamp. In the forward region, accidental triggers from uncorrelated particles in the three layers will be reduced by the use of scintillation counters.

The individual components of the new design will be discussed in more detail in subsequent sections; a brief overview is given here. In general, we have attempted to minimize the number of regional boundaries, chamber technologies, and distinct electronics boards. We have also built in hooks to allow a natural upgrade to $\mathcal{L} = 10^{33} \text{ cm}^{-2} \text{ s}^{-1}$.

The three layers of the muon system are designated A,B,C, where A is closest to the interaction region, and the toroid magnet is located between the A and B layers. For $|\eta| \lesssim 1$, the Wide Angle Muon System (WAMUS) PDTs will be retained but the electronics, from the front-ends to the Movable Counting House (MCH), will be replaced. There will be two layers of scintillator: the existing Central Muon Scintillator C-layer (CMSC C-layer) just outside the WAMUS C-layer PDTs and a new set of CMSC A-layer scintillation counters located between the calorimeter and the A-layer. There will be a CFT-CMSC A-layer trigger with good geometric acceptance that will enable a trigger on low- p_T muons ($\gtrsim 1.5 \text{ GeV}/c$) in the central region. There will also be a trigger based on the hits in the PDTs, as in Run I.

For the Forward Muon System (FAMUS), $1 < |\eta| < 2$, the PDTs will be replaced with planes of plastic Mini-Drift Tubes (MDTs). The cells are square in cross section and 1 cm wide. They will be arranged in three layers (A,B,C) with (4,3,3) decks of tubes per plane. There will be three layers (A,B,C) of Forward Muon Scintillator (FMSC) pixels arranged in an $r - \phi$ geometry. The trigger will be provided by a CFT-FMSC requirement. As in the central region, a Run I-style trigger based on the MDT wires will also be implemented, as this will give finer p_T resolution.

2.7.2 Shielding

The upgrade of the DØ muon system will include the addition of shielding material. This shielding will block non-muon background particles originating from the three hottest sources [15]. The main source is scattered proton and antiproton fragments which interact with both the

exit of the calorimeter (producing a background in the central and forward muon A-layer) and the beam pipe and low-beta quadrupoles (producing showers in the forward B and C-layers). (The accelerator-produced background which comes from the tunnel is small compared to the direct contribution from interactions thanks to improved shielding that was installed in the tunnel during Run I [16].) Shielding these background sources is important because it will reduce the occupancy of the detectors. This decreases the fake trigger and track probabilities and increases the detector lifetime by reducing aging.

The main feature of the B and C-layer shield is a thick iron, lead, and polyethylene casing surrounding the beam pipe and final low-beta quadrupole magnet. This extends from the calorimeter to the accelerator tunnel. The shield is ~ 170 cm wide on the outside and has an inside hole ~ 50 to 65 cm wide for the accelerator equipment.

The appropriate thicknesses of the iron, lead and polyethylene was determined by Monte Carlo simulations (GEANT and MARS) for various shielding configurations. Figure 10 (upper) shows the energy deposition from hadrons and electromagnetic showers in the Run I detector configuration for a luminosity of $2 \times 10^{32} \text{ cm}^{-2}\text{s}^{-1}$. Figure 10 (lower) depicts the energy deposition from hadrons and electromagnetic showers in the shielded detector. The effect of the shielding is striking. We find that the energy deposition from proton and antiproton remnants is reduced by approximately a factor of 100 with a shield comprised of 39 cm of iron, 15 cm of polyethylene, 2 cm of lead and an additional 8 cm of iron located on the inner core of the shield at the exit of the muon toroid in front of the low-beta quadrupole magnet. As a result, the number of hits in counters is expected to be reduced by about a factor of 40 [17].

Additional polyethylene shielding will be mounted in the gap between the End Calorimeters and the EF toroids to reduce the rates in the CF A-layer detectors due to shower propagation at the rear of the calorimeters through the liquid argon and insulating vacuum space.

2.7.3 Central Muon Detectors

A. WAMUS

The WAMUS central region consists of three layers of drift chambers, one layer inside and two layers outside the iron toroid magnet. The purpose is to provide muon identification and a confirming momentum measurement independent of the central tracking. The muon momentum resolution in the central region in Run II will be dominated by the central tracking system. The WAMUS PDT's produce for each hit: the drift-time T perpendicular to the anode wire; the time difference, ΔT , in the arrival time of the hit between a hit cell and its neighbor (jumped at the far end) providing the distance along the wire; and the charge deposition on inner and outer vernier pads, yielding a more accurate measure of the distance along the wire. The Run II gas mixture will be 80% Argon, 10% CF_4 and 10% CH_4 which gives a maximum drift time of 450 ns and thus less event overlap compared to the Run I mixture. With this mixture the wires will operate at $\sim 5.0\text{kV}$ and the pads at $\sim 2.5\text{kV}$. The contribution to the hit uncertainty due to diffusion is estimated at less than $500 \mu\text{m}$, worse than the present $\sim 300 \mu\text{m}$, but smaller than the $700 \mu\text{m}$ residual typically achieved in WAMUS chambers during Run I. The trade-off

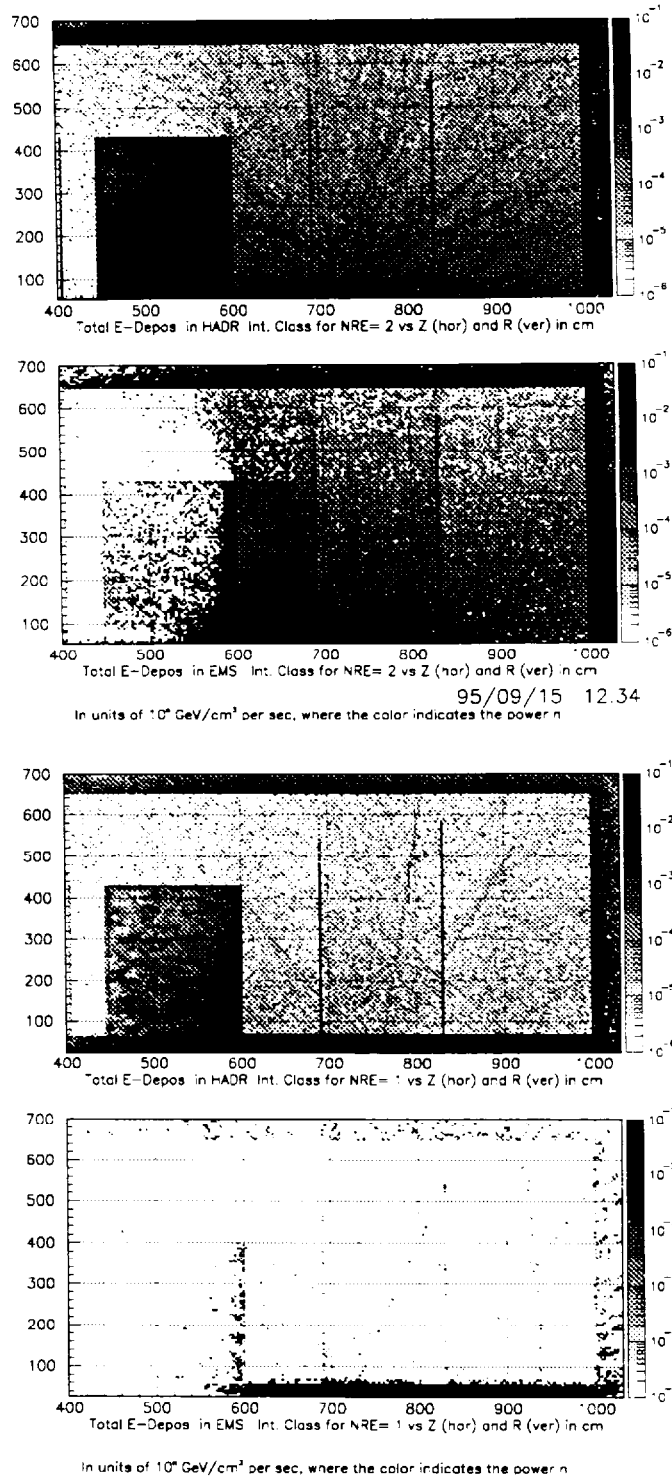


Figure 10: From top: Energy deposition from hadrons (1) and electromagnetic showers (2) in the unshielded detector. Energy deposition from hadrons (3) and electromagnetic showers (4) in the shielded detector. A luminosity of $2 \times 10^{32} \text{ cm}^{-2}\text{s}^{-1}$ is assumed.

in resolution is offset by the reduced occupancy and benefits to triggering and reconstruction achieved by decreasing the number of crossings in one drift time from 6 to 4 for 132 ns bunch spacing operation.

B. Central B- and C-layer Scintillation Counters

The existing CMSC C-layer counters [18] cover the top and sides of the central region with 12 divisions in ϕ and 20 divisions in z . The purpose is to provide a fast trigger detector outside of the toroid magnet and to tag the crossing for hits in the WAMUS B and C-layers. The background rate is small in comparison with other detector regions; very tight timing is not necessary to achieve adequate rejection. These counters exist and have been used during Run I to reject cosmic ray muons. They have achieved timing resolution of 2.5 ns after offline corrections (online, the counters have timing resolution of ~ 5 ns).

The bottom of the central region was not covered with scintillation counters during Run I but must be for Run II. The “CMSC Bottom” includes the CF Bottom B- and C-layer counters and the EF Bottom B-layer counters. The B-layer counters are needed for matching with the CFT in the region where there are no CMSC A-layer counters due to calorimeter support structures. Both B and C layer counters are needed to provide more complete coverage of the bottom quarter of the detector because of spatial constraints in each layer arising from support structures. The design is similar to the existing counters: scintillator sheets with wavelength shifting fibers for light collection. Forty counters will be located on the B-layer chambers underneath the CF muon toroid. These are referred to as the “CF B-layer Bottom” counters. A minor difference between these counters and those in the CMSC C-layer is that these counters will be oriented with the short dimension along ϕ so that they cover an interval of approximately $4\frac{1}{2}$ degrees. The smaller ϕ segmentation is advantageous for matching with the CFT trigger tracks. The EF B-layer bottom, located on the PDTs just underneath the North and South EF toroid magnets, consists of 36 counters 88 inches long and $15\frac{3}{4}$ inches wide. The CF C-layer Bottom counters are located underneath the north and south ends of the platform and consist of approximately 40 counters similar in design to those described above. The total number of CMSC B- and C-layer counters (including those already installed) is 356.

C. Central Muon Scintillator A-layer Counters

The CMSC A-layer counters [19] will be located between the Central Calorimeter and the WAMUS central A-layer PDTs. The purpose is to provide a ϕ measurement matching high and low p_T triggers with the central tracking system, and to reject out-of-time backgrounds originating at or near the exit of the calorimeter. The counters divide the A-layer into rows covering $4\frac{1}{2}$ degrees of ϕ . Each row contains nine counters that cover three 100 inch wide PDTs. The counter widths vary from 10 to 17 inches in order to maintain a constant segmentation in ϕ . The total number of CMSC A-layer counters is 630. Figure 11 shows a view of the CMSC A-layer scintillator array on the east or west A-layer wall. The scintillator is $\frac{1}{2}$ inch thick Bicron 404a and light collection is accomplished with Bicron G2 waveshifter fiber. This waveshifter has a fast (2.7 ns) decay time and is well-matched to the scintillator and PMTs. The photomultipliers are Russian MELZ 115M tubes which have a 1 inch diameter. Prototype counters have been studied with this configuration. Over the surface of the counter, the response

to minimum ionizing particles is constant to within $\sim 10\%$ with a timing spread of about 4.7 ns. We have operated test counters in the CF A-layer during Run I, and have verified that muons are well separated from the background and in good agreement with Monte Carlo [19].

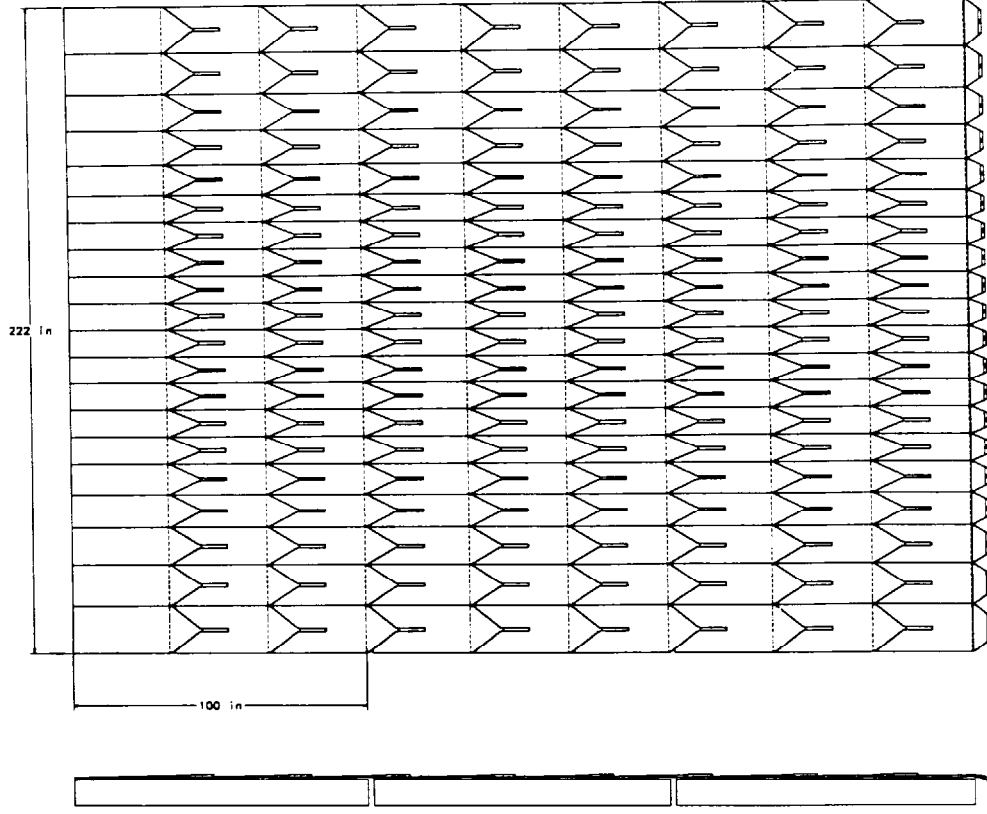


Figure 11: The CMSC A-layer counter array of the east or west wall A-layer.

2.7.4 Forward Muon Detectors

Plastic mini-drift proportional tube planes and scintillation counters will be used for forward muon triggering and track reconstruction. WAMUS PDT's in the forward region in Run I suffered a radiation induced buildup of material on the anode wires derived from the cathode pad polyresin material. Although a time consuming procedure exists to "clean" the PDT's, studies of PDT aging show that the number of such "cleanings" needed to maintain high chamber efficiency would be unacceptably high. For that reason the WAMUS PDT's will be replaced with mini-drift proportional tubes.

A. Mini Drift Tube System

The Mini Drift Tube (MDT) design has a $10 \times 10 \text{ mm}^2$ internal cross section with $50 \text{ }\mu\text{m}$ anode wires in the center of each cell. The cells, in packs of eight, are made from plastic

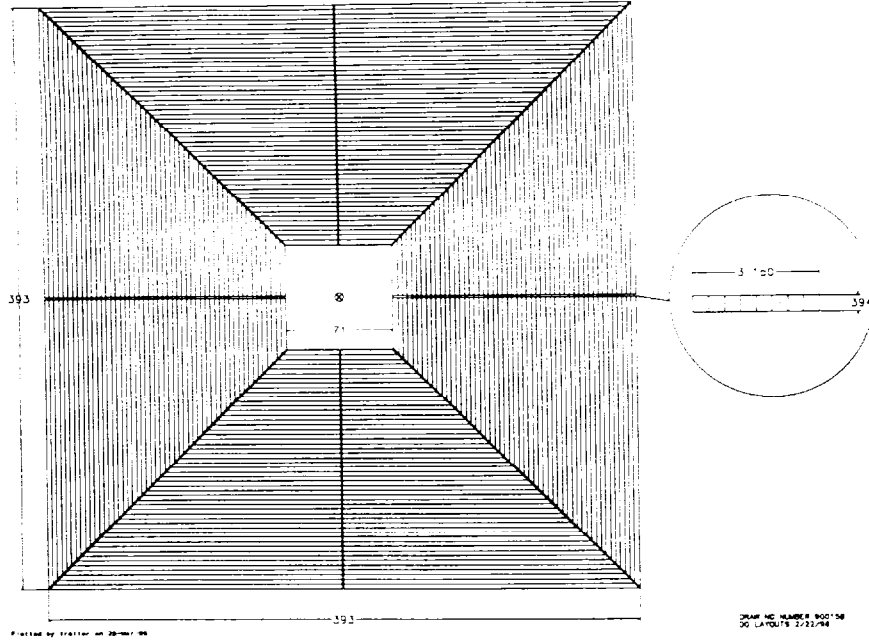


Figure 12: Mini Drift Tubes: individual 8 tube module and one complete plane.

extrusions as long as 5 m. The internal surfaces of the tubes are covered with conductive paint ($1 \text{ k}\Omega/\text{square}$) to form the cathode electrode. The extruded tube construction is the same as that used in Iarocci counters, which have been used extensively in collider experiments [20]. Iarocci tubes are usually operated in limited streamer mode with cathode readout, but in this application the tubes will be run in proportional mode with readout of the anode wires in order to facilitate high-rate operation. Filled with a fast gas mixture, such as $\text{Ar}(80\%)+\text{CF}_4(10\%)+\text{CH}_4(10\%)$, these tubes will have a maximum electron drift time of 60 ns. The planned gate width of 90 ns is well within the 132 ns bunch spacing. This constitutes a significant advantage over the larger drift cells in the WAMUS system.

The layout of one MDT plane is shown in Fig. 12. The tubes are oriented along magnetic field lines (the field shape in the EF toroids is more “square” than “circular”). The flux of particles decreases with increasing distance from the beam pipe, so the occupancy per cell is approximately constant: using the geometry shown in Fig. 12 the occupancy of individual cells will vary only a factor of two over the entire plane. The total number of MDT 8-cell modules is 6000 (48,000 individual channels).

The intrinsic efficiency of an individual MDT cell is near 100%, but due to the tube walls, the efficiency of a plane is 90% for normal incidence (1 mm wall/10 mm cell). We assume a single-layer efficiency around 92%, which corresponds to results from prototype studies at 45° incidence. In order to have a track vector from each layer, the planes will be separated by 20 mm. In order to reduce the probability of track segment formation by low energy electrons, the gap between the MDT planes will be filled with polyethylene. The energy of electrons from

neutron interactions is below 1 MeV and they can be absorbed by 5 mm of polyethylene.

The solenoid tracker momentum resolution falls off in the forward direction and the contribution from the muon system becomes significant. The momentum resolution of the muon system is limited by multiple scattering and the coordinate resolution of the muon detector. The typical coordinate resolution of WAMUS and Small Angle Muon System (SAMUS) detectors (per layer) in Run I was around 1 mm. However, mechanical inaccuracies, survey accuracy, and the time-to-distance calibration were the major factors limiting momentum resolution. Using MDT drift times measured with 18.8 ns time bins, the per layer effective coordinate resolution is around 0.8 mm, and thus not the limiting factor in the momentum resolution.

Experience with SAMUS tubes shows that an integrated charge of 50 C/cm on the anode wire can be accumulated without changes in gas amplification using a freon-methane gas mixture (similar to the one we propose for the MDT's). Preliminary studies of the MDTs show that there is no outgassing from their internal surfaces. This suggests that MDTs can run for many years at $\mathcal{L} = 1 \times 10^{33} \text{ cm}^{-2} \text{ s}^{-1}$ without aging. Studies of MDT aging with the selected gas mixture in the proportional mode show gain decreases of less than 2% for integrated charges of 2 C/cm. This charge is considerably more than that expected in the lifetime of the experiment.

B. Forward Scintillator Counters

The time and energy spectra of background particles are substantially different than those from real muons. Scintillation counters will register substantially fewer background hits than other types of detectors [19, 21]. Use of a 20 ns gate (compared to the 100 ns gate width of the MDT's) reduces the number of background hits per plane by a factor of five. The minimum ionizing energy deposition in one-half inch of plastic is 2.5 MeV. Setting a detection threshold at 0.5 MeV will reduce the counting rate due to neutrons by a factor of three compared to the rate seen by the MDT's [22].

There will be three layers of Forward Muon Scintillation counters (FMSC A-, B- and C-layers) with $\Delta\phi = 4.5^\circ$ and $\Delta\eta = 0.1$ segmentation in the forward region (Fig. 13). This segmentation has been optimized with respect to multiple scattering, the fiber tracker trigger azimuthal segmentation, the minimum muon momentum, background trigger rates, and the number of channels [23]. The minimum pixel size is dictated by the requirement of triggering efficiently on muons down to $p_T = 3 \text{ GeV}$, where the typical multiple scattering angle is about 3° . On the other hand, fine granularity is needed in order to keep the combinatoric backgrounds under control. Since the combinatoric rejection varies as n^3 for 3 layers of n scintillator pixels in coincidence with the CFT trigger, a factor of two coarser granularity would give almost an order of magnitude increase in accidental triggers. Each plane consists of two overlapped sub-planes in order to remove any dead zones between counters. The maximum counter size is $60 \times 110 \text{ cm}^2$.

A tower of three layers of prototype counters located at $\eta \approx 1.6$ was tested in Run I, at luminosities which correspond to the same average number of interactions/crossing that is expected in Run II at $\mathcal{L} = 2 \times 10^{32} \text{ cm}^{-2} \text{ s}^{-2}$ with 132 ns bunch spacing. These tests showed that the background hits in the three layers were largely uncorrelated. A three layer coincidence of the prototypes achieved a signal-to-background ratio of about 1:140. After corrections

for the expected reductions from shielding and the larger size of the actual trigger towers with respect to the prototypes, a signal-to-background of about 1:10 is expected from the scintillator coincidence alone. Additional rejection from the CFT and/or MDT planes should reduce the combinatoric background even further.

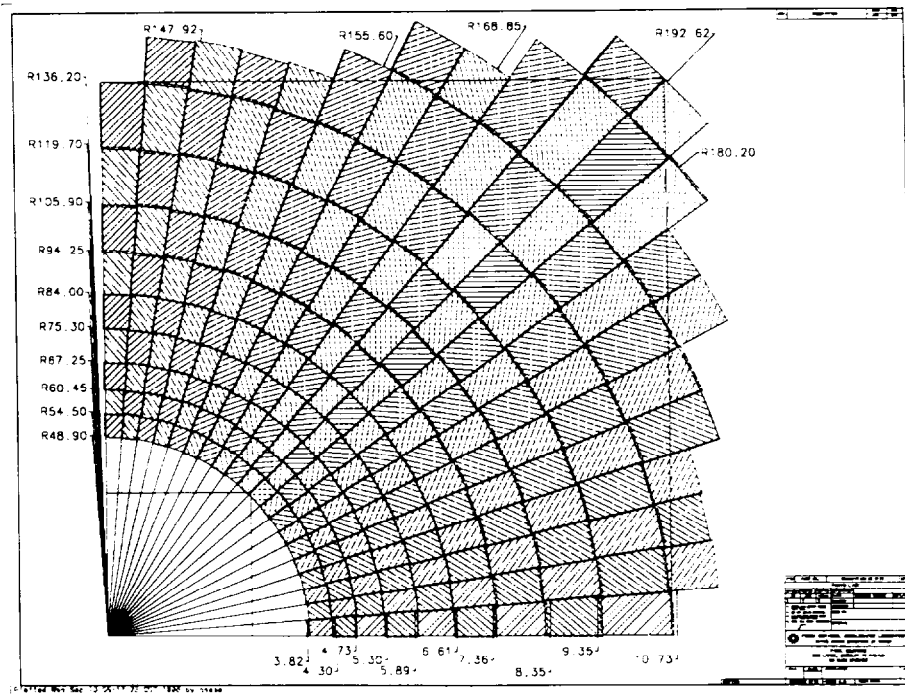


Figure 13: One quadrant of scintillation pixel plane.

There are two FMSC light collection schemes in the baseline design. The first is based on two wavelength shifting (WLS) bars used for collection of light into the photomultiplier [21]. The high transparency of Bicron BC404A one-half inch scintillator provides a large number of photoelectrons (more than 60 for the largest counters) and good uniformity (within $\pm 10\%$). In the second design, twelve 1 mm diameter WLS fibers (Bicron G2 fibers with decay time of 2.7ns) are installed around the counter perimeter to collect light from all four sides of the plastic. This design has the advantage of a better photomultiplier connection and counter design, but fewer photoelectrons and a more complex assembly/production procedure. The performance of these two optimized configurations is very similar. Results from test counters give about 60 photoelectrons from a minimum ionizing particle passing through the center of the counter and a time resolution of 0.8–1.4 ns. Both counter designs use 1 inch Russian MELZ 115M photomultipliers. The final choice will be driven by the design of the octant assembly.

The total number of FMSC counters is 4608. They are grouped into octants matching the MDT arrays. There are about 96 counters per octant.

2.7.5 Front-End Electronics

There will be new front-end electronics for all the muon detectors in Run II. The electronics design is well developed [24]. The readout part of the WAMUS electronics is the basic model for the fast trigger-detector electronics design.

A. Wire Amplifier

The wire amplifier design takes advantage of new, lower power, commercial IC's to achieve comparable noise performance to the present system. Performance improvements include the addition of transformer coupling at the high voltage distribution boards to provide a true differential connection and avoidance of low impedance ground paths between the chambers and the preamplifier inputs. The determination of which tube in a pair is hit will be achieved by separating the arrival time by about 20 ns, through the use of a lumped constant delay line in series with the jumper joining the far ends of the tube pair. Similar preamplifiers will be used for the FAMUS MDT system.

B. Time Digitization

The drift time measurement will be made with a four channel pipelined digital TDC chip (TMC) developed by Arai at KEK [25], which matches our needs very closely. The bin width, when run at 26 MHz, is 1.2 ns and the maximum delay is 4.8 μ s, enough to cover the Level 1 trigger latency of 4.1 μ s. The pipeline can store one hit per clock cycle, which means that there is no practical limit to the maximum number of wire hits recorded during one drift time interval.

The time of arrival difference between each end of the WAMUS tube pairs is used to break the ambiguities of the repetitive pad pattern. For a least count time ΔT , the resolution is $\sim c \cdot \Delta T / 5$. Therefore, to resolve the pads (pattern repeat length = 61 cm) with a resolution of 30 cm, a least count resolution of ~ 5 ns is required. We propose to calculate ΔT by subtracting time values from adjacent tubes.

The drift times themselves determine the muon momentum. On a test chamber using cosmic rays, we have achieved 0.4 mm resolution [26]. For WAMUS, even with a fast gas ($V_d^{-1} = 16$ ns/mm), this implies a time resolution of 6.4 ns or a least count of 22 ns. The time difference requirement drives the specification and the TMC resolution makes a small contribution to the drift distance measurement error. This resolution is also well matched to the time resolution of the FMSC counters, which also use the TMC chip for time digitization. In the 48,000 channel FAMUS MDT system, each input channel will have a latch similar to the scintillator counter card design and a digital delay based on commercial 18 bit FIFO instead of the TMC chip. Time digitization is performed using FPGA logic and gives a least count of 18.8 ns. As with other components of the muon system, the MDT electronics is designed for

deadtimeless operation.

C. Charge Integration

A new charge amplifier will be used to sample the pad signals for 350–400 ns. It will also feature a reset switch to eliminate saturation problems and reduced input impedance in order to collect the pad charge as rapidly as possible. The new pad integrator has a wide-band RMS noise of 1.2 mV and gain of 300 mV/pC. The recovery time of the integrator is about 20 ns which allows us to use a reset pulse 50 ns wide.

The pulse height ratio in the pads yields the coordinate orthogonal to the drift direction. For the pad repeat pattern of 61 cm, we achieved a resolution of ~ 2 mm on a test chamber [26]. In order to achieve that resolution we need to make 1% measurements of the individual pad pulse heights. This performance can be achieved with low cost 10-bit 15-Msps ADCs. The pad amplifier/integrator and digitization circuits will be implemented on the WAMUS A-layer PDT's. In addition these circuits will be used on some small number of channels on B- and C-layer PDT's for monitoring purposes.

2.8 Trigger Systems

2.8.1 Introduction

The Run I DØ triggering system includes two hardware triggers Level 0 (L0) and Level 1 (L1) and a Level 3 (L3) software trigger. Interactions with coincident hits in the small angle counters on both sides of the interaction region give a L0 trigger. After a L0 accept, the L1 trigger requires either a minimum E_T deposition in the calorimeter or primitive tracks of minimum p_T in the muon chambers. Four electron thresholds, four jet thresholds, and several global calorimeter sums are available at L1. The L1 requirements can be combined into 32 separate triggers and prescaled, if necessary, by an integral number to limit event rates. Once an event passes the L1 trigger, the entire detector is read out and the event assembled in a farm of VAX computers. This farm, the L3 trigger, performs a nearly complete reconstruction of the event. If the event includes objects of sufficient interest, it is written to tape. Event selection can occur in 128 L3 filters which can also be prescaled. Between L1 and L3, a third hardware trigger (L2) refines the calorimeter-based trigger for electron candidates by examining the shape of the energy deposition and refines the muon trigger by using finer granularity hardware information. L2 presently interrogates only a subset of the L1 accepts and inhibits data taking while examining the event. Typically, this limits the current L1/L2 accept rate to 150 Hz. The maximum L3 accept rate is 4 Hz.

A typical Run I trigger menu includes high p_T jet, electron, muon and large missing E_T triggers. The L1/L2 and L3 cross-sections, at a luminosity of $2 \times 10^{32} \text{ cm}^{-2}\text{s}^{-1}$, are 10 and $0.05 \mu\text{barns}$, respectively. These correspond to trigger rates of 2000 Hz for L1/L2 and 10 Hz for L3 at $2 \times 10^{32} \text{ cm}^{-2}\text{s}^{-1}$, which are beyond our present capabilities.

In order to deal with these high rates, the DØ triggering system requires significant enhancement. The upgrade must include a new trigger framework to deal with the increased rates. The trigger also includes several new detectors: the fiber tracker (CFT), the central preshower (CPS), the forward preshower (FPS), and muon detectors. The L2 system will be strengthened with more hardware engines to test for correlations between the L1 triggers. Pre-processors which reorganize the detector and L1 trigger information and a global processor will contribute to the L2 trigger decision. The L3 system will also require bandwidth and processor improvements to meet the increased computational needs of Run II.

2.8.2 The Trigger Framework

The L0 provides an inelastic collision trigger and luminosity measurement. The introduction of the solenoidal magnetic field dictates that the present L0 system be replaced because of its conventional phototube readout. The luminosity monitor functions will be replaced by the new L0 system.

There are two distinguishing characteristics of the new framework. First, all events will be examined by L2 hardware processors – not just a subset of events. Second, there will be event buffers between L1 and L2 and between L2 and L3. The addition of eight buffers between

each trigger stage de-randomizes the Poisson distributed arrival times of the events, decreasing deadtime due to pileup. The buffers also eliminate the present L1 disable during L2 operation. These two improvements alone increase the L1 accept rate to 5–10 kHz and the L2 accept rate to 1000 Hz. Since the Run II event sizes will be half that of Run I, an 1000 Hz event transfer rate to L3 and a 20 Hz rate to tape are feasible. To recapitulate, the expected Run II trigger accept rate limits are 5–10 kHz, 1000 Hz, and 10–20 Hz at L1, L2, and L3, respectively.

2.8.3 Level 1

The upgraded L1 trigger is composed of the calorimeter, the central fiber and preshower detectors, the forward preshower, and the muon scintillators and chambers. The calorimeter, fiber tracker, and preshower detectors will provide electron triggering for $|\eta| < 2.5$. The fiber tracker and muon systems will cover the region $|\eta| < 2.0$. All L1 triggers will be pipelined and buffered to ensure deadtimeless operation. In addition, the number of triggers will increase to 128 and fractional prescales may be available.

A. Calorimeter

The L1 calorimeter trigger will be unchanged from Run I. Both local energy deposition and global calorimetric characteristics can generate a trigger. The calorimeter is segmented into trigger tiles of $\Delta\eta \times \Delta\phi = 0.8 \times 1.6$ and trigger towers of $\Delta\eta \times \Delta\phi = 0.2 \times 0.2$ covering $|\eta| < 4$. A calorimeter trigger will require transverse energy above a preset threshold in one or more calorimeter trigger elements. For instance, a 200 GeV jet trigger may require one trigger tile with more than 50 GeV transverse energy. Additional trigger terms are provided by global quantities or trigger tower sums such a total transverse energy, total energy, and missing transverse energy.

B. Central Fiber Trigger and Preshower Detectors

The trigger scheme for the fiber tracker ($|\eta| < 1.6$) is based upon the $r - \phi$ hit patterns in 4.5 degree sectors and allows four distinct momentum thresholds. The outputs from the CFT trigger pickoff chips are fed into a series of large field programmable gate arrays. The gate arrays are preloaded with the appropriate logic to form eight-fold coincidences from hits in the eight CFT superlayers. A trigger will be generated by hit patterns consistent with track momentum above a software settable threshold. The trigger data is combined with the preshower detector on the trigger board and sent serially at 424 MHz to other trigger systems. There is a limit of six trigger candidates per sector. Each trigger candidate will be identified by momentum, charge, azimuth in the last axial layer, and the presence of preshower energy deposition above threshold. Central electron triggering will be limited by the preshower acceptance to $|\eta| < 1.2$.

The forward preshower detector will contribute to electron triggering in the region $1.4 < |\eta| < 2.5$. The L1 trigger will require a spatial match of preshower hits in each layer behind the converter lead with corresponding track stubs in each layer before the lead. Matching a track stub two strips wide before the lead with a single strip above a 14 MeV threshold after the lead defines a triggering algorithm with 90% efficiency approximately independent of position

for electrons with transverse momentum of 20 GeV. An energetic electron typically deposits substantial energy in seven or less adjacent strips. The L1 FPS electron trigger may also include isolated energy deposition behind the converter. Isolation would be indicated if the total energy in the three strips on either side of the seven is less than a specified threshold.

C. Muon

The central L1 muon trigger detectors include the barrel scintillation counters, the cosmic ray veto scintillation counters, and the proportional drift tubes. The forward L1 muon region includes the pixel scintillation counters and the mini-drift tubes. The CFT is also an integral component of the L1 triggering scheme for both the central and forward regions. The muon trigger acceptance includes the region $|\eta| < 2$. The muon trigger hardware resides on the detector platform. Central fiber trigger tracks, scintillation counter hits, and wire chamber centroids are sent to the hardware via high speed serial links.

The central L1 trigger computations are performed by detector octants in MTC05 and MTC10 VME cards. (MTC05 and MTC10 triggers are independent as the MTC05 cards operate only on azimuthal information and the MTC10 cards on chamber hits in the $r - z$ plane only.) The MTC05 trigger algorithm matches CFT trigger tracks with barrel scintillation counters for low p_T tracks. High p_T tracks also require cosmic ray veto scintillation counters since the tracks penetrate the CF toroid iron. The barrel scintillation counter segmentation azimuthally matches the central fiber tracker trigger sectors ($\Delta\phi = 4.5$ degrees) and, in addition, has nine segments along the z direction. A 25 ns timing gate used to define barrel scintillation counter hits serves to reject background hits. A 50 ns timing gate defines cosmic ray veto scintillation counter hits. Up to four different muon p_T thresholds can be defined using the track information from the CFT.

The MTC10 trigger algorithm uses centroids found in the proportional drift tubes verified by an accompanying barrel or cosmic ray veto scintillation counter hit. The confirmation is necessary because the proportional tube drift time (600 ns) is greater than the bunch crossing time (132 or 396 ns) and thus centroids can originate from several crossings. A low p_T trigger is defined using only A layer centroids. A high p_T trigger is defined using correlations between proportional drift tube centroids in two or three layers.

Triggering in the end regions is also done locally by octant in MTC05 and MTC10 VME cards. The forward MTC05 trigger algorithm matches CFT trigger tracks with A layer pixel scintillation counters for low p_T tracks and with A, B, and C layer pixel scintillation counters for high p_T tracks. The pixel scintillation segmentation azimuthally matches the central fiber tracker and has radial segmentation of $\Delta\eta = 0.1$. This segmentation ensures efficient triggering for muons of p_T greater than 3 GeV since a typical multiple scattering angle is about 3 degrees. A 25 ns timing gate defines pixel scintillation counter hits at the trigger level and serves to reject background. As with the central region, four different p_T thresholds can be defined using the track information from the CFT.

The forward MTC10 trigger algorithm uses centroids found in the mini-drift tubes which have been verified by an accompanying pixel scintillation counter hit. Although the drift time of the mini-drift tubes (80 ns) is less than the bunch crossing time, this confirmation is useful

for rejecting centroids from background particles produced at points other than the interaction region. Similar to the central MTC10 trigger, a low p_T trigger is defined using only A layer centroids while a high p_T trigger requires correlations between centroids in three layers.

A muon trigger crate manager (MTCM) in each crate of MTC05 and MTC10 cards collects the octant trigger information from each card and produces trigger information for each of the central, north, or south regions. This crate trigger information is then sent to the muon trigger manager (MTM) which produces global muon trigger information. The global muon trigger decision is subsequently sent to the trigger framework where it is included in the global physics trigger decision.

2.8.4 Level 2

The enhanced L2 trigger system [12] extends the power of the trigger systems to meet the increased event rates and shorter bunch crossing times of Run II. The upgrade L1 systems described above operate in a few μs upon the trigger signals from single detector systems – calorimeter, fiber tracking/central preshower, forward preshower and muon chamber/pixel detectors. The L2 system described here makes decisions on the scale of a hundred μs , dictated by the L2 input event bandwidth of $\sim 10\text{kHz}$. The deadtime introduced by the L2 system should be less than a few percent, while providing a factor of 10 rejection. There will be 128 L2 triggers available.

The L2 system described here obtains its rejection power by considering the correlations of trigger information from different detectors. We expect the specific correlation algorithms to evolve as experience is gained and new physics is added to the menu. The generic algorithms are those of matching spatial information of the same object in different detectors, and in computing correlations (mass, etc.) for multiple objects. Specific examples envisioned include: calorimeter – tracker matches, preshower – calorimeter matches, determination of jet parameters with reasonable jet cone definitions, determination of E/p , and rough mass calculations for dileptons, di-jets, lepton-jet. We require the L2 trigger to have a high degree of flexibility for implementing new algorithms that are necessary to address new physics. During Run I this flexibility paid off in defining new triggers and was extremely useful in coping with the large range of instantaneous luminosities.

Our understanding of the rejection power afforded by the cross-detector algorithms operating in L2 has been developed through simulations and experience with Run I data. The understanding of the trigger system has been solidified with detailed timing simulations of the overall trigger system, which have led to the incorporation of L2 preprocessors which prepare lists of compacted information for transmission to the event processors. We have adopted the design principle that generic choices for preprocessor and global processor hardware and software should be made to avoid expensive one-of-a-kind design and fabrication.

The system will consist of a set of preprocessors, which are detector specific and prepare the information to be sent to global processors. The global processors each work on one event at a time. An overview of this system is shown in Fig. 14.

Level 2 Trigger Block Diagram

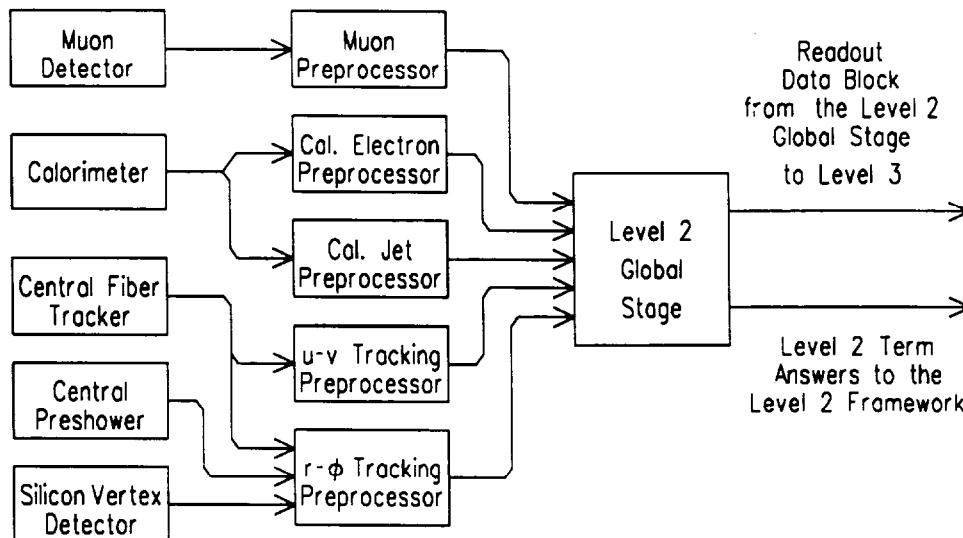


Figure 14: Overview of the L2 trigger components.

We choose not to work directly with the raw detector data but rather only with “concentrated” information from the detectors. This information is available from either the L1 Trigger system for a detector or else from the detector front-end through a special preprocessor. As shown in Fig. 14, each major detector system: muon, calorimeter, tracking, preshower and silicon vertex feeds data into a specific preprocessor. The result of each preprocessor is a list of candidate objects from that specific detector: muons, electrons, jets, tracks and secondary vertices. The number of preprocessors is limited and is determined by the number of detector systems. In addition, a design of the secondary vertices trigger exists and a L2 preprocessor of this trigger will be added later in Run II.

The L2 system must introduce a minimal amount of deadtime ($<1\%$). To verify this we have simulated the deadtime in the L2 trigger using a modeling package based on queuing theory. Simulations like this have provided guidelines for the processing time available in the preprocessor and global processor to complete an event. Typically this time is of order $30\text{--}40\ \mu\text{s}$ in the preprocessor and about $70\ \mu\text{s}$ in the global processor.

The requirements described above and the front end specifications of each detector system put rather different constraints on the preprocessor and so some variation is expected. However the global processor must be able to receive data from several sources and at a bandwidth of about $320\ \text{Mbytes/s}$. Given these constraints and the timing constraints described above, the hardware chosen consists of two classes: an ALPHA based RISC processor board and distributed DSP's. The DSP's are used as preprocessors and typically there are many of

them distributed in front end systems, for example in muon and tracking. The ALPHA based trigger processor board that we plan to use is being developed jointly by CDF and DØ. This development is a continuation of the ALPHA based trigger processor that CDF began using during collider Run I. The principal feature of this trigger processor design is its high speed input data path that can feed the same information to multiple processor boards from multiple data sources. This feature is what is missing from most commercial processor board designs.

2.8.5 Level 3

The DØ Level 3 trigger [27] for Run II is a straightforward upgrade of the existing data acquisition and high-level trigger system used successfully in Run I. This system has two fundamental features:

- (1) use of a farm of standard, high performance commercial processors to run event filter algorithms, written in high-level transportable code, with each filtering node handling complete events, and
- (2) data acquisition of each event's data from buffer memory modules in each of the digitizing crates directly to multi-ported memories in a specific filter node, over custom, high speed, parallel paths.

Besides providing an efficient platform which permits easy development and deployment of the software filters, this trigger system is easily upgradeable. For example, during the course of Run I, four generations of workstations were used successively as filter processors; and the software filter programs migrated smoothly through each generational change.

In Run II, the Level 3 will utilize the strength of the existing data path components and the associated processor farm framework. Thus the principle changes to the present system are:

- (a) replacement of the existing processors (VS-4000/90's) with the best price/performance systems available in '98-'99, and
- (b) further parallelization (and better utilization) of the data paths, together with the replacement of Futurebus hardware by Fiber Channel, for the 'long haul' links.

The principal development work needed to prepare the Level 3 Trigger for Run II is on modifications to the readout/control system. Although the complete upgrade of all processors is best delayed as long as possible, we will test some early versions of replacement processors as we upgrade the readout/control.

In Run I, data flowed on 8 parallel paths, from buffers in each digitizing crate to 8 external memory ports in each node; the aggregate capacity of the data paths was 388 MByte/s but typical occupancy was only around 20%. One of the limitations on the realizable readout bandwidth in Run I came from the latency of the external readout control system. For Run II we will replace the software-based readout decisions with an internalized control system such

that the data transport is highly data driven, and thus more efficient. Further, in Run I at any instant a single event flowed on the 8 parallel paths to all nodes (one of whose external memory ports were enabled). With the revised readout/control we can easily group the Level 3 processor nodes in separate segments so that multiple events can be flowing at the same time from the digitizing crates, with blocks for a given event still being collected in a single processor's memory. Although the initial specification for the Level 3 trigger calls for an input rate of 1 KHz, the planned readout/control system would permit staged upgrades to 10 KHz.

The Level 3 Trigger for Run II will be a natural upgrade to the existing data acquisition and high level trigger processor farm at DØ. Both the replacement of the processors and the upgrade of the readout/control system make use of the existing structure and components of the data paths. High performance commercial processors with the best price/performance will fit easily into this framework. The readout/control system adds additional parallelism in stages as increased performance is required. In this way the Level 3 Trigger will be well matched to the needs of DØ.

2.8.6 Trigger Examples and Rates

The L1 high transverse momentum electron trigger will be upgraded from a simple calorimeter threshold in E_T to include a CFT track and CPS deposition for $|\eta| < 1.2$ and a FPS trigger for $1.4 < |\eta| < 2.5$. The CFT momentum threshold gives good rejection against minimum bias (QCD) background. Requiring an energy deposition in the CPS spatially matched with the track further improves rejection against isolated charged pions. To reject forward pions, the FPS trigger will require a matched scintillator hit before the FPS converter to significant energy deposition after the converter. Since the calorimeter L1 trigger does not contain spatial information, it cannot be used to further improve the background rejection. The L1 high p_T electron trigger rate will be ~ 440 Hz at $2 \times 10^{32} \text{ cm}^{-2}\text{s}^{-1}$.

Both the forward and central L2 electron triggers will retain the present electron isolation and shape requirements. In addition, a rejection factor of approximately two should be possible by requiring a coincidence among the calorimeter, CFT, and CPS in the central region and between the calorimeter and the FPS in the forward region. With these new elements, the L2 electron trigger rate at $2 \times 10^{32} \text{ cm}^{-2}\text{s}^{-1}$ will be ~ 100 Hz for $E_T > 15$ GeV. A L3 electron rejection factor of 50 can be achieved by importing current off-line shape cuts into the software farm; the high momentum electron rate at $2 \times 10^{32} \text{ cm}^{-2}\text{s}^{-1}$ will be ~ 2 Hz for $E_T > 20$ GeV.

The L1 high p_T central muon triggers ($|\eta| < 1.6$) will also incorporate the CFT. Coincidences between the CFT, the muon scintillators, and the muon chambers themselves, will provide substantial background rejection. For instance, the $p_T > 7$ GeV L1 muon rate at $2 \times 10^{32} \text{ cm}^{-2}\text{s}^{-1}$ will be ~ 330 Hz. Use of the muon preprocessor at L2 to refine the centroids contributing to the L1 trigger will reduce the trigger rate to 160 Hz. At lower p_T (< 1.5 GeV), a pair of CFT⊕A-layer ϕ coincidences serving as a di-muon or J/ψ trigger will require 230 Hz at L1. A combined L2 di-muon centroid improved track and transverse mass trigger should provide an additional rejection factor of two and a L2 rate of 100 Hz. At L3, a rejection factor of ~ 50 will be achieved by requiring full tracking, cosmic ray rejection, and calorimeter confirmation.

2.8.7 Summary

Changes in the trigger framework and the addition of triggering elements will meet the high rate demands of Run II. Table 1 is a summary of the L1, L2 and L3 rates for various generic triggers at $2 \times 10^{32} \text{ cm}^{-2} \text{ s}^{-1}$. Typical electron and muon thresholds are 10–15 GeV. For completeness, high p_T jet, photon, and missing E_T triggers have been included. Note that there is sufficient remaining bandwidth for more specific low rate top, di-lepton and tri-lepton search triggers and for various (perhaps prescaled) lower p_T triggers. For example the central di-muon and di-electron trigger thresholds are 1.5 GeV and 6 GeV, respectively.

Trigger	L1 (Hz)	L2 (Hz)	L3 (Hz)
Capability	5–10k	1000	20
High p_T electrons ($e, 2e, e + \cancel{E}_T$)	440	100	2
High p_T muons ($\mu, 2\mu$)	330	160	3
Central Di-muon	230	100	3
Central Di-electron	400	25	2
$t\bar{t} \rightarrow e\mu$	60	15	1
High p_T jet	80	40	1
High p_T photon	30	10	1
High missing E_T	140	140	1
Total trigger rate	1710	590	14

Table 1: Approximate Run II trigger capabilities and accept rates for high p_T physics.

2.9 Luminosity Monitor

The DØ luminosity monitor in Run II consists of two hodoscopes of scintillation pixels mounted on the face of the end cryostats that cover the region $2.6 < |\eta| < 4.5$. The scintillation light will be read out using either wavelength-shifting fibers with photomultiplier tubes located in a low field region or fine-mesh photomultiplier tubes attached directly to the scintillator pixels. The primary purpose of these counters is to detect non-diffractive inelastic collisions with high efficiency for making an accurate determination of the DØ luminosity. An important secondary goal of the luminosity monitor is to provide diagnostic information regarding accelerator performance. Good time-of-flight resolution will allow the z coordinate of the primary interaction vertex to be measured for beam crossings with a single $p\bar{p}$ interaction. This allows beam-beam interactions to be separated from beam halo and provides a fast measurement of the luminous profile. During separated beam scans, the changes to the shape of the luminous profile are used to make a precise measurement of the beam optics. In addition, the luminosity monitor provides large η trigger coverage for hard diffractive and rapidity gap triggers and can be used to help identify beam crossings where there is only a single $p\bar{p}$ interaction.

2.10 Data Acquisition and Computing

The data acquisition architecture for DØ in Run II [28], as illustrated in Fig. 15, will be largely unchanged from the current system. The basic components will remain: VME Buffer Drivers (VBDs) in each front end electronics crate driving a high-speed Data Cable. The Data Cables will feed a new Data Collector / Data Distributor system, which further buffers the information and appropriately passes the data to a Level 3 processor node. The output from the Data Distributor is over the standard Data Cable, feeding Multi-Port Memories (MPMs) accessed by a farm of event-building and software-filtering Level 3 processor nodes. The processor node output is to another VBD – Data Cable system feeding event data to a Host Interface node. These nodes will pass the events via a standard network connection to data-logging and/or monitoring host cluster nodes.

The architecture has been designed with parallel and redundant paths. For example, the numbers of Data Collectors, Data Distributors, Level 3 processor nodes, Host Interface nodes, Host Logging nodes, and Host monitoring nodes can all be adjusted to match the desired event data bandwidths. The redundancy at any function level provides for a high degree of system reliability in case of single component failure.

The VBD – Data Cable – MPM path will handle a rate of 160 Mbytes per second (~ 800 Hz) to the Level 3 processor farm using existing components. The 48 Level 3 nodes will be replaced with ones running an open operating system, i.e. one which will provide the necessary real-time functions yet will allow great flexibility in choice of commercial hardware. An example Level 3 system in current terms might be a PCI-based PC running Windows NT. The processor farm must possess sufficient compute capacity to provide a software trigger rejection factor of approximately eighty by executing a substantial subset of the current offline algorithms.

The VBD – Data Cable – MPM path from Level 3 to the host system will be designed to accommodate a rate of 5 Mbytes per second (~ 20 Hz). The host system is also to be assembled from commercial components. Incoming event data will be written to local disk buffers for later spooling to local or remote serial media. The host system will also provide the platform for monitoring of the data stream and will act as the interface to the hardware monitoring and control system.

Events will be reconstructed on the FNAL processor farm system, with that portion dedicated to DØ (an estimated 20,000 MIPs) capable of matching the 10 – 20 Hz data acquisition rate. Following reconstruction, data will be stored on a tightly coupled disk and robotic tape system, and made available for analysis on a centralized analysis processor. We expect ~ 250 million events per year to be accumulated, requiring 3 Tb disk-resident and 160 Tb tape-resident storage.

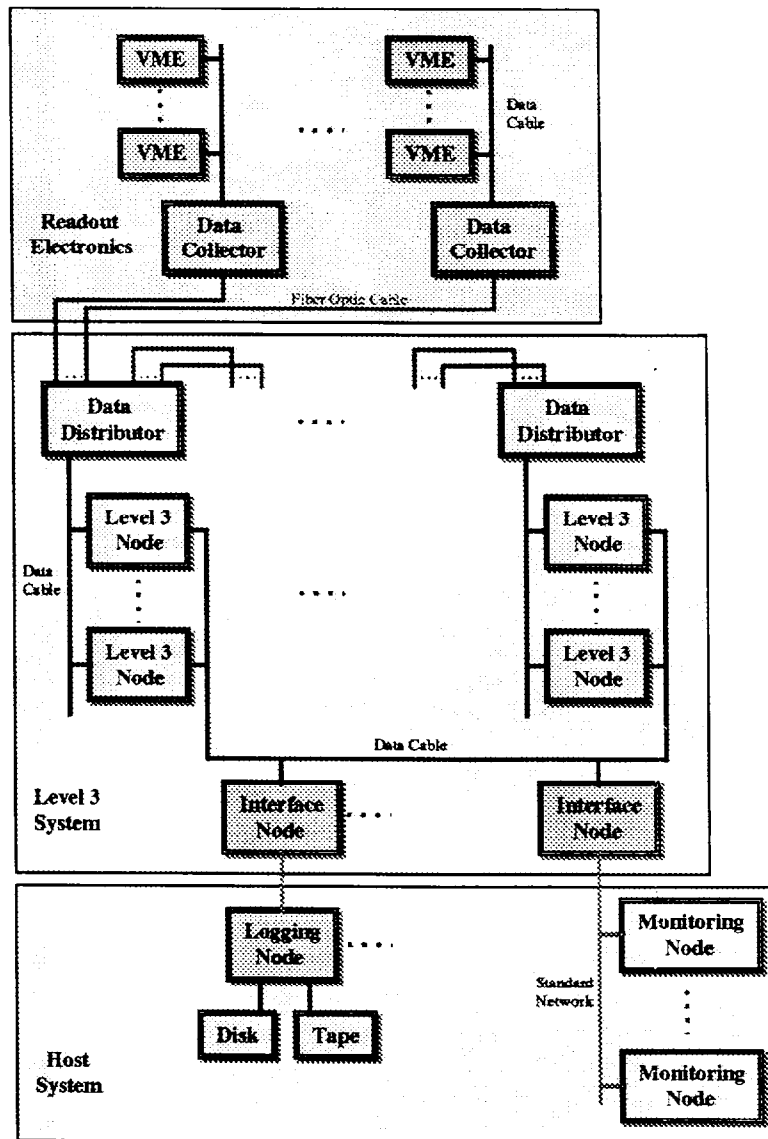


Figure 15: Upgrade Online computing architecture.

2.11 Software Upgrades

The computing requirements for the DØ upgrade are significantly more stringent than those for the Run I data collection and analysis. The software required for Run II data collection, reconstruction, and analysis is also not a simple extrapolation or maintenance project of the Run I software. Of the three major detector subsystems in Run I, one disappears and one is significantly revamped. The disappearing one is replaced by a system with very different software requirements (tracking in a magnetic field versus straight-line tracking). So, much of the DØ reconstruction system must be replaced. With the evolution of the detector into one with a central magnetic field, the basis for particle identification and detector calibration changes, implying that the analysis programs and calibration procedures also change significantly. The mix of computing platforms and operating systems will also be quite different in Run II. Therefore a major effort is underway to redesign the online and offline software to meet the new requirements and environment.

2.11.1 Software Organization

DØ has outlined a starting point for the Run II computing model in Ref. [29] in April 1995. At that point, four working groups were established to examine some of the software issues for Run II. In November 1995, DØ held a workshop at which the principal recommendations of the working groups were reviewed and adopted. In January 1996, an organizational structure was formed to implement the Run II software and computing. This structure, with four groups, is described below.

2.11.2 Online

This area includes the software for detector configuration and control, for the Level 3 trigger framework (not algorithms), for data logging, and for the monitoring and alarm system used during data-taking. A detailed list of tasks has been assembled, by analogy with the existing Run I online software [28]. People and institutions that will take responsibility for each of these tasks are being identified. The development of a schedule coordinating these tasks with the hardware schedule is also underway.

2.11.3 Algorithms

Within this group is responsibility for all software dealing directly with the physics of the DØ experiment. This group will generate the software for triggering algorithms in Level 3, reconstruction algorithms, calibration procedures for each subdetector, and particle identification algorithms. The organization within this area will be according to subdetector, with two additional subgroups (calibration and Monte Carlo) which cross subdetector lines. Work is already underway for tracking algorithms within the two new central trackers, the silicon and the scintillating fiber trackers. New clustering algorithms for the calorimeter are also being studied. Leaders have been appointed for the six subgroups.

2.11.4 Offline

The Offline group is responsible for software requiring more computer expertise than physics expertise. This group will be responsible for tools and/or systems for (1) information exchange, (2) editing, (3) code management and distribution, (4) compilers and debugger's, (5) databases, and (6) GUI building and editing. Investigation of choices for these systems is under way. The code management and distribution issue has been moved over to a joint working group including CDF and the Fermilab Computing Division for testing and further augmentation of the chosen system (CVS/UPD). It is hoped that success with this joint venture will be a model for further cooperation with CD and CDF to produce and maintain the necessary software tools for Run II. These tools are in many ways experiment-independent, and sharing the work in this area is an excellent way to conserve resources.

2.11.5 Production and Data Access

This group encompasses both the software and the hardware needed to (1) interface with the production farm and store the data and (2) retrieve the data in a timely fashion for analyses. Its immediate responsibilities are to define the data model, define the Run II platforms that replace D0FS/FNALD0, plan the purchase schedule for that replacement, and evaluate the hierarchical storage system which will be required in Run II. Later on, when Run II is underway, the responsibilities will include managing the production farms, moving the data from the farms to the analysis platform, and all associated bookkeeping and system management activities.

2.11.6 Summary

An organization is in place including appropriate groups to carry out the task of designing, writing, and testing software for Run II. Long term maintainability, operating system independence, and reliability are important auxiliary objectives in this effort.

3 Physics Topics and Detector Performance

3.1 Introduction

The Run I DØ detector proved to be an extremely powerful instrument for the study of the Standard Model (SM). Its finely segmented calorimeter and large angular coverage for electron and muon identification and measurement have enabled a wide range of physics studies to be addressed. Some of the physics results based on the Run I data set are summarized in Ref. [30]. A highlight was the announcement of the observation of the top quark by DØ in March 1995 [31]. The goals of the DØ upgrade are, firstly, to maintain this excellent performance in the future Main Injector era, when the Tevatron luminosity will be increased by a factor of 10 from Run I and the bunch spacing reduced from the present $3.6\,\mu\text{s}$ to $396\,\text{ns}$ (and eventually $132\,\text{ns}$); and secondly to significantly extend the capabilities of the detector. In particular we will:

- tag b -quark decays using displaced vertices in the silicon tracker;
- enhance muon identification and triggering, especially at low p_T ;
- enhance electron identification and triggering using the preshower and central tracking detectors;
- improve tau identification;
- determine the sign of the charged particles.

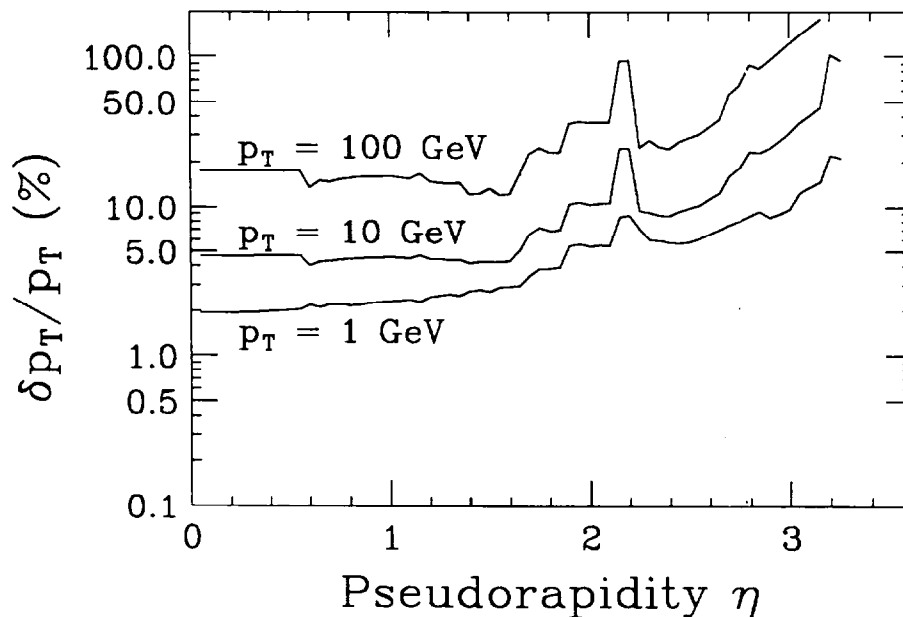


Figure 16: Charged particle momentum resolution *vs* η for various p_T 's.

The momentum measurement capabilities of the upgraded DØ detector are shown in Fig. 16.

In the following sections, we discuss some of the many physics topics which the upgraded detector will address. The program will be much richer than the outline given here, and we expect to further refine our analyses in the light of experience to achieve improved precision. The overall themes of the upgrade physics program are to seek the mechanism of electroweak symmetry breaking, through the study of large samples of the top quark and precision measurements of the parameters of the standard model; to make precision tests of the color force using a variety of probes and measurements in new regions of phase space; to carry out a broad programmatic study of b -quark hadrons; and to search for physics beyond the current paradigm.

3.2 Top Physics

3.2.1 Run I Observation of the Top Quark

In March 1995, the DØ collaboration announced the discovery of the long sought top quark [31], a critical ingredient of the Standard Model. The discovery analysis was based on data with integrated luminosities between 44 and 56 pb⁻¹, depending on the channel. The top quark signal was observed in both dilepton and single-lepton channels. The dilepton candidates possessed two isolated leptons, at least two jets, and large missing transverse energy \cancel{E}_T ; the single-lepton candidates had one isolated lepton, large \cancel{E}_T , and a minimum of three jets (with muon tag) or four jets (without tag). We imposed a minimum requirement in all channels on H_T , the scalar sum of the transverse energies E_T of the jets (for the single-lepton and $\mu\mu$ + jets channels) or the scalar sum of the E_T 's of the leading electron and the jets (for the $e\mu$ + jets and ee + jets channels). From all seven channels, we observed 17 events with an expected background of 3.8 ± 0.6 events. The probability of an upward fluctuation of the background to 17 or more events is 2×10^{-6} , which corresponds to 4.6 standard deviations for Gaussian probability distribution. We calculated the probability for our observed distribution of excess events among the seven channels and found that our results are consistent with top quark branching fractions at 53% CL. Thus, we observed a statistically significant excess of events and the distribution of events among the seven channels is consistent with the top quark production.

Since the discovery, the data sample has been doubled. The analysis has been refined to yield more precise measurements of the $t\bar{t}$ production cross section and the top quark mass. As reported at the 1996 International Conference on High Energy Physics in Warsaw, we observed 37 $t\bar{t}$ candidate events in the seven channels with estimated 13.4 ± 3.0 background events. For the dilepton channels, the main backgrounds arise from Z and continuum Drell-Yan production, vector boson pairs (WW, WZ), heavy flavor ($b\bar{b}$ and $c\bar{c}$) production, and backgrounds with jets misidentified as leptons. For the single-lepton channels, the main backgrounds are from W +jets, Z +jets, and multijet production with a jet misidentified as a lepton. Assuming a top quark mass of 170 GeV/c², the $t\bar{t}$ production cross section was measured to be 5.25 ± 1.79 pb. To determine the top quark mass, single-lepton + four-jet events were subjected to two-constraint (2C) kinematic fits to the hypothesis $t\bar{t} \rightarrow W^+W^-b\bar{b} \rightarrow \ell\nu q\bar{q}b\bar{b}$. A different set of the selection criteria was developed to select events for the mass analysis to reduce mass bias. A total of 93 lepton+jets events were selected. For every candidate event, a fitted top mass from a 2C fit and a top likelihood discriminant constructed using variables that are weakly correlated with top mass were determined. The best top mass was obtained by simultaneously fitting the fitted mass distribution and a top likelihood discriminant, incorporating top quark and background contributions. The estimated top mass was $169 \pm 8(\text{stat.})$ GeV/c². This result is consistent with all the fits tried by varying event sample, background and signal models. The total systematic error is estimated to be 8 GeV/c², dominated by the uncertainty of the jet energy scale. The measured $t\bar{t}$ production cross section for the measured top quark mass is shown in Fig. 17 together with the theoretical calculations.

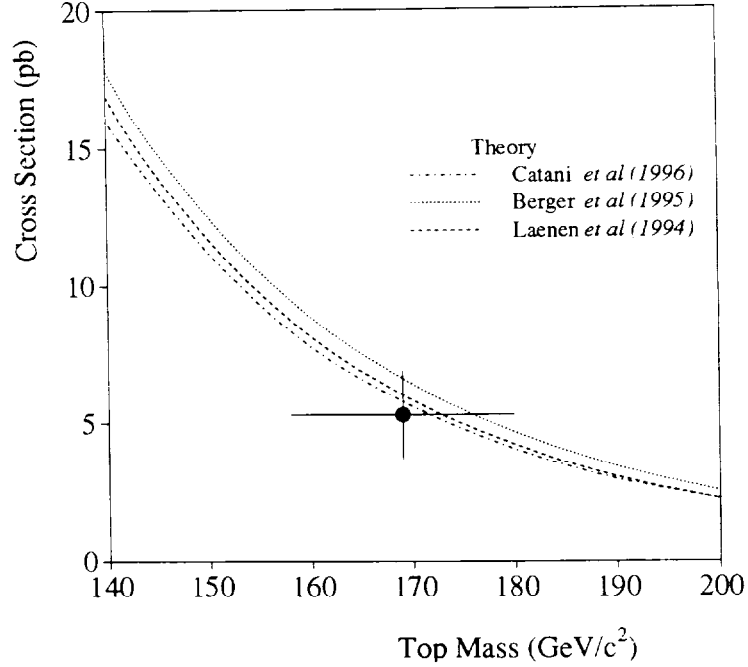


Figure 17: The measured $t\bar{t}$ production cross section for the $D\bar{D}$ top quark mass is compared with the theoretical calculations. The measurement is in good agreement with the calculations.

3.2.2 Run II Detector Improvements for Top Physics

A. Lepton p_T Resolution

All simulations described here for top physics include detailed ISAJET [32]/GEANT modeling of radiative effects and interactions in material, etc., and use full pattern recognition of tracks with raw hits as input. These simulations yield a p_T resolution for magnetic tracking of electrons from $t \rightarrow e$ ($t \rightarrow b \rightarrow e$) of $0.002p_T^2$ ($0.003p_T^2$). This is independent of, and in addition to, the $\sim 0.15\sqrt{E_T}$ resolution available from the central electromagnetic calorimeter. With the calorimeter continuing to provide the best energy information above $p_T \sim 20$ GeV/c, the main advantages of magnetic tracking for electrons lie in new capabilities for triggering and for electron identification using E/p , and in identification of the electron charge.

The benefits of magnetic tracking are dramatic for muons for which momentum resolution is slightly better than for electrons. In Run I the muon p_T resolution is bounded at low p_T by $\sim 0.2p_T$ due to Coulomb scattering in the steel filter. At high p_T it is limited to $\sim 0.003p_T^2$ by muon drift chamber resolution including alignment. With the addition of central magnetic tracking in Run II, the muon p_T resolution will improve by a factor of about two at high p_T . At lower p_T the muon resolution will improve even more, by a factor of approximately $100/p_T(\text{GeV}/c)$.

B. Lepton Tagging of b -jets From Top Decays

In Run II the new muon A-layer counters will permit muon identification and momentum reconstruction down to $p_T \sim 1.5 \text{ GeV}/c$. This will extend acceptance for soft muon b tags well below the present $\sim 4 \text{ GeV}/c$. Triggering on all top final states containing such tags (dilepton, lepton+jets, and all jets) will be enhanced by the new ability in Run II to trigger on muons above 6–10 GeV over most of the η acceptance of the calorimeter. This will become possible owing to the new dedicated muon trigger counters.

The new preshower detectors, combined with the E/p match afforded by magnetic tracking, will allow DØ in Run II to carry out b tagging in the electron channel as well. Monte Carlo studies indicate that electrons with $p_T \geq 4 \text{ GeV}/c$ from b -quark decays can be identified with high efficiency ($>50\%$) and low backgrounds by matching the preshower clusters with tracks in the magnetic tracker and requiring good E/p matches.

With these improvements, a probability of 40% for lepton tagging either b -jets from top decays should be achievable.

C. Secondary Vertex Tagging of b -jets From Top Decays

The top physics in Run II will benefit greatly from the silicon vertex detector. The detector will cover the full luminous region. The interspersed disk and barrel structure will allow us to reconstruct secondary vertices from b -quark decays in three dimensions within the range $|\eta| \leq 3.0$. The secondary vertex resolutions of $\sim 40 \mu\text{m}$ and $100 \mu\text{m}$ are expected in $r - \phi$ and $r - z$ planes respectively.

Based on some preliminary Monte Carlo studies (both $t\bar{t}$ signal and background events) and the Run I results from CDF, we estimate that the probability for tagging at least one b -jet in a $t\bar{t}$ event through the reconstruction of the secondary vertices should exceed 80% with low backgrounds in Run II. Moreover, both b -jets in a $t\bar{t}$ event can be tagged with about 50% efficiency. The high tagging efficiency will reduce the backgrounds in the $t\bar{t}$ sample significantly. Combined the soft lepton and the secondary vertex taggings, the probability for tagging a b -jet in a $t\bar{t}$ event should be above 90%.

Futhermore, the new trigger on the secondary vertices will enhance our $t\bar{t}$ trigger capability for all final states in general, the all-jet final state in particular.

D. Tau Identification

The jets from tau decays are generally isolated, narrow and pencil-like, characteristically different from those originating from quarks and gluons. Presently, the tau leptons from W decays in $t\bar{t}$ events are identified through their hadronic decays with about 14% efficiency and an acceptable background primarily by using the jet width information. The efficiency is expected to increase to about 20% by optimizing the selection algorithm. In Run II, the tau identification will be significantly improved using the information from the magnetic tracker. Monte Carlo studies show that the track-isolation is more effective in reducing QCD backgrounds than the calorimeter-isolation. A factor of two increase in the efficiency is anticipated.

3.2.3 $t\bar{t}$ Production Cross Section

Addition of the magnetic tracking will open up many new channels (secondary vertex tagged and soft electron tagged lepton+jets events, dilepton and lepton+jets events with taus) for DØ's top analysis, in addition to the dilepton (with e/μ), soft μ tagged lepton+jets, shape selected lepton+jets and all-jet modes used in Run I. Moreover, significant increases in efficiencies and dramatic reductions in backgrounds for the presently available channels are expected through the improved lepton identifications and momentum measurements of the charged particles. With the probability for tagging at least one b -jet approaching 100% per event, $t\bar{t} \rightarrow$ all-jets can be selected with high efficiency. This will allow us to use the high statistics of that sample.

The DØ preliminary $t\bar{t}$ production cross section from Run I is 5.25 ± 1.79 pb. The uncertainty on the current measurement is dominated by the statistics of the $t\bar{t}$ candidate sample. We expect the overall $t\bar{t}$ selection efficiency to double in Run II without any corresponding background increase. With an integrated luminosity of 2 fb^{-1} , the Run II $t\bar{t}$ sample represents a 40-fold increase compared with the current Run I data sample ($\sim 100 \text{ pb}^{-1}$). With this statistics, the systematic error dominates the error on the cross section. The major systematic sources are uncertainties on acceptance, background and luminosity. These systematic uncertainties are also expected to decrease with the increased statistics. Overall, we estimate that the $t\bar{t}$ cross section can be measured with about 10% accuracy for 2 fb^{-1} .

3.2.4 Top Quark Mass

A W mass precision approaching $\sim 35 \text{ MeV}/c^2$ may be achieved shortly after the end of the decade from the Tevatron and LEP II experiments. Our goal is to measure the top mass in DØ to a precision of $\leq 4 \text{ GeV}/c^2$, or $\leq 2.4\%$. The sensitivity of the Higgs mass to m_t and m_W is such that an error on the top mass much larger than this will dominate the uncertainty on m_H , while smaller errors on m_t do not significantly improve the precision with which m_H is constrained. Our $4 \text{ GeV}/c^2$ goal corresponds to a Higgs mass uncertainty of $\delta m_H/m_H \sim 0.8$.

From an integrated luminosity of $\sim 100 \text{ pb}^{-1}$ of Run I, we measured the top quark mass to be $169 \pm 8(\text{stat}) \pm 8(\text{syst}) \text{ GeV}/c^2$ from the constrained fit. To estimate the precision obtainable in Run II, one expects that the statistical uncertainty scales like $1/\sqrt{N}$ where N is the number of $t\bar{t}$ lepton+jets candidate events. A 40-fold increase in the statistics will lead to a 0.7% statistical error on the top quark mass. Clearly, then, the Run II top mass precision will be dominated by systematic errors. At present in DØ, foremost among those is the energy scale error of 4%. In Run II, we have several methods to reduce this uncertainty. The addition of the magnetic tracking will allow us to calibrate the jet energy scale *in situ*. As large statistics becomes available, $Z + 1$ jet events will replace the present $\gamma + 1$ jet events for the calibration using the jet balance technique. Moreover the jet energy scale can also be fixed using the dijet mass peak of the W 's from the top decays. Combining these methods, we expect to determine the jet energy scale with a precision of $\leq 1.5\%$.

Among the residual systematic errors, perhaps the least reducible is the difference between the actual pattern of gluon radiation and that predicted by the available parton shower Monte Carlo calculations. At present we observe $>2\%$ differences in the means of distributions of fit

mass for ISAJET [32] and HERWIG [33] top samples; the peaks of these distributions, to which fits can be especially sensitive, exhibit still larger shifts. The difference is expected to shrink with the implementation of the matrix element calculation at the next-to-leading order in the Monte Carlo event generators. Furthermore, the high statistics will impose strong constraints on the different models and even eliminate some models. Therefore, it is not unrealistic to expect a systematic error of about 1% on the top mass from the uncertainty in modelling $t\bar{t}$ events.

DØ possesses a unique advantage for controlling errors due to radiative corrections. This is its fine calorimeter granularity. We plan to use this detailed calorimeter information to *measure* the initial and final state radiation and to *recombine* the latter. Our techniques in this area are still in a formative stage. However, we are already able to demonstrate clustering algorithms able to detect, on average, >2 extra gluons per top event, and mass fitting algorithms able to identify and recombine these gluon jets. Relative to the conventional practice of fitting only the four leading jets, these algorithms improve the mass resolution and, more important, reduce the systematic uncertainties associated with these radiative corrections. Our detailed GEANT simulation of the calorimeter will also contribute to reducing these uncertainties, particularly as we gain more experience in benchmarking the simulations against real data.

To summarize, we believe that the top quark mass can be measured with an combined statistical and systematic error of $\leq 4 \text{ GeV}/c^2$ in Run II.

3.2.5 Top Quark Decay Properties

With approximately 1000 background-subtracted $t\bar{t}$ candidates, it will be possible to test the standard model predictions of the decay properties of the top and to search for rare top decays. The electronic and muonic branching ratios will be measured to 15% each, providing a key check on the Standard Model. The rate of double *vs.* single *b* lifetime tags should determine the $t \rightarrow b$ branching fraction to 5%, and thus the CKM matrix element V_{tb} to less than 3%. With the large top sample, the flavor changing neutral current decays of the top quark, such as $t \rightarrow c\gamma, cZ$, can be sought. The Standard Model predictions for the branching ratios of FCNC decays are around 10^{-10} , so any observation will signal new physics. The branching ratio limits of 3.0×10^{-3} for $t \rightarrow c\gamma$ and 1.5×10^{-2} for $t \rightarrow cZ$ should be reachable in Run II.

3.2.6 *W* Polarization from Top Decays

Since the top quark decays before it hadronizes, the *W* boson from the top decay therefore carries helicity information related to the Wtb coupling. In the Standard Model, the top quark decays to either left-handed (W_L) or longitudinal (W_0) polarized *W*'s. The ratio of the branching ratios of the top decaying to the left-handed and the longitudinal polarized *W*'s is predicted to be

$$\frac{B(t \rightarrow bW_0)}{B(t \rightarrow bW_L)} = \frac{1}{2} \left(\frac{m_t}{m_W} \right)^2$$

Therefore, the branching fraction $B(t \rightarrow bW_0)$ depends on m_W and m_t only and it is 69.2% for $m_t = 170 \text{ GeV}/c^2$. Non Standard Model couplings will appear as a departure of $B(t \rightarrow bW_0)$ from the prediction of the Standard Model. Precise measurement of the branching ratio $B(t \rightarrow bW_0)$ will provide an important test of the Standard Model.

The polarization state of the W can be analyzed through the helicity angle [35]:

$$\cos \theta^* \approx \frac{2m_{eb}^2}{m_{eb\nu}^2 - m_W^2} - 1$$

of the charged lepton from the W decay. Here θ^* is the angle between the lepton and the polarization axis measured in the W rest frame. The Standard Model $\cos \theta^*$ distribution for a top quark mass of $170 \text{ GeV}/c^2$ is shown in Fig. 18. The distributions of longitudinal and left-handed components are also shown. The branching ratio $B(t \rightarrow bW_0)$ can then be determined from a fit to the measured $\cos \theta^*$ distribution. With an integrated luminosity of 2 fb^{-1} , the branching ratio can be determined with a statistical precision of about 3%. The systematic uncertainty is expected to be similar to the statistical error.

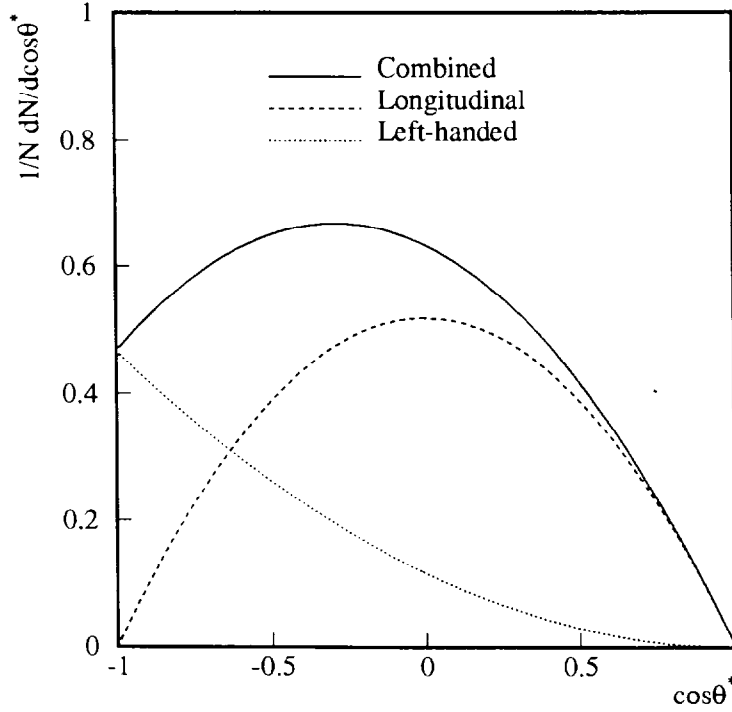


Figure 18: The $\cos \theta^*$ distribution for a top quark mass of $170 \text{ GeV}/c^2$ (solid curve) as predicted by the Standard Model. The distributions of the longitudinal and left-handed components of the W polarizations are shown in dashed and dotted curves respectively.

3.2.7 Single Top Production

A number of interesting physics measurements can be made by studying single top quarks produced via the electroweak interaction. The width of the top is not measurable in the $t\bar{t}$ state, but can be extracted directly (within theoretical uncertainties) from the single top cross section. Single top events will also provide an interesting cross-check of the top mass, since the multijet combinatoric problems are less severe. The expected dominant process for single top quark production in $p\bar{p}$ collisions is via W t -channel production, $qb \rightarrow q't$ with the b supplied by the antiproton sea, and $qg \rightarrow q't\bar{b}$, known as W -gluon fusion. For a $170 \text{ GeV}/c^2$ top quark at $\sqrt{s} = 2.0 \text{ TeV}$, the total single top cross section is 4.78 pb [36] (at leading order \times a K factor of 1.45), yielding 9560 events ($t + \bar{t}$) in 2 fb^{-1} . The t -channel process accounts for 63% of the cross section (3.00 pb , 6,000 events), with 28% coming from the s -channel W^* process (1.35 pb , 2700 events), and 9% from tW production (0.43 pb , 860 events).

The sensitivity of the upgraded DØ detector for single top physics has been studied using a fast parton-level Monte Carlo simulation [37]. We conservatively assume resolutions taken from Run I DØ data, a b -tagging efficiency of 50% per jet and a lepton reconstruction efficiency of 70%. We take as our single top signature two high E_T jets, at least one of which is tagged as a b jet (coming from the top decay), a high E_T electron or muon (from $t \rightarrow bW \rightarrow b\ell\nu$), and large missing E_T . After efficiencies and cuts, nearly 200 signal events are expected per fb^{-1} in a $100 \text{ GeV}/c^2$ band centered at the top mass. The dominant background processes are $p\bar{p} \rightarrow Wb\bar{b}$ and $p\bar{p} \rightarrow t\bar{t}$. The distribution of reconstructed top masses for signal and backgrounds, after cuts, is shown in Fig. 19 (with the leading order single top cross section used here). The signal to noise ratio in the peak region is roughly 1 to 2.2. We estimate that a 25% measurement of the cross section could be achieved with 2 fb^{-1} of data in Run II, which would give a 27% measurement of $\Gamma(t \rightarrow bW)$ and a 14% measurement of $|V_{tb}|$.

It has been pointed out by Stelzer and Willenbrock [38] that the s -channel process $q'\bar{q} \rightarrow W^* \rightarrow t\bar{b}$ is less prone to theoretical uncertainties than the t -channel process since initial state effects can be measured in the data from the similar Drell-Yan process $q'\bar{q} \rightarrow W^* \rightarrow l\bar{\nu}$. However, isolating the s -channel events requires more than 2 fb^{-1} and therefore is likely beyond the reach of Run II.

3.2.8 Search for the Charged Higgs Boson in Top Decays

The present limit on the mass of the charged Higgs boson predicted by minimal supersymmetry ($m_{H^\pm} > 45 \text{ GeV}/c^2$) is from LEP measurements. By the time the DØ Upgrade run is underway, we expect this limit to increase to $\gtrsim 90 \text{ GeV}/c^2$, the exact value depending on the maximum energy reached by LEP II. Assuming that the charged Higgs is lighter than the top quark, one can search for top quark decays into a charged Higgs and a b quark in addition to its usual decay into W and a b quark. The charged Higgs could have two predominant decay modes, $c\bar{s}$ and $\tau\nu$. Both top and H^\pm decay branching ratios depend on the $\tan\beta$ value of the minimal supersymmetric model. The Higgs decay will not contribute to the DØ dilepton top search channels of ee , $e\mu$ and $\mu\mu$ except by the secondary decay of the τ , which we neglect in the present calculation. The lepton + jets channels e +jets and μ +jets will have contributions from

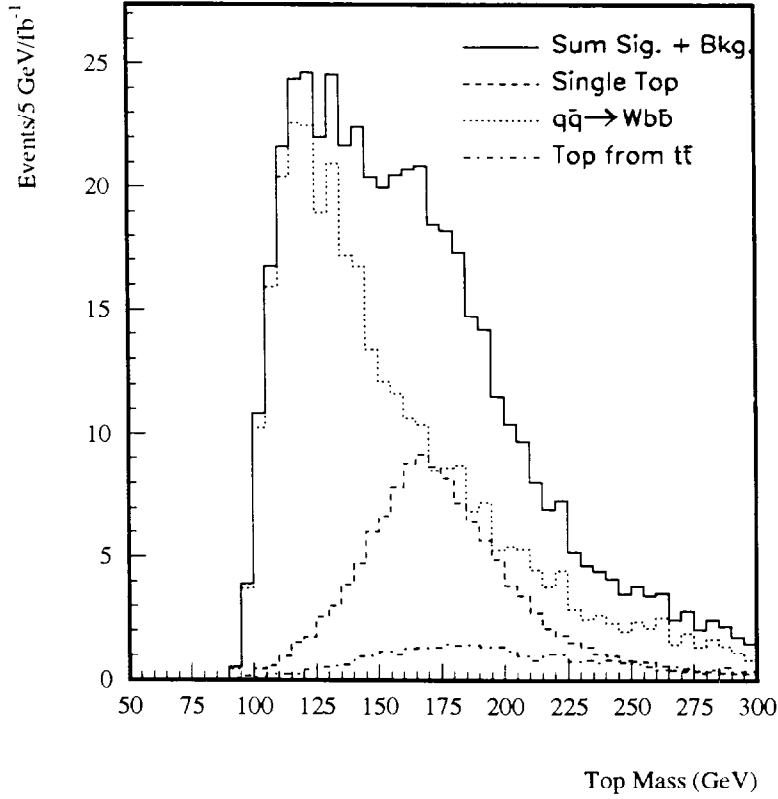


Figure 19: Distribution of reconstructed top mass for single top signal ($m_t = 170 \text{ GeV}/c^2$), $t\bar{t}$ and $Wb\bar{b}$ backgrounds, after cuts, for an integrated luminosity of 1 fb^{-1} .

both W decays and from charged Higgs decays.

There are several ways of searching for the charged Higgs in top quark decays.

- Searching for an apparent violation of lepton universality in top decays. An excess of τ decays compared with e and μ modes would signal the presence of a charged Higgs decay mode. The DØ upgrade, with its excellent tracking and finely segmented calorimetry is very well suited to precision τ studies.
- Counting the overall event rate and comparing it to the standard model QCD top production cross section. For an increase in the branching ratio $t \rightarrow H^\pm + b$ the total number observed events in e and μ channels falls. Comparing with the standard model top production cross sections enables a limit to be placed in the $m_{H^\pm} - \tan\beta$ plane.
- Since the charged Higgs contributes only to lepton + jets channels and not the dilepton channels, we can look for departures in the relative event rates in these two channels. This method does not assume the standard model QCD top quark production cross section.

- Look for effective mass peaks in the dijet system removed from the W peak. This method can in principle measure the mass of the charged Higgs, should it contribute significantly to top quark decays. However, as a search method, it is limited by the resolutions obtainable in the jet–jet effective mass.

3.2.9 Discovery of New Physics in the $t\bar{t}$ Channel

The top quark’s large mass makes it unique among the elementary fermions in having a coupling to the SM Higgs of order unity; it is the only fermion not to be approximately massless on the scale of electroweak symmetry breaking. It therefore offers a dramatic example of broken flavor symmetry and a window into possible physics beyond the standard model — for example, to scenarios where electroweak symmetry is dynamically broken at a scale of order the top quark mass. Examples of such phenomena are multiscale technicolor [39], color octet vector mesons V_8 associated with $t\bar{t}$ condensation [40], and electroweak isoscalar quarks t , [41]. The cross section, $t\bar{t}$ invariant mass, and centre-of-mass angular distributions may all be used to search for new physics.

The $t\bar{t}$ cross section is enhanced in most of these models. For example, in multiscale technicolor, a color–octet techni-eta η_T which occurs with mass 400–500 GeV/ c^2 can easily double the $t\bar{t}$ rate. If the $\eta_T \rightarrow t\bar{t}$ partial width is not too large, (e.g. the coupling $C_t \sim \frac{1}{3}$) then a peak at the η_T mass will easily be seen in the $t\bar{t}$ invariant mass distribution (with a width of about 20 GeV/ c^2) with 1 fb $^{-1}$ of integrated luminosity. If $C_t \sim 1$ then the $\eta_T \rightarrow t\bar{t}$ peak is much broader, and the mass peak is too wide for direct observation; the enhancement of the $t\bar{t}$ cross section will still be obvious.

Subsystem invariant masses may also be sensitive to new physics. For example, a color–octet techni-rho ρ_T may be produced and decay via $\rho_T \rightarrow W\pi_T^\pm$, with $\pi_T^\pm \rightarrow t\bar{b} \rightarrow Wb\bar{b}$, the same final state as in $t\bar{t}$ production. Searches for processes such as this will be possible with 1 fb $^{-1}$ of data.

Another sensitive observable is the centre-of-mass angle distribution of the top quarks. The Tevatron has a distinct advantage in this case, as the annihilating quark and antiquark directions are strongly correlated with those of the proton and antiproton. Measurements of forward–backward asymmetry (A_{FB}) are therefore much cleaner than at the LHC, where $t\bar{t}$ production is dominated by gg fusion. It is found [42] that 1 fb $^{-1}$ of data is sufficient to distinguish, at the 5σ (statistical) level, the A_{FB} arising from V_8 -enhanced top production from the standard QCD mechanisms.

3.3 Electroweak Physics

Because of its success in describing low energy phenomenology and its relative economy in the number of fundamental fields, the $SU(3)_c \times SU(2)_L \times U(1)$ theory of strong and electroweak interactions, based on the principle of non-abelian gauge invariance, has become the Standard Model. $SU(3)_c$ embodies the current theory of the strong interactions, Quantum Chromodynamics, and is deemed to be an unbroken symmetry of nature. The $SU(2)_L \times U(1)$ sector is the basis of the Standard Electroweak Model and is spontaneously broken at a mass scale $v = (\sqrt{2}G_\mu)^{-1/2} = 246$ GeV into $U(1)_Q$, the abelian gauge group of electromagnetism.

The Standard Model has been very successful phenomenologically. It has provided the theoretical framework for the description of a very rich phenomenology spanning a wide range of energies, from the atomic scale up to m_Z . It is being tested at the level of a few tenths of a percent, both at very low energies and at high energies. The aim of these studies is to test the theory at the level of its quantum corrections and to search for deviations that may signal the presence of “new physics”.

3.3.1 W Boson Mass

A prime measurement that is sensitive to quantum corrections is the precision measurement of the W mass, which provides a critical test of the Standard Model. The current preliminary DØ measurement of the W mass, based on central electrons only, presented at the 1996 Warsaw International Conference on High Energy Physics, is [45]:

$$\begin{aligned} m_W^e &= 80.37 \pm 0.06 \pm 0.12 \pm 0.07 \text{ GeV}/c^2 \\ &= 80.37 \pm 0.15 \text{ GeV}/c^2 \end{aligned}$$

where the errors are statistical, systematic and energy scale systematic, respectively. The current world average W mass, using the preliminary DØ [45] and the published UA2 [46] and CDF [47] values, is

$$m_W = (80.35 \pm 0.13) \text{ GeV}/c^2 \text{ (World Av., 1996)}$$

Table 2 [43, 44] lists the dominant uncertainties on the current DØ W mass measurement. With a better understanding of the high luminosity effects, the 70 MeV/ c^2 error from the modelling of these effects for Run Ib will be reduced to a negligible level. In addition, including the forward electrons in the analysis will shrink the error on m_W further. Furthermore, with large statistics of Run I, we are pursuing an alternative method for determining the W mass by comparing the transverse momentum spectra of electrons from W and Z decays. This method allows us to measure the mass ratio of the W and the Z and is free of many systematic uncertainties listed in the Table 2. Combining all the improvements, it is anticipated that the DØ error on the final Run I W mass measurement will be ≤ 100 MeV/ c^2 .

The error due to the uncertainties in the absolute energy scale, in the relative response of the hadronic to the electromagnetic calorimeter, in the resolution and the uncertainty in the

neutrino momentum scale are still dominated by the statistical error on the number of Z -events. It is therefore expected that the error on the W mass will approximately scale as $1/\sqrt{N}$ for integrated luminosities reaching 1 fb^{-1} . Some systematic errors are quasi-theoretical in nature and are associated with the details of the production process. With the large statistics, the W p_T spectrum, $d\sigma^W/dp_T$ will itself be measured. The structure function effects are controlled in part through the measurements of the W boson charge asymmetry and the forward-backward charge asymmetry in Z decays as discussed below. It is expected that with the upgraded DØ detector with two W mass measurements, one from the electron channel and one from the muon channel, a precision of $\leq 50 \text{ MeV}/c^2$ can be obtained with an integrated luminosity of 1 fb^{-1} .

	Run Ia	Run Ib	Common	Combined
m_T fit	80.35 GeV/c^2	80.38 GeV/c^2		80.37 GeV/c^2
W statistics	140 MeV/c^2	68 MeV/c^2		61.2 MeV/c^2
Z statistics	160 MeV/c^2	74 MeV/c^2		67.2 MeV/c^2
Calorimeter linearity			21 MeV/c^2	21 MeV/c^2
Electron resolution	69 MeV/c^2	20 MeV/c^2	10 MeV/c^2	21.3 MeV/c^2
CDC calibration	34 MeV/c^2		37 MeV/c^2	37 MeV/c^2
Recoil resolution	88 MeV/c^2	43 MeV/c^2		38.6 MeV/c^2
Recoil response	50 MeV/c^2	27 MeV/c^2		22.9 MeV/c^2
Lepton removal	35 MeV/c^2	28 MeV/c^2		21.9 MeV/c^2
Efficiencies	30 MeV/c^2	25 MeV/c^2		19.2 MeV/c^2
Backgrounds	35 MeV/c^2	14 MeV/c^2		13.0 MeV/c^2
W production/decay			71 MeV/c^2	71.0 MeV/c^2
High luminosity model		70 MeV/c^2		
Total uncertainty	255 MeV/c^2	140 MeV/c^2	83 MeV/c^2	124 MeV/c^2

Table 2: Systematic uncertainties on the DØ W mass measurement (preliminary). The uncorrelated components between Run Ia and Ib measurements are listed separately in column 2 and 3 while column 4 lists the correlated components.

The value of m_W and m_t can also be inferred from the precision electroweak measurements. The one σ $m_t - m_W$ contour from a Standard Model global fit to the measured electroweak parameters from e^+e^- -collisions is shown in Fig. 20 together with the current DØ measurements of m_W and m_t and the direct m_H limit from LEP. The mass m_H of the Higgs boson is unconstrained in the fit. The shaded bands correspond to lines of constant m_H , with the width of the bands being due mainly to the uncertainty in $\alpha(m_Z)$. It is clear that a precision measurement of m_W and m_t would constitute a significant test of the Standard Model. We illustrate this with a hypothetical Run II measurement with errors of $50 \text{ MeV}/c^2$ and $4 \text{ GeV}/c^2$ for m_W and m_t respectively.

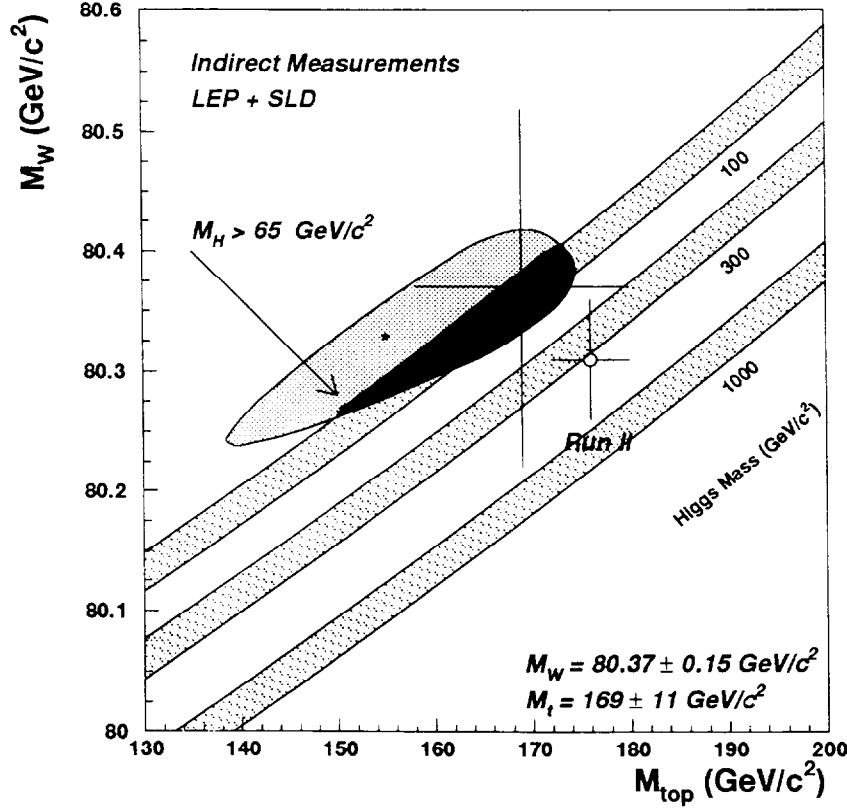


Figure 20: One σ $m_W - m_t$ contour from a global Standard Model fit to the LEP and SLD data together with the current DØ and a hypothetical Run II measurements of m_W and m_t . m_H is unconstrained in the fit. The cross-hatched bands are the Standard Model predictions for the indicated m_H . The widths of the bands are due primarily to the error in $\alpha(m_Z)$.

3.3.2 W Boson Decay Properties

The couplings of the W to other particles are additional parameters which are predicted by the Standard Model and which can be determined from the measured partial widths of the W to specific final states. Deviations from the Standard Model predictions could signal new decay modes or loop corrections involving new particles or new couplings. Both Γ_W and $B(W \rightarrow \ell\nu) = \Gamma(W \rightarrow \ell\nu)/\Gamma_W$ have been measured in hadron collider experiments.

An indirect measurement of $B(W \rightarrow \ell\nu)$ can be carried out by using the measured event ratio $R = \sigma B(W \rightarrow \ell\nu)/\sigma B(Z \rightarrow \ell^+\ell^-)$, multiplied by the theoretical production cross-section ratio $\sigma(p\bar{p} \rightarrow Z)/\sigma(p\bar{p} \rightarrow W)$ and the LEP measurement of the branching ratio $B(Z \rightarrow \ell^+\ell^-)$. The published world average [48] for the leptonic branching ratio is $B(W \rightarrow \ell\nu) = 0.107 \pm 0.005$, to be compared with the Standard Model expectation [49] of 0.1084 ± 0.0002 . In the future, the error in $B(W \rightarrow \ell\nu)$ is likely to be limited at about the 1% level by the theoretical uncertainty

in the production cross-section ratios.

The width of the W -boson can also be measured directly from the measured shape, and especially the high-mass tail, of the transverse mass distribution of $W \rightarrow e\nu$ events [50]. In the region far above m_W the effects of the largely gaussian resolution of the detector die off and the distribution is determined by the Breit-Wigner line shape of the W -decay. After 1 fb^{-1} of data, an error in Γ_W of about $50 \text{ MeV}/c^2$ is expected. This precision approaches the level of radiative corrections to the width.

Furthermore, the direct measurement of the W width may be combined with the leptonic branching ratio measurement to provide a measurement of $\Gamma(W \rightarrow \ell\nu)$. This leptonic partial width is predicted to be $\Gamma(W \rightarrow \ell\nu) = g^2 m_W / 48\pi$, and thus its measurement may be used to determine g . In conjunction with the measured leptonic branching ratio, this would give a measurement of $\Gamma(W \rightarrow \ell\nu)$ at the 1.8% level, and consequently an error on the W - $\ell\nu$ coupling g of 0.9%. The extraction of g from $\Gamma(W \rightarrow \ell\nu)$ is more reliable because it is not sensitive to QCD corrections that are present in the $\Gamma(W \rightarrow q\bar{q})$ widths.

3.3.3 The W Boson Charge Asymmetry

The W boson charge asymmetry

$$\mathcal{A}(\eta') = \frac{d\sigma(W^+)/d\eta' - d\sigma(W^-)/d\eta'}{d\sigma(W^+)/d\eta' + d\sigma(W^-)/d\eta'}$$

where η' is the lepton pseudorapidity, arises from the difference between u and d quark momentum distribution in the proton. The uncertainty of this difference is one of the major contributions to the error in the current W mass measurement. Therefore, a precise measurement of the W asymmetry will lead to a more precise measurement of the W mass by providing strong constraints on the parton distribution functions (PDF's). Moreover, the constraints will also benefit the $\sin^2 \theta_W$ measurement greatly as discussed in the next section.

With a large integrated luminosity, the W charge asymmetry is a very powerful tool in distinguishing different sets of PDF's. Figure 21 shows $|\mathcal{A}|$ as a function of the lepton pseudorapidity $|\eta'|$, predicted by two PDF's (CTEQ2M [51], MRSD- [52]). The lower plot shows the significance $\sqrt{\chi^2}$ with which the two can be distinguished as a function of the pseudorapidity coverage of the detector. In order to fully utilize the sensitivity of the W charge asymmetry to the PDF's, a lepton pseudorapidity coverage out to $|\eta'| = 2.0$ is essential.

The two parton distributions shown in Fig. 21 are already discriminated by the measurement performed by CDF [53] using data from Run Ia. The constraint on parton distributions from this measurement translates into an uncertainty in the W mass measurement of about $50 \text{ MeV}/c^2$. In Run II, we aim to measure the W mass to better than $50 \text{ MeV}/c^2$, which means that a much tighter constraint on proton structure is required. With the magnetic tracking and the large pseudorapidity coverage, the DØ upgrade is well suited for measuring the W charge asymmetry.

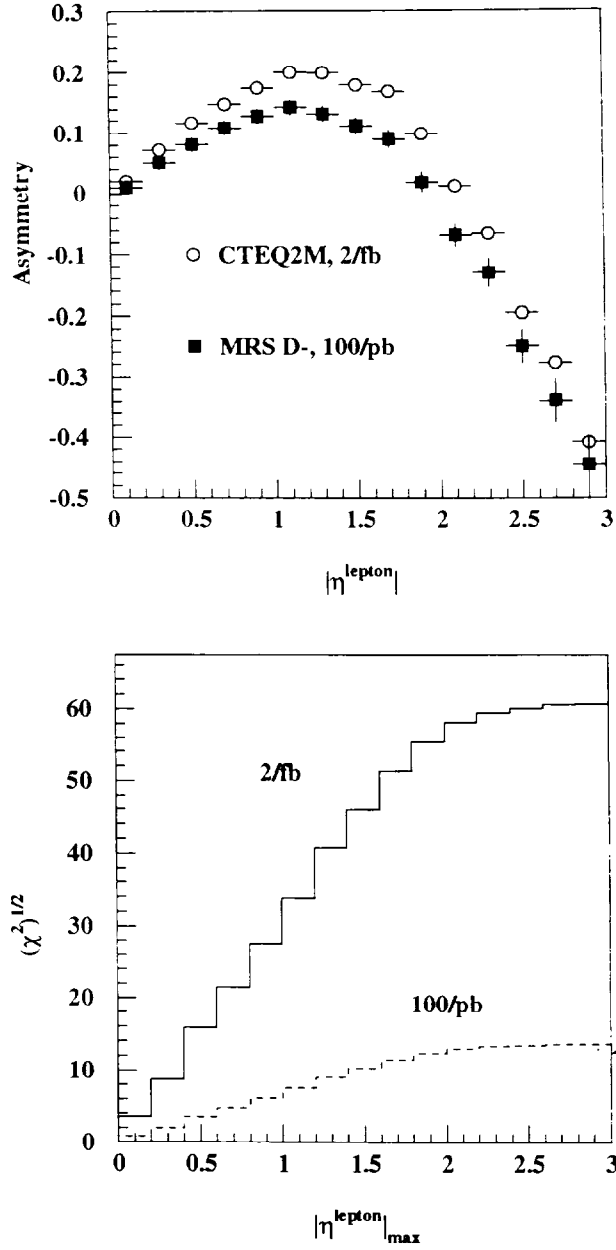


Figure 21: Top: lepton charge asymmetry predicted by CTEQ2M and MRSD-structure functions versus lepton pseudorapidity; bottom: significance with which the two curves can be distinguished for integrated luminosities of 2 and 100 pb^{-1} .

3.3.4 Forward-Backward Charge Asymmetry in Z Decays

The process $p\bar{p} \rightarrow \ell^+\ell^-$ exhibits a forward-backward charge asymmetry (A_{FB}) of the leptons, which arises from the parton level process $q\bar{q} \rightarrow \ell^+\ell^-$ and depends on the vector and axial vector couplings of the Z to quarks and leptons and is therefore sensitive to $\sin^2\theta_W$. The current combined error on $\sin^2\theta_W$ from asymmetry measurements at LEP and SLC is 0.00028 [54].

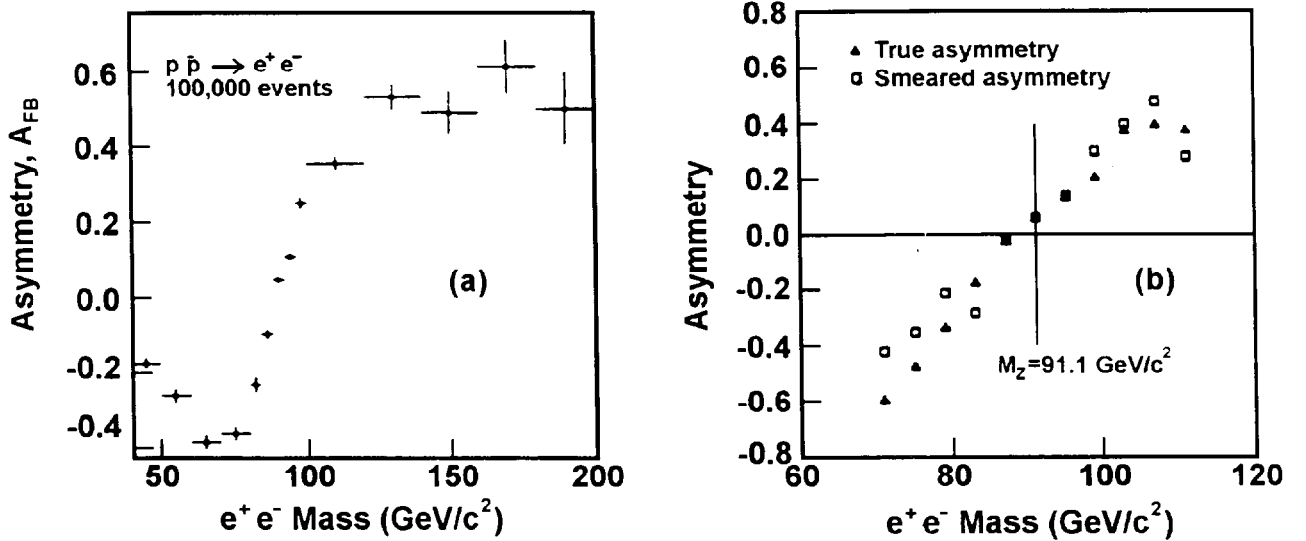


Figure 22: Forward-backward asymmetry A_{FB} as a function of e^+e^- invariant mass in $p\bar{p} \rightarrow e^+e^-$ events. (a) statistical errors for 1 fb^{-1} in an ideal detector; (b) effect of DØ calorimeter resolution.

Figure 22(a) shows the variation of A_{FB} with the e^+e^- invariant mass in $p\bar{p} \rightarrow e^+e^-$ events at $\sqrt{s} = 1.8 \text{ TeV}$. The error bars indicate the statistical errors for 100,000 events, corresponding to an integrated luminosity of about 2 fb^{-1} . From this simulation, we estimate the statistical error on $\sin^2\theta_W$ to be 0.001 for 1 fb^{-1} and 0.00035 for 10 fb^{-1} .

A preliminary study of the systematic errors indicates that most sources of error are small compared with the statistical error for a 1 fb^{-1} data set. The effect of the electromagnetic calorimeter energy resolution is rather small, as shown in Fig. 22(b). The main contribution to the systematic error is from the uncertainty in the parton distribution functions – since the vector and axial vector couplings of u and d quarks to the Z are different, the measured asymmetry depends on the ratio of u to d quarks in the proton. The measurement is primarily a test of our understanding of the couplings of the different quarks within the Standard Model. Alternatively, one may assume the SM couplings and use the world average value of $\sin^2\theta_W$ (with its smaller errors) to constrain the parton distributions of the proton at high Q^2 .

3.3.5 Anomalous Vector Boson Couplings

One of the most direct consequences of the $SU(2)_L \times U(1)_Y$ gauge symmetry is the specification of the couplings among the vector bosons: W , Z and photon. A direct measurement of these vector boson couplings is possible through the study of pair production processes $q\bar{q} \rightarrow W^+W^-$, $W\gamma$, $Z\gamma$, WZ , ZZ and triple boson productions. The first and major goal of such experiments will be a confirmation of the Standard Model predictions. A precise and direct measurement of the trilinear and quartic couplings of the electroweak vector bosons and the demonstration that they agree with the Standard Model would beautifully corroborate spontaneously broken, non-abelian gauge theories as the basic theoretical structure describing the fundamental interactions of nature. At the same time, such measurements may be used to probe for new physics. It is possible that signals for physics beyond the Standard Model will appear in this sector through the observation of anomalous trilinear (or quartic) gauge-boson vertices.

Because of the subtle cancellations between the different processes for di-boson production in the Standard Model, any deviation of the couplings from their standard model values will result in an increase in cross section. Furthermore, differential distributions will be significantly modified. For $W\gamma$ and $Z\gamma$ production, for example, the photon p_T spectrum exhibits a significant increase in the high p_T region. By comparing the shape of the measured and predicted p_T distribution limits on anomalous WWV and $Z\gamma V$ couplings can be obtained. Figure 23 shows the limits on the anomalous $WW\gamma$ and $ZZ\gamma$ -couplings derived from the Run Ia data.

The substantial increase in integrated luminosity expected for Run II will make it possible to test the WWV and $Z\gamma V$ vertices with much greater precision than in current experiments. The expected 95% CL limits on anomalous $WW\gamma$ and $ZZ\gamma$ couplings are shown in Fig. 24 from $W\gamma$ and $Z\gamma$ production at the Tevatron ($\sqrt{s} = 2$ TeV) for 1 fb^{-1} and 10 fb^{-1} . It can be seen that the current limits on anomalous gauge boson couplings can be improved by about a factor 5 – 15 (10 – 100) in $W\gamma$ ($Z\gamma$) production in the Main Injector era. An additional factor 10 in integrated luminosity leads to roughly a factor 2 improvement in the sensitivities. It should be noted that the limits quoted here are based on electron sample only. The limit contours shown can be improved by about 20 – 40% when $W \rightarrow \mu\nu$ and $Z \rightarrow \mu^+\mu^-$ decays are included in the analysis.

In addition to $W\gamma$ and $Z\gamma$ -production, W^+W^- , $W^\pm Z \rightarrow \ell\nu jj$ and $WZ \rightarrow \ell^+\ell^- jj$, $\ell = e, \mu$ production can be employed to study the non-standard WWV couplings. The sensitivity of these processes to anomalous couplings is similar to the sensitivity of $W\gamma$ and $Z\gamma$ production.

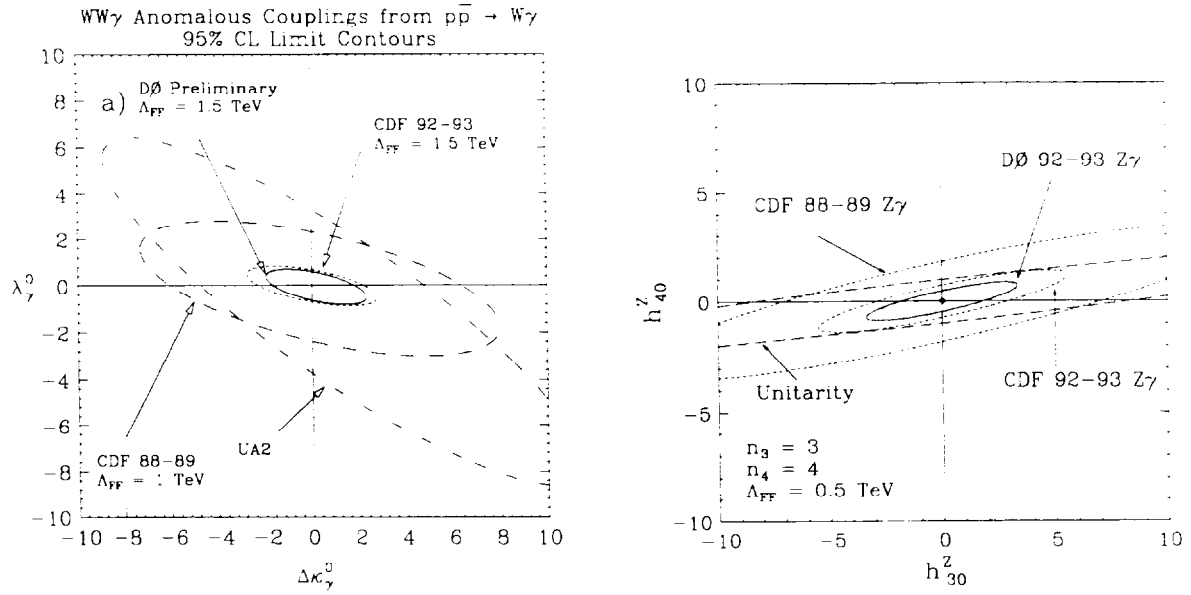


Figure 23: 95% CL limits on anomalous $WW\gamma$ and $ZZ\gamma$ -couplings derived from DØ Run Ia data.

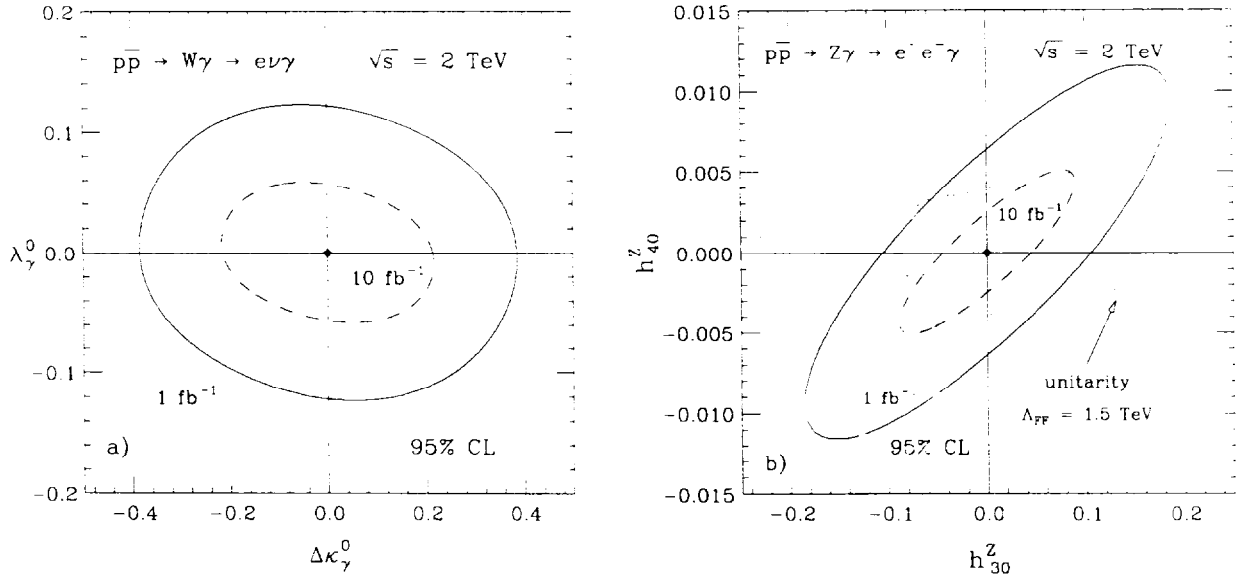


Figure 24: 95% CL limits on anomalous $WW\gamma$ and $ZZ\gamma$ -couplings obtainable with 1 fb^{-1} and 10 fb^{-1} .

3.4 QCD

3.4.1 Introduction

The data gathered at the Tevatron in Runs Ia and Ib have already resulted in many new and rigorous tests of QCD. Several years will be required to exploit fully the data taken with the current DØ detector at present luminosities. In particular, measuring differential cross-sections for jet, photon, and intermediate vector boson production with respect to increased numbers of event variables (momenta, pseudorapidities, etc.) will explore new regions of phase space particularly sensitive to parton distribution functions and higher order QCD calculations. These multi-dimensional cross-sections will also guide the way for establishing non-perturbative descriptions of partonic interactions, which are important at the edges of phase space. The large total luminosities expected for Run II will also encourage searches for new phenomena such as quark compositeness and excited quarks, rare diffractive processes, and vacuum polarization, and will provide accurate tests of all aspects of QCD because the theoretically and experimentally well described W/Z +jet samples will have statistical significance rivaling that of the present dijet samples. As QCD moves into this era of higher precision tests, confrontation between theory and experiment at higher integrated luminosities and with an upgraded detector will be of great importance. The addition of a central magnetic field will also allow the study of more exclusive final states such as W +charm and γ +charm. The current QCD program with the DØ detector is rich and imaginative and we are confident that this will continue with the upgraded detector. We have already presented analyses in areas of physics previously unexplored at the Tevatron: rapidity gaps, correlations between jets with large rapidity intervals, the measurement of α_s , and energy flow around the jets, as well as the development of new jet finding algorithms for the hadron colliders.

3.4.2 Parton Distributions

Until recently, cross-sections measured at the Tevatron have been used to verify the accuracy of current parton distribution parametrizations. This is one of the best tests of QCD because it requires the perturbative calculation of the QCD hard parton cross-sections *and* the QCD evolution equations to extrapolate the parton distributions from low energy fixed target experiments to the $p\bar{p}$ Collider energy scales. This is a rigorous test of factorization since the energy scales tested differ by more than an order of magnitude. Measurement of the total inclusive jet or photon cross-sections are examples of such tests.

Until now, however, the Tevatron results (except for the W -asymmetry measurement) have not been used to fix the parton distributions. This will change in the next few years as studies focus on measuring differential cross sections with respect to an increased number of variables for jets, γ 's, and W/Z final states with larger statistics. For example, consider the triple differential cross-section $d^3\sigma/dp_{T1}d\eta_1d\eta_2$ where p_{T1} and η_1 are the leading jet transverse momentum and rapidity, η_2 is the rapidity of the second leading jet [55]. At small leading momentum and rapidity, $p_{T1} = 50$ GeV and $\eta_1 = 0$, and large values of rapidity for the second jet, $\eta_2 = 2.5$, the cross-section is sensitive to the product of parton momentum fractions at extreme values of x (between 0.003 and 0.7). As a second example of differential cross-sections, the γ inclusive

cross-section $d^2\sigma/dp_T^\gamma d\eta$ and the γ + jet inclusive cross section at large rapidities are sensitive to the gluon content of the proton at $x = 0.001$. Also, the jet multiplicity distribution of the W +jets provides new information on parton distribution functions.

Looking ahead further one can anticipate the measurement of specific parton flavors in the proton, by selecting certain exclusive final states. This is very difficult with the current DØ detector, but is made possible by the upgraded tracking system. An example here is the final state W + charm, which directly probes the strange quark distribution. Another example would be γ + charm or any other process where the final state quark could be tagged. Charm identification will be possible both through reconstruction of the exclusive D decay modes, and through tagging soft muons from the charm decay.

3.4.3 Next-to-Leading Order and Beyond

The differential jet, γ , W and Z cross-sections just discussed also provide precise tests of QCD calculations at order α_s^3 (NLO). These calculations for differential jet and W +jets productions are now available [56, 57]. For large jet rapidities, leading order calculations seriously underestimate the cross section. NLO calculations compensate for this shortfall but not completely. Most likely even higher order calculations are necessary and these are currently being worked on. The examination of rare high p_T and very forward jets, possible only with high luminosity, will be a further revealing test of NLO and NNLO calculations. The large pseudorapidity coverage of the DØ calorimeter ($|\eta| \lesssim 4$) is ideally suited to these measurements.

Currently, precision studies of QCD with jets are limited in DØ because the jet energy scale has systematic errors in the 5–10% range. This error will be greatly reduced in the upgraded detector, because tracking in a magnetic field will allow a calibration of the hadron energy scale *in situ*.

At very low transverse momentum or at the edge of accessible phase space, one expects non-perturbative effects, like primordial parton k_T , to play a role. It has been suggested that such effects can explain the discrepancies in direct photon cross sections at different center of mass energies. A universal formulation of such non-perturbative phenomena is being attempted now [58], and its predictions can be tested in other processes at the Collider. To test the transition from perturbative to non-perturbative calculations, both large acceptance and high luminosities are required. The W and Z p_T spectra test a similar transition since the low p_T portion of the spectrum is calculated by resummation techniques, with the above mentioned non-perturbative contributions, and matched to the high p_T perturbative part of the spectrum.

NLO calculations for di-photon and intermediate vector boson production are available but have not been precisely tested [59, 60]. The high statistics samples required for these NLO tests must wait for higher luminosities or, equivalently, higher energies.

3.4.4 Drell–Yan (W/Z) Production

Drell–Yan pairs provide a clean probe of QCD processes. The colorless muons or electrons are free of final-state interactions and can be accurately identified without any of the ambiguities of jet identification and measurement. Typically, cross sections are small, and, as a result, Drell–Yan production has not been used to its full potential. However, the special cases of Z and W production have recently been used to test perturbative, resummed, or parton shower based predictions of QCD. Two examples include the determination of α_s from $W + \text{jets}$ and the comparison of Z and W p_T distributions with resummed predictions.

Z production alone can be considered an outstanding QCD test laboratory. Because the final state Z can be reconstructed very accurately and without background, the measurement of p_T , p_L , rapidity dependence, and energy flow around the Z can be made in an unambiguous and unique way. This kind of detailed study of QCD is just starting to become feasible with currently available luminosities. With higher luminosities, it can reach the statistical precision of jet cross sections but without any of the hindrance from systematics. To reach this statistical precision one would need a sample of roughly 10^5 Z 's, which corresponds to about 1 fb^{-1} if one uses the $Z \rightarrow e^+e^-$ and $Z \rightarrow \mu^+\mu^-$ decays. In fact, the entire menu of differential jet and photon cross-sections can be replaced with differential $Z + \text{jet}$ final state cross-sections. This will truly move QCD into the realm of precision physics. An obvious measurement here would be the determination of α_s from the ratio of $Z + n\text{jet}/Z + (n-1)\text{jet}$. This would be similar to what has already been done with W 's, but much more precisely determined experimentally.

The special case of Z production can be generalized by introducing the Drell–Yan ($\gamma^* \rightarrow \ell^+\ell^-$) pair mass as a parameter. In particular, measurement of the Drell–Yan pair p_T distribution as a function of mass provides a test of resummation techniques. The more interesting measurement though would again be the determination of the strong coupling constant. One employs the same technique as for Z 's, but as a function of the lepton pair invariant mass. This results in a measurement of α_s as a function of Q^2 scale, and tests both the running of α_s and its absolute value in one experiment. With sufficient statistics the angular distribution of the final state leptons may also analyze the polarization state of the vacuum [61], a possibility that has, as yet, not been investigated at the collider. Including both electron and muon final states, one expects about 60K events in the region $20 < m_{\gamma^*} < 30 \text{ GeV}$.

3.4.5 Jet Algorithms and Studies of Jet Structure

DØ has developed a new jet-finding algorithm based on the successive-combination techniques commonly used in e^+e^- physics. The same algorithm may be used to find clusters of energy within jets. With large statistics, we hope to be able to statistically separate quark and gluon jets using this approach and thus refine our study of the QCD subprocesses. It should also be possible to measure both α_s and observe its running from the dependence of the observed number of jets on the combination scale used in the algorithm.

3.4.6 Rapidity Gaps, Diffractive Scattering and the Pomeron

Dijet production at large rapidity differences, $\Delta\eta \gtrsim 4$, with little or no activity between the jets (rapidity gaps) signals the presence of the exchange of a colorless object [62]. Such events have been observed by DØ in its current run and we want to examine this phenomenon further in the future. Is the exchanged object the Pomeron and is it the same object observed in diffractive scattering? By studying diffractively produced events at the Tevatron the partonic content of the Pomeron may be measured. Is it the same as measured at HERA and at UA8? These questions can partially be answered with events with rapidity gap signatures, but ultimately may require the measurement of the diffractively scattered (anti-)proton. DØ has begun to investigate the potential for pursuing rapidity gap and diffractive physics in Run II.

3.5 B -Physics

3.5.1 Introduction

The upgraded DØ detector will address a variety of B physics topics, ranging from QCD tests involving production dynamics through the mass spectrum of the B_c system, rare decay modes, B_s mixing and CP violation. Apart from the last, the Tevatron is the only (or the pre-eminent) facility where these fundamental issues may be addressed. The DØ detector's full η coverage is particularly well matched to measurements of B -mesons — beauty is produced uniformly in pseudorapidity. Mesons produced centrally are typically soft, with $\gamma < 3$, putting a premium on soft lepton triggers and minimal multiple scattering. The low boost for centrally produced B 's implies decay fragments which are distributed in η . In addition much of the most interesting physics, such as B_s mixing and CP violation, requires that both partners in the $B\bar{B}$ pair be at least partially reconstructed. Physics which requires either full reconstruction of the final state or tagging of the partner B will be quite sensitive to the coverage of the tracking system. The strengths of the upgraded DØ detector for B -physics, then, are its full calorimetric and muon coverage, and its ability to trigger on low- p_T leptons over the pseudorapidity range $|\eta| \leq 2$ for muons and $|\eta| \leq 2.5$ for electrons.

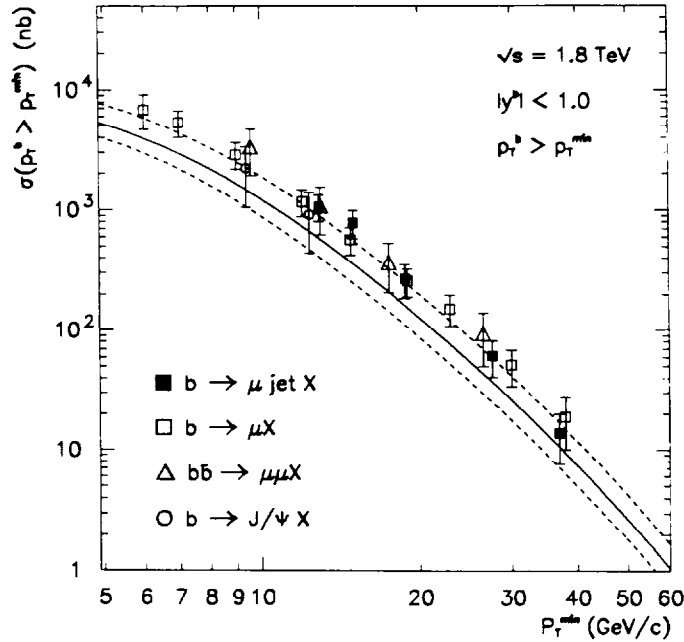


Figure 25: b -quark production cross sections for $|y^b| < 1$ from the inclusive muon, muon plus jets and J/ψ Run Ia data samples.

Although B mesons are produced copiously (about 2000 $B\bar{B}$ pairs per second at $\mathcal{L} = 10^{32} \text{ cm}^{-2}\text{s}^{-1}$) studies of B_s mixing and CP violation are still likely to be limited by statistics.

Final states must be fully reconstructed and the initial state must be tagged. CP violating decay modes are typically at the 10^{-5} level. We will need fully reconstructed decay chains with typical branching ratios of $\sim 10^{-4}$ to obtain sufficient resolution for B_s mixing measurements. The experimental challenge is to trigger on, collect, and reconstruct these events.

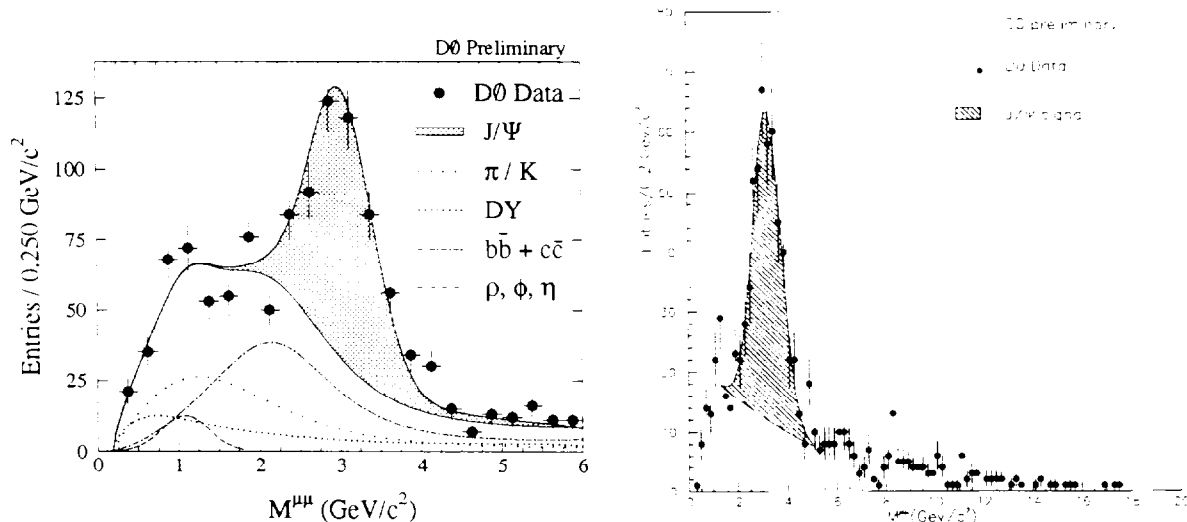


Figure 26: Inclusive $p\bar{p} \rightarrow \mu^+\mu^-$ cross sections as measured by DØ in Run Ia, for central (left plot) and forward (right plot) muon samples.

DØ has had an active B physics program in Run I with an emphasis on the detector's strengths in muon detection and calorimetry. DØ has measured b -quark production cross sections using different data samples as shown in Fig. 25. Current studies include measurements of inclusive muon and charmonium production (see Fig. 26) the heavy flavor content of jets, and $B\bar{B}$ oscillation. B production represents a small fraction ($1/1000$) of the total cross section. In Run I we have gained a great deal of understanding of how to successfully trigger and reconstruct b 's. The job is especially difficult in the intermediate to large η range. Our plans represent the results of studying the triggering and reconstruction problems over the full pseudorapidity range.

The upgrade represents a very significant improvement in DØ's B physics capabilities. Magnetic tracking allows us to reconstruct the masses of hadronic final states and tag the sign of electrons and hadrons. Our J/ψ mass resolution will improve by a factor of 10. The Level 1 track processor will improve the overall level of signal/noise by allowing sharp p_T thresholds for lepton triggers. Combined with the A-layer muon trigger counters, the processor will substantially lower the muon trigger p_T threshold, crucial for efficient b triggering. Signal/noise ratio will also be improved by matching muon system and central tracks at the trigger level. The forward muon pixel counters will allow muon triggering at intermediate η . The silicon vertex detector will allow us to tag decays based on lifetimes, to study B_s mixing, and reduce backgrounds for the whole range of heavy flavor physics. It is a crucial addition for B_s mixing

and CP violation studies. In addition the silicon disks provide forward tracking in the detector. DØ will be the first experiment to seriously explore heavy quark physics in the forward region.

However, our plans do not represent a complete B -physics program. To contain costs and meet the laboratory schedule, DØ has chosen not to upgrade the Level 1 bandwidth beyond 10 KHz. We have also chosen to postpone the Level 2 vertex processor. This will constrain some of our B physics reach in Run II and present some hard choices in our trigger lists.

As examples of Run II B -physics, we consider two benchmark processes, B_s mixing and CP violation. The results shown are from recent studies using a fast simulation package [64]. In previous studies we have demonstrated the very high reconstruction efficiency of the upgraded DØ tracking system.

3.5.2 B_s Mixing

A measurement of B_s mixing, along with the measured value for B_d mixing, will constrain the CKM matrix parameters ρ and η ($x_s/x_d \sim 1/((1-\rho)^2 + \eta^2)$). The large mass of the top quark suggests a value of x_s well in excess of ten; x_s can be measured by taking the difference of mixed and non-mixed events as a function of proper time: $N(B_s \rightarrow \bar{B}_s) = \frac{1}{2}N_0 e^{-t/\tau}(1 - \cos(x_s t/\tau))$, where N_0 is the number of B_s at $t = 0$ and τ is the B_s lifetime.

We have obtained a qualitative picture of the effects of reconstruction on the lifetime resolution:

- Partial reconstruction (*e.g.* semileptonic decays) of the final state can only provide momentum resolution in excess of $\sim 20\%$, which implies a reach of $x_s \lesssim 10$.
- In general, the statistical loss from full reconstruction of a state like $B_s \rightarrow D_s \pi$, $D_s \rightarrow \phi \pi$ is more than balanced by increased lifetime resolution for the final state. Our strategy, then, is to aim for fully reconstructed states.
- In the central region the lifetime resolution is dominated by the vertex resolution and is typically $\sim 5\%$.
- In the forward region the lifetime resolution is dominated by momentum resolution.
- The momentum resolution can be significantly improved by kinematic constraints on the intermediate states.
- Forward acceptance doubles the b tagging efficiency.

We expect that with 1 fb^{-1} of data, the upgraded detector should be able to measure over 2000 B_s decays with a lifetime resolution of better than 5%. This should allow us to measure values of $x_s \lesssim 25$. Figure 27 shows the difference in the number of mixed and unmixed B_s events as a function of proper time for the case $x_s = 12$. The B_s 's are reconstructed through the decay $B_s \rightarrow 3\pi D_s$ and the signs are tagged through the semi-leptonic decays of the other B 's. A fit to the distribution yields $x_s = 12.01 \pm 0.05$.

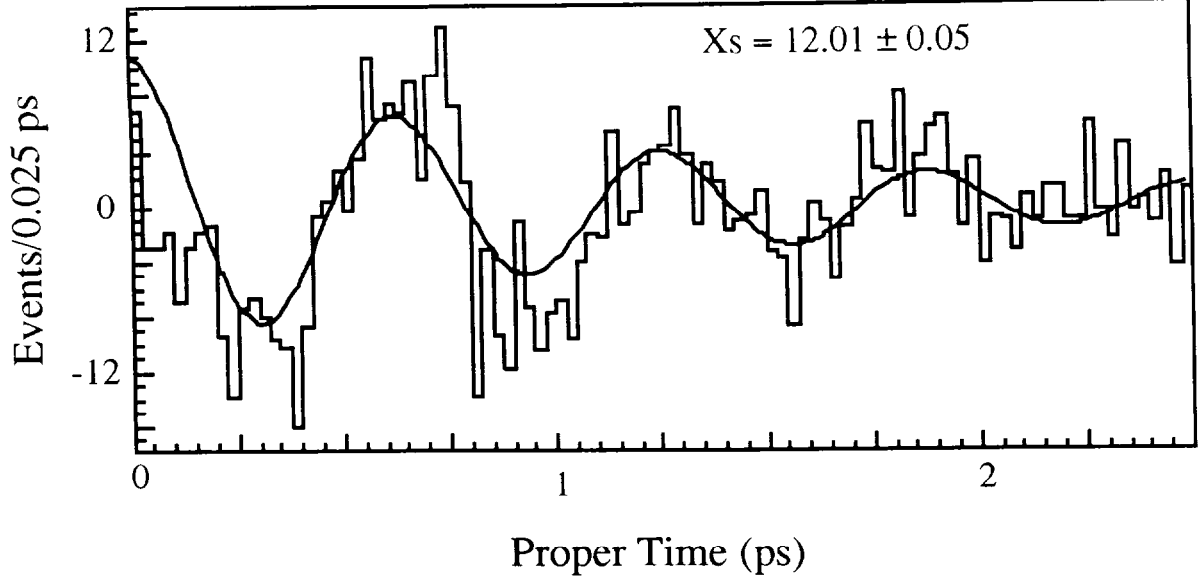


Figure 27: Difference in the number of the mixed and the unmixed B_s events reconstructed through $B_s \rightarrow 3\pi D_s$ as a function of proper time for the case $x_s = 12$ obtainable with 1 fb^{-1} data.

3.5.3 CP Violation

The study of CP violation in the B system is a standard benchmark process for b physics. The error in the CKM parameter β is $\delta(\sin 2\beta) = (1+b)/D(1-2w)\sqrt{N(1+b)}$, where the dilution factor, D , is defined as $D = x_d(1+x_d^2)$, N is the number of tagged events, w is the fraction of wrong sign tags and b is the background to signal ratio. Values of D and w have been extracted from a number of studies.

We have considered two scenarios:

- Central tracking and central lepton triggering/tagging;
- Central tracking but with lepton triggering/tagging over the range $|\eta| < 2.5$;

In accessing the resolution in $\sin(2\beta)$ the increased number of events reconstructed in the forward tracker must be balanced against the degraded mass resolution in the forward direction. Background levels are obtained by scaling from CDF's B results. Expected $D\bar{O}$ muon acceptances and efficiencies were used [63] together with mass resolutions and reconstruction efficiencies for the upgraded tracking system given by the fast simulation package. Table 3 shows the results for our combined simulations of the upgraded detector. Figure 28 shows the expected J/ψ mass resolution for $B \rightarrow J/\psi K_S^0$ from the MCFAST [64] simulation. We note that the mass resolution for the reconstructed B 's is sufficient to eliminate the $B \rightarrow \psi K^*$ background.

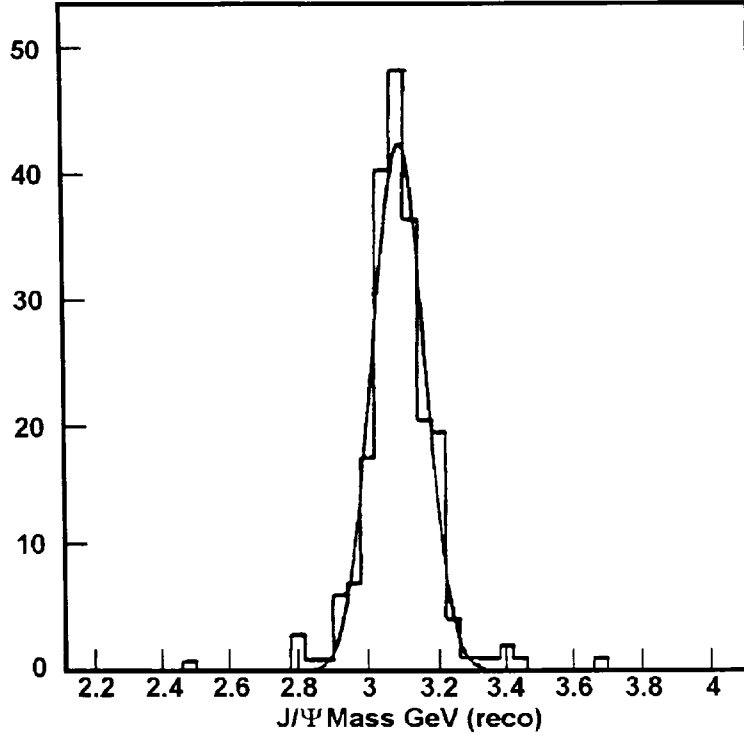


Figure 28: The expected J/ψ mass resolution in Run II reconstructed from the $J/\psi \rightarrow \mu^+\mu^-$ decays.

$B \rightarrow \psi K_S^0$	Central only	Central+full tag
Events in final state	430,000	430,000
Trigger	multi- ℓ	multi- ℓ
Efficiency \times Acceptance	0.0006	0.0011
Tagged Events	236	492
Dilution factor	0.28	0.28
Error on $\sin(2\beta)$	0.24	0.16

Table 3: Precision obtained on $\sin(2\beta)$ for 1 fb^{-1} in the upgraded DØ detector, comparing the two scenarios listed.

It is clear that the CP violation measurement benefits substantially from lepton tagging and triggering ability over $|\eta| \leq 2.5$. While the advantage from covering this whole range for hadronic final state reconstruction is somewhat more modest due to the decreased resolution at high $|\eta|$, it still yields a substantial improvement in the precision with which $\sin(2\beta)$ can be measured.

3.5.4 Other B -Physics Topics

Some of the other topics on which we expect to focus in our Run II B -Physics program are:

- Precision extraction of α_S^2 and α_S^3 processes. Preliminary results [65] from the azimuthal correlation between the two b -tagged jets are already available using the Run I data. The correlation is sensitive to the high order processes in the perturbative QCD calculation. This type analysis will benefit significantly from the improved b -tagging efficiency and increased statistics in Run II.
- Study of B_c spectroscopy – the B_c system is a unique laboratory for heavy quark effective theories with either b or c decays or $b\bar{c}$ annihilations.
- Study of b -baryons.
- Searches for rare B decays such as $B_d \rightarrow \pi/K\mu^+\mu^-$ and $B_d \rightarrow \mu^+\mu^-$. Preliminary studies with Run Ib data have already placed a limit on the decay $b \rightarrow s\mu^+\mu^-$ at 3.6×10^{-5} with 90% CL [66]. The improved muon momentum resolution and increased statistics will enable us to set more stringent limits on this type of processes.

3.6 Searches for New Phenomena

While the Standard Model is very successful in describing all the measurements of particle interactions currently available, it cannot be the whole story. It contains too many arbitrary parameters and the Higgs mechanism of electroweak symmetry breaking requires unnatural fine-tuning. Appealing theoretical frameworks which address these shortcomings have been suggested; examples include supersymmetry and new flavor symmetries. The spectrum of new states occurring in these models should be visible in the Tevatron Collider energy range. The Run II should cover much of the parameter space of the Minimum Supersymmetric Model (MSSM) for charginos (χ^\pm), neutralinos (χ^0), squarks (\tilde{q}) and gluinos (\tilde{g}). It is also necessary to search for completely unexpected new phenomena.

Searches for phenomena beyond the Standard Model have been an important part of DØ's physics menu to date. Their importance will continue to increase as greater accumulated luminosity stretches the reach into unexplored territory. The upgraded detector will maintain the unique DØ capabilities that have aided such searches in the past — the hermeticity of the calorimeter system, the excellent \cancel{E}_T resolution, and the large η coverage for lepton identification — and allow us to exploit the expanded capabilities of the detector to extend further into that territory.

3.6.1 An Overview of New Particle Searches

Some of the searches we have already undertaken are summarized in Table 4. The top quark is included in the table as a cross section comparison. The production cross sections are rough estimates of the range accessible at the Tevatron's center-of-mass energy for Run Ia's luminosity. The table shows current DØ mass limits from Run Ia, for completed searches, and the estimated discovery reach for 1 fb^{-1} , for some of the searches. (The discovery reach is the mass which could be observed with a 10-event signal.)

The table does not tell the complete story, however — while some exotic objects appear to be ruled out to quite large masses, this sometimes masks assumptions about branching ratios and/or coupling constants. For example, the gaugino limit assumes the most favorable branching ratios. There is still territory to be covered which requires triggering and analysis cuts to remain at fairly low E_T for the primary objects — jets, leptons, and \cancel{E}_T — and this should be an important consideration for the upgraded detector. Four examples of searches which will be advanced with the upgraded DØ detector are the Z' search, the gaugino search, the \tilde{t} search, and the $\tilde{q} - \tilde{g}$ search, described below.

3.6.2 The Z' Search

The current mass limit on a heavy Z' from DØ's search is $670 \text{ GeV}/c^2$, assuming the coupling of the Z' to leptons is identical to the Standard Model Z . The main determinant of the acceptance for this search is the η acceptance for lepton triggering and identification. The current DØ triggers for electrons reach out to $\eta < 2.5$. For the upgraded detector, these

Possible signals	Production cross sections (over accessible mass range)	Current Mass limit (model dependent)	Discovery reach 1 fb^{-1}
$t\bar{t}$	$5.25 \pm 1.79 \text{ pb}$	$169 \pm 11 \text{ GeV}/c^2$ (measured)	—
Right-handed W	$0.5\text{--}1000 \text{ pb}$	$650 \text{ GeV}/c^2$	
W'	$0.5\text{--}0.0001 \times \sigma_W$	$720 \text{ GeV}/c^2$	$\sim 1 \text{ TeV}/c^2$
Z'	$0.1\text{--}0.001 \times \sigma_Z$	$670 \text{ GeV}/c^2$	$\sim 1 \text{ TeV}/c^2$
scalar 1st generation leptoquarks	$1.0\text{--}100 \text{ pb}$	$130 \text{ GeV}/c^2$	$\sim 240 \text{ GeV}/c^2$
scalar 2nd generation leptoquarks	$1.0\text{--}100 \text{ pb}$	$110 \text{ GeV}/c^2$	$\sim 240 \text{ GeV}/c^2$
\bar{q} and \bar{g} pairs ($m_{\bar{q}} = m_{\bar{g}}$)	$5\text{--}1000 \text{ pb}$	$230 \text{ GeV}/c^2$	$\sim 200\text{--}320 \text{ GeV}/c^2$
gaugino pairs	$0.5\text{--}10 \text{ pb}$	$90 \text{ GeV}/c^2$	$\sim 90 \text{ GeV}/c^2$
stop	$0.1\text{--}100 \text{ pb}$	$93 \text{ GeV}/c^2$	
b'	$10\text{--}1000 \text{ pb}$	$m_Z + m_b$	
q^*	$0.1\text{--}100 \text{ pb}$	$720 \text{ GeV}/c^2$	

Table 4: Summary of DØ's current limits and mass reach for the discovery of new particles (10 events required for discovery). The limit on gaugino assumes the most favorable branching ratio.

searches will benefit from an approximately doubled acceptance through the use of muon as well as electron final states over $|\eta| < 2.0$ and $|\eta| < 2.5$ respectively.

3.6.3 The Gaugino Search

Our current searches for supersymmetric gaugino pairs seek to probe the mass region from the LEP limit of approximately $47 \text{ GeV}/c^2$ upward. While the production processes proceed through the electroweak interaction, the low mass still gives large enough cross sections to be explored with current data. The cleanest signature for $\chi_1^\pm - \chi_2^0$ pair production is the 3 lepton + \cancel{E}_T topology. (The \cancel{E}_T comes from an escaping lightest supersymmetric particle, or LSP.) The highest E_T lepton in such events has a mean E_T of only 24 GeV for a χ_1^\pm of mass $50 \text{ GeV}/c^2$, and the third lepton has a mean E_T of only 9 GeV. The upgraded detector is well-matched to this physics as it will operate with efficient (and unprescaled) electron and muon triggers for lepton transverse momenta down to $p_T \sim 10 \text{ GeV}/c$, and multilepton triggers may include muons as low as $p_T \sim 1.5 \text{ GeV}/c$. The gaugino search also requires full pseudorapidity coverage for lepton identification and measurement, as illustrated in Table 5 below which shows acceptance figures for a χ_1^\pm with a mass of $50 \text{ GeV}/c^2$.

While the leading lepton is predominantly central, the acceptance for the three-lepton state is a factor of ~ 3 larger for DØ's full pseudorapidity coverage ($|\eta| \lesssim 3$) than if lepton identification were restricted to $|\eta| \lesssim 1$.

η range	eee (Leading e)	$e\mu\mu$ ($p_T^e > 5$ GeV)
0.0 – 1.0	58.3%	57.1%
1.4 – 2.5	21.0%	22.6%
2.5 – 3.4	2.2%	3.0%
	Any electron ($p_T^e > 5$ GeV)	Any electron ($p_T^e > 5$ GeV)
1.1 – 1.4	27.2%	13.2%
1.4 – 4.0	47.1%	26.3%

Table 5: $D\bar{O}$ acceptance for 50 GeV/c² χ_1^\pm .

3.6.4 The \tilde{t} Search

Within current supersymmetry theories, the large mass of the top quark carries the extremely interesting implication that its supersymmetric partner, the \tilde{t} , will be split into two mass eigenstates, one of which will be significantly less massive than the top quark itself. We have already carried out a search for this low mass \tilde{t} in a mass range which extends above the region accessible to LEP II. This is another search for which a relatively low mass region will remain interesting through Run II. The offline analysis for this search imposed a cut on \cancel{E}_T of 40 GeV, and a lower cut would have been desirable. We aim to maintain a trigger on pure \cancel{E}_T , or \cancel{E}_T+1 or 2 jets, with a threshold of $\lesssim 50$ GeV and no prescale. While \cancel{E}_T trigger rates require some further study in the high luminosity regime, there appear to be no major problems. The reduced bunch spacing will mean that the number of interactions per crossing will be similar to that in Run Ib, and the faster calorimeter electronics will keep the pileup from out-of-time events in the calorimeter manageable. The upgraded inter-cryostat detector is also important for maintaining \cancel{E}_T precision. The search for the leptonic decay modes of the \tilde{t} , in the mass region heavier than the W but lighter than the top quark, will be very like the search for the top from 90 GeV/c² to 200 GeV/c².

3.6.5 The $\tilde{q} - \tilde{g}$ Search

The search for $\tilde{q} - \tilde{g}$ pair production, like the \tilde{t} search, uses both leptonic and hadronic decay modes and relies heavily on the measurement of \cancel{E}_T . Our limit of 230 GeV/c² for $m_{\tilde{q}} = m_{\tilde{g}}$ is from the decay signature of multiple jets plus \cancel{E}_T , and the leptonic analysis has been shown in conferences. In conjunction with the searches for \tilde{t} and gauginos, a combined analysis of these three supersymmetry signatures promises to make a significant contribution by either discovering supersymmetry or ruling out that portion of its (nearly infinite) parameter space most attractive to theorists.

It is important to stress that for the regime where the supersymmetry partners are in the range of 50–250 GeV/c², the Tevatron is the best place to make a supersymmetry discovery. In fact, this regime of the supersymmetry parameter space has been suggested [70] to explain the

CDF $ee\gamma\gamma$ event with \cancel{E}_T . The LHC detectors will have difficulty triggering at the low lepton E_T 's and \cancel{E}_T required to cover this range, in the presence of a large number of overlapping minimum bias events.

3.6.6 Other Searches

Many other searches for phenomena beyond the Standard Model have been and are being performed with the Run I data sets. Among these other searches are those for leptoquarks, b' quarks, excited quarks, W' bosons, right-handed W 's, heavy neutral leptons, charged Higgs, neutral Higgs, di-jet states and massive stable particles. In addition, non-Standard Model behavior is being sought in distributions from known particles as well. Di-boson analyses have produced limits on the anomalous gauge boson couplings, as will studies of QCD jet distributions. Composite effects are being sought in the Drell-Yan processes and in jet E_T distributions. *All* of these searches will continue to be interesting in the upgrade era. Except for the QCD jet distribution studies, the acceptance, and therefore reach, of these searches depends on the ability to trigger on and identify leptons and \cancel{E}_T . Since limits on several interesting new particles will remain below 150 GeV/ c^2 into Run II, we have aimed to preserve our capacity to trigger as low as possible in E_T and \cancel{E}_T , and to make the η coverage for triggering and tracking as broad as possible.

3.7 Beyond Run II

Run II promises a rich and varied physics program at DØ. However, there remains much interesting high- p_T physics which will require integrated luminosities an order of magnitude larger, $\sim 30 \text{ fb}^{-1}$. As an example, it has recently been suggested that it may be possible to observe light and intermediate mass Higgs bosons at the Tevatron collider, given sufficient integrated luminosity. Preliminary studies [68] indicate that the mass range $80 \lesssim m_H \lesssim 130 \text{ GeV}/c^2$ may be accessible for integrated luminosities $\mathcal{L} \gtrsim 30 \text{ fb}^{-1}$. This mass range is of great interest, since minimal supersymmetric versions of the standard model almost always predict a light Higgs boson lying in this region and the mass window is beyond the reach of LEP200 and is awkward for LHC. The possibility therefore exists of either discovering, or refuting, this whole class of models.

The channels of interest are $(W/Z)H$ with $W/Z \rightarrow \text{leptons}$ and $H \rightarrow b\bar{b}$, and $W/Z \rightarrow \text{jets}$ and $H \rightarrow \tau^+\tau^-$. The reconstruction techniques needed for a Higgs discovery — jet-jet spectroscopy using b -tagging information — are similar to, and will benefit from, the high-statistics study of top quark production. In order to accumulate sufficient statistics, operation at luminosities higher than that currently envisaged for Run II would be necessary. We have made a preliminary study of triggering and data acquisition at $\mathcal{L} = 2 \times 10^{33} \text{ cm}^{-2}\text{s}^{-1}$ [69] and find no insuperable obstacles to triggering on and recording these Higgs final states. Of course, such physics is properly beyond the scope of the present Upgrade; it is mentioned in order to emphasize that high- p_T physics at the Tevatron will remain of interest beyond Run II, and it is our belief that further luminosity increases are in fact desirable in order to fully exploit the physics opportunities. The upgraded detector described in this report provides a solid foundation for any additional enhancements that may be needed to meet the challenge of increased luminosity.

4 Conclusions

In this report we have described the upgrade to the DØ detector for Tevatron Run II, its cost and milestones, and outlined some of the physics which we intend to pursue. During this period, the Tevatron will be the highest energy accelerator available and will provide unsurpassed luminosity. We believe that the upgrade project satisfies the requirements of maintaining the excellent performance of the DØ detector while significantly improving its capabilities in the areas of b -tagging, and muon and electron identification and measurement. The result will be a versatile, general purpose detector, well-matched to the accelerator environment and to the physics requirements of Run II, with particular strengths complementary to those of CDF. We expect the upgraded DØ detector to play a leading role in carrying high energy physics into the twenty-first century.

References

- [1] “The DØ Upgrade”, unpublished (1990);
“P823 (DØ Upgrade): Responses to the Physics Advisory Committee” DØ note 1148 (1991);
“E823 (DØ Upgrade): R& D and Optimization Progress Report, DØ 1322 (1992);
“E823 (DØ Upgrade): Step-1 and Beyond”, DØ 1421 (1992);
“E823 (DØ Upgrade): DØ_β”, DØ 1733 (1993);
“E823 (DØ Upgrade): Magnetic Tracking”, DØ (1993).
- [2] “DØ Upgrade Technical Design Summary”, DØ note 2962.
- [3] “Conceptual Design of a 2 Tesla Superconducting Solenoid for the Fermilab DØ Detector Upgrade”, DØ note 2167 and Fermilab TM-1886 (May, 1994).
- [4] “DØ Silicon Tracker Technical Design Report”, DØ note 2169.
- [5] D.D. Pitzl et al., Nucl. Phys. B (Proc. Suppl.) **23A** (1991) 340;
H.J. Ziock et al., IEEE Trans. Nucl. Sci. **NS-38** (1991) 269.
- [6] C. Boswell, “Tests of Silicon Microstrip Wedge Detectors for the DØ Experiment”, in Proceedings of the 3rd International Workshop on Vertex Detectors, Bloomington, Indiana, May 8-13, 1994.
- [7] D. Adams *et al.*, Fermilab-Conf-94/318-E, presented at DPF’94;
M. Atac *et al.*, Nucl. Instrum. and Meth. **A314**, 56 (1992);
M.D. Petroff and M.G. Stapelblock, IEEE Trans. Nucl. Sci. **NS-36**, 158 (1989);
M.D. Petroff and M. Atac, *ibid*, p. 163.
- [8] D. Adams *et al.*, Fermilab-Conf-95/012E, January (1995).
D. Adams *et al.*, Nucl. Phys. B **44** 332 (1995).
D. Adams *et al.*, IEEE Trans. Nucl. Sci., Vol. 43, No. 3, 1146 (1996).
- [9] T. Zimmerman *et al.*, “The SVX II Readout Chip”, IEEE Transactions on Nuclear Science, Vol. 42, No. 4, August 1995.
- [10] M. Adams *et al.*, “Design Report of the Central Preshower Detector for the DØ Upgrade”, DØ note 3014.
- [11] M. Adams *et al.*, “A Detailed Study of Plastic Scintillating Strips with Axial Wavelength Shifting Fiber and VLPC Readout”, NIM **A366**, 263, (1995).
M. Adams *et al.*, “A New Detector Technique Using Triangular Scintillating Strips to Measure the Position of Minimum Ionizing Particles”, NIM **A378**, 131, (1996).
- [12] “The DØ Upgrade: Forward Preshower, Muon System and Level 2 Trigger”, DØ note 2894.
- [13] S.A. Kleinfelder et al., Nucl. Phys. B (Proc. Suppl.), **23A**, 382 (1991).
- [14] “Technical Design Report for the Upgrade of the ICD for DØ Run II”, DØ note 2686.

- [15] H.T.Diehl, "Aggressive Shielding Strategies for the Muon Upgrade", DØ Note 2713.
- [16] J.M. Butler *et al.*, "Reduction of Tevatron and Main ring induced backgrounds in the DØ detector", DØNote 2559, FNAL TN-629, Fermilab, 1995.
- [17] V. Sirotenko, "Progress on DØ Detector Shielding Optimization with GCALOR", DØ Note 2835.
- [18] R. Brock, "DØ Full Scintillator Coverage", Report to a Review Panel, May 1992.
- [19] H. T. Diehl *et al.*, "Proposal for Central Muon A-Layer Scintillator Trigger Counters", DØ Note 2213.
- [20] G. Alexeev *et al.*, "Studies of stability and systematics of operation of the DELPHI plastic tubes", NIM, A292, 551, 1990.
- [21] B. Baldin *et al.*, "Upgrade of the DØ forward muon system with pixel scintillation counters", IEEE Transaction on Nuclear Science, No. 4, August 1995, pp. 736-742.
- [22] Yu. Nikolaev *et al.*, "The efficiency of plastic scintillators to neutrons and gammas", SDC-93-512, SSCL 1993.
- [23] D. Green, "Muon System Pixel Trigger Rates in EF", DØ Note 2551.
- [24] B. Baldin, *et al.*, "DØ Upgrade Muon Electronics Design", IEEE Transactions on Nuclear Science, Vol 42, (1995) 736.
- [25] Y.Arai, F.Sudo and T.Emura, "Developments of Time Memory Cell VLSI's." KEK Preprint 93-49, June 1993 H.
- [26] J.M.Butler *et al.*, Nucl. Inst. Meth. **A290** (1990) 122.
- [27] "The Level 3 Trigger Upgrade", DØ note 2943.
- [28] S. Fuess, "DØ Run 2 Online Computing", DØ note 2935.
- [29] "DØ Analysis Computing Recommendations for Run II", DØnote 2537.
- [30] DØ Collaboration, "The Standard Model and Beyond", Fermilab-FN-640 (1995).
- [31] S. Abachi *et al.*, (DØ Collaboration), Phys. Rev. Lett. **74** (1995) 2632.
- [32] ISAJET 7.13 Program:
F. Paige and S. Protopopescu, BNL Report No. BNL38034, 1986 (Unpublished).
- [33] HERWIG Program:
G. Marchesini and B. Webber, Nucl. Phys. **B310** (1988) 461;
I.G. Knowles, Nucl. Phys. **B310** (1988) 571;
G. Marchesini *et al.*, Comp. Phys. Comm. **67** (1992) 465.
- [34] VECBOS Program:
F.A. Berends *et al.*, Nucl. Phys. **357**, 32 (1991).

- [35] G. Kane, C.P. Yuan and G. Ladinsky, Phys. Rev. **D45**, 124 (1992).
- [36] A.S. Belyaev, E.E. Boos and A.P. Heinson, in preparation.
- [37] D.O. Carlson and C.-P. Yuan, Phys. Lett. **B306**, 386 (1993).
- [38] T. Stelzer and S. Willenbrock, Phys. Lett. **B357**, 125 (1995).
- [39] E. Eichten and K. Lane, Phys. Lett. **327** (1994) 129.
- [40] C. Hill and S. Parke, Phys. Rev. **D49** (1994) 4454.
- [41] V. Barger and R.J.N. Phillips, MAD/PH/830 (1994).
- [41] V. Barger and R.J.N. Phillips, MAD/PH/830 (1994).
- [42] K. Lane, BUHEP-95-2 (1995) and private communications.
- [43] M. Demarteau *et al.*, "Measurement of the W Mass", DØ note 2929.
S. Abachi *et al.*, FNAL-PUB-96/177E, submitted to Phys. Rev. Lett.
- [44] I. Adam *et al.*, " W Boson Mass Measurement using Run Ib Data", DØ note 2982.
S. Abachi *et al.*, submitted to ICHEP, Warsaw, July 1996.
- [45] M. Rijssenbeek, talk at the 1996 International Conference on High Energy Physics, Warsaw (1996).
- [46] J. Alitti *et al.* (UA2 Collaboration), Phys. Lett. **B276**, 354 (1992).
- [47] F. Abe *et al.* (CDF Collaboration), Phys. Rev. Lett. **65**, 2243 (1990), Phys. Rev. D **43**, 2070 (1991);
F. Abe *et al.* (CDF Collaboration), Phys. Rev. Lett. **75**, 11 (1995), Phys. Rev. **D52**, 4784 (1995).
- [48] Review of Particle Properties by the Particle Data Group, Phys. Rev. D50, No. 3, p.1173, August 1994.
- [49] J. Rosner, M.P. Worah, and T. Takeuchi, Phys. Rev. D **49**, 1363 (1994).
- [50] F. Abe *et al.*, (CDF collaboration), Phys. Rev. Lett. **74** (1995) 341.
- [51] CTEQ Collaboration (J. Botts *et al.*), Phys. Lett. **B304** (1993) 159.
- [52] A.D. Martin, R.G. Roberts and W.J. Stirling, Phys. Lett. **B306** (1993) 145; **B309** (1993) 492(E).
- [53] CDF collaboration, (F. Abe *et al.*), Phys. Rev. Lett. **74**, 850 (1995).
- [54] P. Renton, the Proceedings of the International Symposium on Lepton Photon Interactions, Beijing, August 1995.
- [55] H. Weerts for the DØ collaboration, proceedings of the Tsukuba $p\bar{p}$ conference, Tsukuba, Japan (1993).

- [56] S. Ellis, Z. Kunszt, and D. Soper, Phys. Rev. Lett. **62**, 2188 (1989); Phys. Rev. Lett. **64**, 2121 (1990).
- [57] W. Giele et al., “The Two-Jet Differential Cross Section at $O(\alpha_s^3)$ in Hadron Collisions”, Fermilab Pub-94/070-T, 1994.
- [58] G. Sterman, private communication.
- [59] W. Giele et al., Phys. Rev D46, 1980 (1992); Nucl.Phys. B403, 633 (1993).
- [60] H. Baer, J. Ohnemus, and J. Owens, Phys. Lett. **B234**, 127 (1990).
- [61] A. Brandenburg and O. Nachtmann, “Spin Effects and Factorization in Drell-Yan Process”, Preprint HD-THEP-93-13, 1993.
- [62] S. Abachi et al., (DØ collaboration), Phys. Rev. Lett. **72** (1994) 2332.
- [63] D. Hedin and K. Johns, DØ note 2113 (1994).
- [64] MCFAST simulation package, Fermilab Computing Division.
- [65] S. Abachi *et al.*, “The $b\bar{b}$ Production Cross Section and Correlations in $p\bar{p}$ Collisions at $\sqrt{s} = 1.8$ TeV”, submitted to the 28th International Conference on High Energy Physics, Warsaw, Poland, July 1996.
- [66] S. Abachi *et al.*, “Search for $b \rightarrow X\mu^+\mu^-$ and $B^0 \rightarrow \mu^+\mu^-$ Decays in $p\bar{p}$ Collisions at $\sqrt{s} = 1.8$ TeV”, submitted to the 28th International Conference on High Energy Physics, Warsaw, Poland, July 1996.
- [67] S. Abachi et al., Fermilab PUB-95/057-E, submitted to Physical Review Letters.
- [68] A. Stange, W. Marciano and S. Willenbrock, Phys. Rev. **D50** (1994) 4491;
S. Mrenna and G. Kane, UM-TH-94-24;
A. Belyaev, E. Boos and L. Dudko, Mod. Phys. Lett. **A10** (1995) 25.
- [69] J. Womersley, DØ Note 2371 (1994).
- [70] S. Ambrosanio *et al.*, “Supersymmetric analysis and predictions based on the CDF $ee\gamma\gamma + \cancel{E}_T$ event”, hep-ph/9602239 (1996).